



저작자표시-비영리-변경금지 2.0 대한민국

이용자는 아래의 조건을 따르는 경우에 한하여 자유롭게

- 이 저작물을 복제, 배포, 전송, 전시, 공연 및 방송할 수 있습니다.

다음과 같은 조건을 따라야 합니다:



저작자표시. 귀하는 원저작자를 표시하여야 합니다.



비영리. 귀하는 이 저작물을 영리 목적으로 이용할 수 없습니다.



변경금지. 귀하는 이 저작물을 개작, 변형 또는 가공할 수 없습니다.

- 귀하는, 이 저작물의 재이용이나 배포의 경우, 이 저작물에 적용된 이용허락조건을 명확하게 나타내어야 합니다.
- 저작권자로부터 별도의 허가를 받으면 이러한 조건들은 적용되지 않습니다.

저작권법에 따른 이용자의 권리는 위의 내용에 의하여 영향을 받지 않습니다.

이것은 [이용허락규약\(Legal Code\)](#)을 이해하기 쉽게 요약한 것입니다.

[Disclaimer](#)

공학박사학위논문

Phase and Structure Control of Metal Compound
and Carbon Hybrid Nanofibers using
Thermodynamic Redox Reaction

열역학적 산화 및 환원 반응에 의한 금속 화합물/
탄소 나노섬유의 상 및 구조 제어 연구

2017년 2월

서울대학교 대학원

재료공학부

남 대 현

ABSTRACT

Phase and Structure Control of Metal Compound and Carbon Hybrid Nanofibers using Thermodynamic Redox Reaction

Dae-Hyun Nam

Department of Materials Science and Engineering

The Graduate School

Seoul National University

Precise phase control in nanoscale synthesis and spontaneous assembly in macroscopic dimension are important but difficult for practical implementation of nanomaterials. In frequently-encountered situations where multiple components are involved in synthesis, the most of difficulties about mass production and reproducibility are related to the lack of thermodynamic and kinetic predictability. Inspired by chemical metallurgy theories, an insight to solve the limitations in nanomaterial synthesis has been suggested in this thesis.

Metal compound/carbon nanofibers are receiving great attention for the energy and environmental applications. Metal compound acts an active material which shows high electrochemical activity. Electrically conductive carbon (C) nanofiber is a supporter which maintains high-aspect ratio one-dimensional (1D) structures. In this thesis, a new functionality of C nanofiber has been pioneered as a determinant to control the spontaneous of atomic species and final structures of metal compound. It is based on oxidation based C decomposition, which produces gaseous decomposition products such as carbon monoxide (CO) and carbon dioxide (CO₂). Based of the reaction between O₂

and C, the degree of C decomposition can be precisely controlled by the oxygen partial pressure (pO_2). In multi-atomic component system, the reaction between the elements can generate many intriguing compounds. For inducing the reaction between selected elements, Ellingham diagram and phase diagram can contribute to predict processing parameters and material composition. Based on this theoretical background, an innovative fabrication methodology for controlling the phase and structures of active materials and C nanofibers has been developed *via* predictive synthesis. Escaping from the control in solution process, it is based on gas-solid reactions which can realize the mass production of complex multi-atomic nanomaterials with high uniformity.

The first focus is the demonstration of selective C oxidation induced reductive metal structure control. Based on the oxidation Gibbs free energy (ΔG) of C, metals are categorized into reductive and oxidative metals. In the case of reductive metals such as Co, Ni, Cu, Pt, etc., selective redox reaction induces C oxidation and metal reduction. According to the pO_2 in this condition, full-filled C nanofibers with embedded metal nanoparticles, metal/C core/shell nanofibers, hollow and porous C nanofibers are formed. The mechanism of this structure evolution according to the pO_2 has been studied by the catalyzed C oxidation at the surface of metallic species.

The second focus is an in-depth study about the effect of C porosity on the structures of oxidative metallic species. The size and distribution of Sn, which shows high capacity active material in Li-ion battery anode, was optimized by managing the outward Sn diffusion during calcination. For minimizing the volumetric expansion based material degradation, the strategy for inducing Sn nanoparticles fully-embedded has been established. By utilizing the pressure equilibrium to derive reverse direction of Boudouard reaction, C porosity could be controlled by ambient conditions.

Finally, selective redox reaction scheme has been verified in multi-atomic component system to control molybdenum disulfide (MoS_2) inside C nanofibers. The redox reactions of Mo-S-C-O were categorized according to the $p\text{O}_2$. Especially, at the $p\text{O}_2$ between ΔG of C and Mo oxidation, C is decomposed by combustion with MoS_2 formation. In ternary phase diagrams, Mo-S-C-O mole fraction was determined to form MoS_2 and gaseous C oxide such as CO and CO_2 . The calcination in this region was induced to control MoS_2 structures by modulating the vertical stacking and lateral growth of MoS_2 stacking unit. Through this methodology various MoS_2 structures such as length, stacking number, distribution, and alignment were induced.

In this thesis, it has been revealed that the structure and phase of metal compound/C nanofibers can be precisely controlled by the predicted parameters from the same metal precursor and polymer matrix nanofibers. This customized fabrication has a potential to tuning the properties of metal compound/C nanofibers according to the various applications such as electronic, chemical, energy, and environment fields.

Keywords: Electrospinning, metal compound/carbon nanofibers, calcination, selective oxidation, Ellingham diagram, phase diagram, predictive synthesis

Student Number: 2011-20636

Table of Contents

Abstract.....	i
Table of Contents.....	iv
List of Tables.....	ix
List of Figures.....	x

Chapter 1. Introduction

1.1. Metal compound/carbon hybrid nanofibers	1
1.2. Phase and structure control issues of metal/C nanofibers	7
1.2.1. Solution process based active material loading inside C nanofibers	7
1.2.2. Thermodynamics for phase control	12
1.2.3. Kinetics for atomic diffusion induced structure control	15
1.3. Objective of the thesis	17
1.4. Organization of the thesis	23

Chapter 2. Theoretical Background

2.1. Nanofibers	24
-----------------------	----

2.2. Electrospinning	29
2.2.1. Effect of solution parameters	31
2.2.2. Effect of processing and ambient parameters	32
2.2.3. Coaxial-Electrospinning	33
2.3. Calcination	35
2.3.1. Selective oxidation	36
2.3.2. Boudouard reaction	38
2.4 Thermodynamic tools for predictive synthesis	42
2.4.1. Ellingham diagram	43
2.4.2. Ternary phase diagram	45
2.4.3. Reciprocal phase diagram	51
2.4.4. Relationship between phase diagram and Ellingham diagram	53

Chapter 3. Experimental Procedures

3.1. Sample preparation by electrospinning	55
3.1.1. Reductive metal/C nanofibers	55
3.1.2. Oxidative metal/C nanofibers	56
3.1.3. Metal compound/C nanofibers	56
3.2. Calcination	59
3.2.1. Oxygen partial pressure controlled calcination	59
3.2.2. Oxygen empty ambient condition induced calcination	59
3.3. Microstructure analysis	62
3.4. Chemical analysis	62

3.5. Electrical and electrochemical property	63
3.5.1. Electrical conductivity	63
3.5.2. All solid state Li-ion battery anode performance	63
3.6. Computation	65
3.6.1. Factsage TM calculation	65
3.6.2. Density Functional Theory (DFT) calculation	65

Chapter 4. Selective Carbon Oxidation based Reductive Metal/Carbon Nanofiber Structure Control

4.1. Introduction	66
4.2. Ambient effect on the thermal decomposition during calcination	67
4.3. Thermodynamics in calcination of Cu/C nanofibers	69
4.4. Microstructural changes of Cu/C nanofibers by selective oxidation	73
4.5. Mechanism of Cu/C nanofiber formation	80
4.6. Effect of Cu/C nanofiber structures on electrical properties	85
4.7. Summary	91

Chapter 5. Selective Carbon Oxidation induced Hollow Structure Formation in Metal/Carbon Nanofibers

5.1. Introduction	92
5.2. Thermodynamic consideration on the	94

calcination of reductive metal/carbon nanofibers	
5.3. Structure evolution of reductive metal/carbon nanofibers with the hollow structure formation	101
5.4. Catalytic carbon oxidation on metal surface	103
5.5. Mechanism of hollow C structure formation	111
5.6. Summary	114

Chapter 6. Phase Equilibrium based Carbon Porosity Engineering for Oxidative Metal Structure Control

6.1. Introduction	116
6.2. Gas-solid reaction based Sn/C structure control	118
6.3. Effect of ambient condition on porosity of Sn/C nanofibers	126
6.4. Material properties of Sn/C nanofibers	133
6.5. All solid state Li-ion battery performance	139
6.6. Summary	145

Chapter 7. Thermodynamic based Reaction Prediction of Multi-component Atomic System for Kinetic van-der Waals Solid Structure Control

7.1. Introduction	146
7.2. Thermodynamic calculation for redox control in Mo-S-C-O quaternary system	149

7.3. Validation of molybdenum sulfidation and carbon oxidation	159
7.4. MoS ₂ rational design according to the thermodynamic-driven processing parameters	165
7.5. Kinetics of MoS ₂ layer formation	172
7.6. Summary	178
 Chapter 8. Conclusion		
8.1. Summary of results	180
8.2. Future works and suggested research	183
References	185
Abstract (In Korean)	192

LIST OF TABLES

Table 6.1 Comparison of the BET surface area and the total pore volume of the Sn/C nanofibers formed using the various calcination conditions.

Table 6.2 Parameters of the Raman analysis of the Sn/C nanofibers according to the calcination methods.

LIST OF FIGURES

- Figure 1.1** Renewable energy circulation from the sun-light, CO₂, and water resources.
- Figure 1.2** Schematics for displaying the components of metal (composite)/C hybrid nanofibers for energy and environmental application.
- Figure 1.3** Effect of metal(composite) loading on C nanofiber properties. **(a)** Dependence of electric double-layer capacitance on discharge current density according to the calcination temperature, **(b)** Electrochemical adsorption capacity of Na ion, **(c)** TEM image of Sn/SnO_x containing C nanofibers, **(d)** Cycle performance in Li-ion battery with a current density of 30 mA/g, **(e)** TEM image of MnO_x-loaded C nanofiber, and **(f)** Cycle performance of Li-ion battery according to the loading amount of Mn(OAc)₂ precursor.
- Figure 1.4** **(a)** The research scope of this thesis about the active material/supporter hybrid nanomaterials. It is fabrication method design to control atomic arrangement and related electronic structure. **(b)** Categorization of active material/C hybrid nanofibers according to the composition of functional materials.

Figure 1.5 Electrospinning methodology for the fabrication of metal compound containing heterogeneous nanofibers. **(a)** Direct-dispersed electrospinning, **(b)** Gas-solid reaction, **(c)** In-situ photoreduction, **(d)** Sol-gel method.

Figure 1.6 Previous researches for metal compound/C nanofiber structure control in the aspects of active material and C nanofibers.

Figure 1.7 **(a)** Phase diagram of Na-O as a function of temperature and pO_2 . **(b)** Phase diagram of Na_2O_2 and NaO_2 at 300 K as a function of particle size and pO_2 . **(c)** Facet related morphology evolution of Mg-calcite and aragonite with a function of Mg^{2+} . **(d)** Kinetic phase diagram of the nucleation rate related with Mg:Ca ratio. **(e)** Bulk phase diagram of Li-O as a function of temperature and pressure. **(f)** Nano-scale phase diagram of Li_3O_4/Li_2O_2 .

Figure 1.8 Effect of thickness of outer Al_2O_3 shell on the degree of outer Cu diffusion after calcination. As the thickness of oxide decreases, the degree of Cu diffusion increases and the size of Cu agglomerates increases.

Figure 1.9 Overview of the thesis

Figure 1.10 Gas-solid reaction based control scheme

Figure 1.11 Potential applications of phase and structure controlled metal compound/C nanofibers.

Figure 2.1 Categorization of nanomaterials according to the structural dimension and aspect ratio. Nanorod, nanowire, and nanofiber are 1D nanostructured materials and they can be classified by the aspect ratio. Secondary nanostructures such as core/shell, hollow, and porous can be induced in nanofibers with the aspect ratio of 1000.

Figure 2.2 (a) Length and (b) thickness dependence of 1D nanostructured materials on percolation theory based electrical conduction.

Figure 2.3 (a) FE-SEM image of nanofiber fabricated by electrospinning. (b) Dimension of electrospun nanofibers.

Figure 2.4 Electrospinning system for fabrication of nanofibers. Equipment is composed of voltage source, syringe pump, and collector. The solution for electrospinning is composed of polymer matrix to build nanofiber structure, metal precursor for functional element, and solvent to dissolve the solutes.

Figure 2.5 Optical images for displaying the whipping motion of electrospinning jet.

- Figure 2.6** Effect of processing parameters such as applied voltage, feeding rate, and jetting distances on the morphologies of electrospun nanofibers.
- Figure 2.7** Schematic for indicating the coaxial electrospinning with the dual nozzle to simultaneously induce the flow of two solutions with the different composition. Based on this method, core/shell, hollow and porous nanofibers are fabricated.
- Figure 2.8** Structures of nanofibers fabricated by the co-axial electrospinning. **(a)** core/shell nanofibers, **(b)** hollow nanofibers, **(c)** porous nanofibers.
- Figure 2.9** **(a)** Calcination process of electrospun copper acetate+polyvinyl alcohol nanofibers. **(b)** Thermogravimetric analysis (TGA) of coal for comparison of combustion and pyrolysis.
- Figure 2.10** Categorization of redox reactions of metal and C according to the Gibbs free energy of oxidation in Ellingham diagram. Aspects of phase transformation of metal ion and C decomposition are classified as full oxidation, full reduction, and selective oxidation.
- Figure 2.11** Reaction off-gas P_{CO}/P_{CO_2} for graphite, coke, char with lime additions at the temperatures of **(a)** 1000 °C, **(b)** 1100 °C, **(c)** 1200 °C.

- Figure 2.12** Application of Boudouard reaction to control the porosity of C nanofibers according to the pressure equilibrium of the chamber. In high vacuum calcination, overall chamber pressure is constant. There is no preference in Boudouard reaction. In Ar gas calcination, overall chamber pressure increases and reverse Boudouard reaction proceeds.
- Figure 2.13** Ellingham diagram for considering the standard Gibbs free energy of various oxide compounds according to the temperature.
- Figure 2.14** Ternary phase diagram classification according to the distribution of tie-lines. **(a)** GaAs dominant, **(b)** MGa_x dominant, **(c)** MAS_y dominant phase diagram. **(d)** No phase dominant phase diagram
- Figure 2.15** Effect of Gibbs free energy of the reaction between compounds on the types of thermodynamic ternary phase diagram. According to the reaction activity between elements, metal oxide dominant, no phase dominant, SiO_2 dominant phase diagrams are determined with the assumption of no ternary phases (MSi_xO_y) and only one M_x phase.
- Figure 2.16** Comparison of Kohler and Toop equation theories for the demonstration of ternary phase diagrams.

Figure 2.17 Composition square of reciprocal phase diagrams in the geometrical basis of the CIS equation.

Figure 2.18 Comparison of the Gibbs free energy between Ellingham diagram and phase diagram. Line cd shows the standard Gibbs free energy term in pure element system. When the element M is in solid solution at a_M , the energy term changes to cf. When the compound MO_2 is in solid solution at a_{MO_2} , the energy term changes to ch.

Figure 3.1 Metal (composite)/C Nanofiber fabrication process by electrospinning and calcination

Figure 3.2 Effect of viscosity of electrospinning solution on the nanofiber morphology. **(a)** 10 wt.% PVA with the viscosity of 8.38 poise, **(b)** 13 wt.% PVA with the viscosity of 10.90 poise, **(c)** 15 wt.% PVA with the viscosity of 12.90 poise.

Figure 3.3 Oxygen gas confined calcination scheme for oxygen partial pressure control during calcination.

Figure 3.4 Schematic for displaying the difference of degree of pressure change according to the oxygen partial pressure control methodology. In the condition of **(a)** closed chamber system, chamber pressure increases due to the closed valve, accumulation of gaseous decomposition products inside chamber. In the condition of **(b)** open chamber system, chamber pressure maintains constant value due to the gas flowing out behavior by pump.

Figure 3.5 Optical images of **(a)** free-standing electrospun SnAc+PAN nanofiber mats with **(b)** magnified images and **(c)** after bending. **(d)** Free-standing Sn/C nanofiber mats after 700 °C 5h calcination and **(e)** after punching the mats into a 10 mm diameter disk. **(f)** Pressed 77.5Li₂S-22.5P₂S₅ solid electrolyte pellet in all-solid-state Li-ion battery testing cell die. **(g)** Pressed free-standing Sn/C nanofiber mats anode on the solid.

Figure 4.1 Thermogravimetric analysis (TGA) and TEM images of the electrospun CuAc and PVA nanofibers comparing the C decomposition degree of full oxidation and full reduction under **(a, b)** air for combustion and **(c, d)** Ar gas for pyrolysis.

Figure 4.2 (a) Redox reaction schemes according to the effect of pO_2 during calcination on the electrospun CuAc+PVA nanofibers. (b) Schematic indicating the Cu/C nanofiber formation mechanism for the fully filled, core/shell, hollow, and porous/hollow nanofibers by selective oxidation. According to the structures of the C nanofiber, the inward or outward Cu diffusion related to the CTE differences between Cu and C is determined.

Figure 4.3 (a) Phase transformation for Cu relative to the calcination pressure as determined by XRD. (b) Quantitative XPS analysis of C decomposition in the Cu/C nanofibers. These analyses indicate that the pressure range from 1.0×10^{-2} to 1.0×10^{-1} Torr provides selective oxidation.

Figure 4.4 Comparison of the Cu 2p XPS spectra to investigate the existence of Cu phase in the nanofiber after calcination. With the exception of 7.6×10^2 Torr, a pure Cu phase was observed across the calcination range from 1.0×10^{-5} Torr to 1.0×10^{-1} Torr.

Figure 4.5 FE-SEM and TEM images of the Cu/C nanofibers formed via selective oxidation at 700 °C with a 5 h calcination at **(a)** 1.0×10^{-2} Torr, **(b)** 2.5×10^{-2} Torr, **(c)** 5.0×10^{-2} Torr, and **(d)** 6.0×10^{-2} Torr. Increasing the pressure decreases the C shell thickness of the Cu/C nanofiber. According to the pressure, various Cu/C structures are formed, including fully filled C nanofibers, Cu/C core/shell nanofibers, hollow C nanofibers, and porous/hollow C nanofibers.

Figure 4.6 The Cu/C nanofiber structural transformation *via* FE-SEM and TEM images with HAADF and EDS for the 700 °C calcination at 2.5×10^{-2} Torr over **(a)** 1 h, **(b)** 3 h, **(c)** 5 h, and **(d)** 10 h with the **(e)** calcination profile. The calcination time effects revealed the growth of the inner diameter of the hollow C nanofiber, which induced inward/outward Cu diffusion based on the C decomposition amount.

Figure 4.7 Structural transformation map of the Cu/C nanofibers simultaneously considering the calcination pressures from 1.0×10^{-2} Torr to 6.0×10^{-2} Torr and times from 1 h to 10 h using FE-SEM. The nanofibers are categorized by colors according to their degree of hollow C structure and Cu dispersion. The hollow structure formation rate increased with increasing pressure.

Figure 4.8 Effect of processing parameters in the aspects of temperature, pressure, and time on the process of hollow C nanofiber formation. With increasing degree of C decomposition, inner diameter of hollow C increases. It can be simultaneously induced by pressure and time control during calcination. As the temperature increases, the pressure region for selective oxidation increases.

Figure 4.9 (a) FT-IR spectra for investigating the CuAc decomposition during the calcination of electrospun CuAc+PVA nanofibers based on the ramping region temperature. Schemes indicating for the (b) C concentration gradient as a driving force of outward C diffusion and (c) Cu/C nanofiber formation mechanism of the fully filled, core/shell, hollow, and porous/hollow nanofibers by selective oxidation.

Figure 4.10 Structures of PVA nanofibers after calcining at (a) 1.0×10^{-5} Torr for full reduction and (b) 1.0×10^{-2} Torr, (c) 5.0×10^{-2} Torr, and (d) 1.0×10^{-1} Torr for selective oxidation. Calcining at 1.0×10^{-1} Torr decomposed all of the material with only the substrate remaining. (e) Before the calcination, uniform PVA nanofibers were formed.

Figure 4.11 (a) I-V curve for the Cu/C nanofibers formed *via* selective oxidation according to pressure and the (b) sheet resistance (R_s) determined *via* the Van der Pauw method. (c) TEM EDS line profile for the dual Cu and C components of the Cu/C core/shell nanofibers. (d) High oxidation resistance of the Cu/C core/shell nanofibers formed at 2.5×10^{-2} Torr. R_s was measured under atmospheric conditions.

Figure 4.12 Effect of Cu structures (particle size and distribution) on the mechanical-electrical reliability, which has been analyzed by the bending fatigue test during 500,000 cycles. (a) Relative resistance change with increasing bending cycles and (b) FE-SEM images after 500,000 cycles of Cu embedded inside C nanofibers according to the compressive strain. (c) Relative resistance change with increasing bending cycles and (d) FE-SEM images after 500,000 cycles of Cu agglomerated outside C nanofibers according to the compressive strain.

Figure 4.13 (a) FE-SEM and (b) TEM images for displaying the cross-linked broken nanofibers by diffused Cu after 500,000 bending fatigue cycles of Cu embedded C nanofibers in 2% strain condition.

Figure 5.1 Thermodynamic consideration about gas-solid reactions in the calcination of metal precursor + polymer matrix nanofibers. **(a)** Schematics for indicating gas-solid reactions between gaseous O₂ and solid state metal + C atoms in nanofiber system. **(b)** Categorization of redox reactions of metal and carbon (C) such as full reduction, selective oxidation, and full oxidation according to the oxidation Gibbs free energy (ΔG). **(c)** Schematic for structure evolution of metal/C nanofibers with increasing oxygen partial pressure (pO_2) in selective oxidation region.

Figure 5.2 **(a)** Ellingham diagram for indicating oxidation tendency of C and various metals such as Fe, Co, Ni, Cu, and Pt. **(b)** FactsageTM calculated ternary phase diagrams of metal (Fe, Co, Ni, Cu)-C-O system for prediction of materials composition between metal precursor and polymer matrix, and relative ratio between chamber pressure and mass of specimen.

Figure 5.3 FE-SEM and TEM images for displaying the metal/C nanofiber structures of **(a)** Co, **(b)** Ni, **(c)** Cu, and **(d)** Pt with the pressure control in the series of high vacuum ($<10^{-5}$ Torr), 1.0, 2.5, 5.0, and 6.0×10^{-2} Torr during the calcination temperature and time of 700 °C and 5h. With increasing pressure, hollow and porous C structures form. Compared to metal/C nanofibers formed by high vacuum calcination, the selective oxidation based structures show higher C decomposition degree. **(e)** Difference of the pressures which induce hollow and porous structures according to the metal types.

Figure 5.4 Mechanism of oxidation based C combustion process in metal/C hybrid nanofibers. Density functional theory (DFT) calculation to compare the preference of C oxidation at the metal surface and vacuum in the case of **(a)** CO and **(b)** CO₂ formation.

Figure 5.5 DFT calculation for energy computation in O₂ dissociation and CO formation on Ni (111) and Cu (111) surface. **(a)** O₂ dissociation on Ni (111) which shows the initial state for bridge-top and final state for two fcc site. **(b)** CO formation on Ni (111) which shows the initial state for two hcp site and final state for hcp site in perpendicular direction. **(c)** O₂ dissociation on Cu (111) which shows the initial state for bridge-bridge and final state for two hcp site. **(d)** CO formation on Cu (111) which shows the initial state for two hcp site and final state for fcc site in perpendicular direction.

Figure 5.6 Schematic for general C oxidation process to form carbon monoxide (CO) and carbon dioxide (CO₂) on the surface of metal species.

Figure 5.7 (a) Overall C oxidation steps of C adsorption, O adsorption, O₂ dissociation and CO formation on metal surface, CO desorption. (b) Density functional theory (DFT) calculation based energy consideration of C adsorption, O adsorption, and CO desorption according to the metals of Pt, Cu, Ni, Co.

Figure 5.8 Procedure of hollow C structure formation in metal/C nanofibers by catalytic selective oxidation on metal surface. C matrix induced by calcination of polyvinyl alcohol (PVA) is amorphous structure. O₂ molecules diffuse toward metal located inside nanofibers because C oxidation is preferred at the metal surface. CO and CO₂ form at the matrix near the metal nanoparticles. Continuous C oxidation can induce hollow C structure by the accumulation of pores inside C matrix.

Figure 6.1 (a) Structural modulation schemes of the Sn/C nanofibers by controlling the porosity of the C nanofibers. FE-SEM and TEM images with HAADF, EDS of Sn/C nanofibers for Sn size and distribution comparison according to the calcination conditions. (b,c) SA calcination, (d,e) HV calcination, and (f,g) Ar calcination.

Figure 6.2 Transmission electron microscope (TEM) images, reproduced images for particle size and distribution analysis of the Sn/C nanofibers formed by (a,b) SA calcination, (c,d) HV calcination, and (e,f) Ar calcination. Sn particle distributions are represented by the histogram.

Figure 6.3 (a) Brunauer-Emmett-Teller (BET) specific surface areas of the Sn/C nanofibers according to the calcination conditions. (b) Comparison of the pore size distribution between the Sn/C nanofibers using the Barrett-Joyner-Halenda (BJH) plot.

Figure 6.4 Fitting plot for investigating the Brunauer-Emmett-Teller (BET) surface area according to the relative pressure (P/P_0). (a) SA calcination, (b) HV calcination, and (c) Ar calcination.

Figure 6.5 TGA and DSC of electrospun SnAc + PAN nanofibers to investigate the thermal decomposition process under (a) air and (b) N_2 gas flow in inert condition.

Figure 6.6 (a) FT-IR of Sn/C nanofibers from electrospinning to stabilization and calcination for investigating the thermal decomposition behavior of the SnAc and PAN. (b) Magnified range of transmittance in the FT-IR.

Figure 6.7 Calcination pressure and time profile schematics according to the tailoring methods of pressure equilibrium, such as (a) HV calcination and (b) Ar calcination. (c) XPS analysis for quantitative investigation of the weight percent ratio between C1s and Sn3d5 in the Sn/C nanofibers.

Figure 6.8 (a) XRD analysis for investigating the phase of Sn in the SANFs, HVNFs, and ArNFs. (b) Raman analysis for investigating the C crystallinity in the Sn/C nanofibers according to the calcination conditions. The electrical properties of the Sn/C nanofibers free-standing mats with (c) current-voltage (I-V) sweep and (d) sheet resistance measurement using the Van der Pauw method.

Figure 6.9 XPS analysis for investigating the oxidation states of Sn in **(a)** SANFs after SA calcination, **(b)** HVNFs after HV calcination, **(c)** ArNFs after Ar calcination. The relative differences between them are quantitatively represented by the **(d)** Sn $3d_{5/2}$ relative peak area.

Figure 6.10 The electrochemical properties of the Sn/C nanofibers as the anodes of all-solid-state Li-ion batteries. **(a)** The cycle performances and coulombic efficiencies of the Sn/C nanofibers according to the Sn structures. The charge/discharge profiles of **(b)** ArNFs, **(c)** HVNFs, and **(d)** SANFs during cycling. **(e)** Comparison of the rate capability between HVNFs and ArNFs.

Figure 6.11 Differential charge and discharge profiles of **(a)** ArNFs and **(b)** HVNFs as the anodes in all-solid-state Li-ion cells from the 1st to the 50th cycle.

Figure 7.1 Thermodynamic Strategy to induce processing parameter and material composition to control MoS_2 formation. **(a)** Atomic system of Mo, S, C in nanofibers and O in ambient. **(b)** Ellingham diagram which provides Gibbs free energy of reactions between Mo, C and S, O.

Figure 7.2 Ternary phase diagrams of nanofiber components to predict phase formation in the components of Mo, S, O, and C. **(a)** Mo-S-C, **(b)** Mo-S-O, **(c)** Mo-C-O, and **(d)** MoS₂-C-O at the calcination condition of 800 °C, 0.1~0.4 Torr.

Figure 7.3 FactsageTM-calculated thermodynamic behavior of gas formation and phase transformation. **(a)** Evolution of thermodynamically stable phases calculated according to the O₂ moles in a closed chamber system and related **(b)** gaseous decomposition products. **(c)** The progress of gas product amounts in the aspects of C, O, S formed in accordance with the number of O₂ moles. **(d)** Phase diagram according to the O₂ mole fraction and total chamber pressure from 0 to 10⁻³⁰ atm. The minimum pressure is 6.6×10⁻⁹ atm and the pressure range for selective oxidation ranged from 1.3×10⁻⁴ to 5.3×10⁻⁴ atm.

Figure 7.4 Structure evolution schemes of MoS₂ according to pressure, which affects the degree of selective C oxidation in MoS₂/C nanofibers.

Figure 7.5 Analysis to confirm redox control of Mo-S-C-O and reaction inducement of Mo sulfidation and C oxidation. **(a)** XRD and **(b)** XPS analysis to determine the pressure range of selective oxidation. Raman analysis which shows the increasing **(c)** stacking number of MoS₂ with decreasing C contents in nanofibers.

Figure 7.6 **(a)** Brunauer–Emmett–Teller (BET) specific surface areas of the MoS₂/C nanofibers according to the calcination conditions. **(b)** Comparison of the micropore size distribution between the MoS₂/C nanofibers using MP plot. **(c)** Mesopore size distribution of MoS₂/C nanofibers. Higher amounts of O₂ induced porosity in nanofiber structures after calcination in the Barrett-Joyner-Halenda (BJH) plot.

Figure 7.7 XPS analysis for investigating the chemical status of **(a)** Mo and **(b)** S.

Figure 7.8 FE-SEM, TEM images and reproduced images of MoS₂/C nanofibers for structure analysis. FE-SEM images illustrate the surfaces of nanofibers and nanotubes. TEM images illustrate the length, stacking number, alignment, and distribution of MoS₂ inside nanofibers under conditions of **(a)** Ar/H₂ gas, **(b)** pO₂ 0.1 Torr, **(c)** 0.2 Torr, **(d)** 0.3 Torr, **(e)** 0.4 Torr, **(f)** Stabilization + pO₂ 0.4 Torr calcination.

Figure 7.9 Thermogravimetric analysis (TGA) and differential scanning calorimetry (DSC) of electrospun ATTM+PAN nanofibers. These compare the extent of decomposition by full oxidation and full reduction under **(a)** air for combustion and **(b)** N₂ for pyrolysis.

Figure 7.10 MoS₂ nanotubes with high aspect ratios formed by a stable calcination process. TEM images with **(a)** low magnification to show overall morphology and **(b)** high magnification to show MoS₂ distribution. Cs-corrected TEM analysis provides **(c)** high resolution image and FFT analysis (inlet) of MoS₂ atomic array at the shell in the (002) direction. **(d)** Bright field image and FFT analysis (inlet) of MoO₂ phase at the inner part and **(e)** HAADF and EDS mapping of the shell of the nanotubes.

Figure 7.11 Phase investigation of MoS₂ nanotubes. **(a)** XRD analysis after stabilization + pO₂ 0.4 Torr calcination. TEM EDS analysis of **(b)** the inner part and **(c)** the shell part to investigate the distribution of MoS₂ and MoO₂. **(d)** Mo, S, O quantitative analysis for each of the sites. Cu has been detected due to the presence of the TEM grid. **(e)** Comparison of O atomic % between inner and shell parts. The inside showed a higher O atomic percent than did the shell of the nanotube. The shell part contains MoS₂ and inner part of the nanotubes contains MoO₂.

Figure 7.12 Statistical analysis which denotes the quantitative aspects of structure evolution of MoS₂. Average and standard deviation of MoS₂ structure information investigated by TEM images according to the **(a)** pressure (Ar/H₂ gas, pO₂ 0.1, 0.2, 0.3, 0.4 Torr, and stabilization + pO₂ 0.4 Torr) of **(b)** layer length, **(c)** stacking number and **(d)** isothermal time (1, 5, 10 h at pO₂ 0.3 and 0.4 Torr) of **(e)** layer length and **(f)** stacking number. Comparison of the growth modes between the lateral (length) and vertical (stacking number) directions during self-assembly of MoS₂ inside C nanofibers according to the pressure and time.

Figure 7.13 TEM images and reproduced images of MoS₂ in nanofibers for structure statistical analysis. The calcination time was varied at constant pressures of 0.3 and 0.4 Torr at a temperature of 800 °C. **(a)** 0.3 Torr 1 h, **(b)** 0.3 Torr 5 h, **(c)** 0.3 Torr 10 h, and **(d)** 0.4 Torr 1 h, **(e)** 0.4 Torr 5 h, **(f)** 0.4 Torr 10 h. As the isothermal time increased, MoS₂ layers are increasingly distributed near the surface of the nanofibers and aligned parallel to them.

Figure 7.14 Schematics for displaying the chemical reactivity difference between MoS₂ edge site and basal plane. Due to the high chemical reactivity of MoS₂ edge site, lateral growth shows the higher preference than vertical stacking.

Figure 8.1 (a) Schematics for displaying the 5 atomic component of Mo-W-S-C-O for the fabrication of MoS₂+WS₂ inside C nanofibers. (b) Ellingham diagram for displaying the chemical potential (Gibbs free energy) about the compounds formed in Mo-W-S-C-O system. (c) Reciprocal phase diagram of Mo-W-S-O.

CHAPTER 1

Introduction

1.1. Metal compound/carbon hybrid nanofibers

The demand for developing renewable energies is increasing to solve the energy and environmental problems originated from exhaustion and harmful wastes of fossil fuels (**Figure 1.1**). In energy harvesting and storage system such as water splitting, carbon dioxide (CO₂) reduction, fuel cell, and Li, Ni-ion battery, the dominant operating mechanism is based on electrochemical reaction between active material and guest material. The factors affecting the optimization of functionalities are ① surface to volume ratio related with the reaction area, ② electrically conductive collector formation, and ③ demonstration of physiochemical reaction control elements. One-dimensional (1D) nanofibers are ideal material which can satisfy these requirements. The nanofibers fabricated by electrospinning are receiving great attention due to high aspect (>1000), high production yield, versatility in the structure and phase control.

In metal (compound)/carbon nanofibers, nano-sized metal (compound) is an active material which can show high reactivity in electrochemical reaction (**Figure 1.2**). For

Chapter 1: Introduction

enhancing the performance of the devices, the efficiency of surface/interface reaction should be optimized. It is affected by the oxidation status of metal ion and structural aspects such as size, distribution, alignment. Carbon (C) is a supporter which forms and sustains the nanofiber shape after electrospinning and calcination. It is electrically conductive and acts as an anchoring site which affects the dispersion of active materials. C nanofibers can be produced by the carburization of polymer matrix such as polyacrylonitrile (PAN), poly-imide (PI), poly(vinyl alcohol) (PVA), poly(vinylidene fluoride) (PVDF), and pitch.^[1] According to the types of polymer matrix, free-standing nanofiber mat can be induced after calcination. During calcination under inert ambient, carburization induces the graphitization and it is related with the crystallinity. To enhance the electrical conductivity, the degree of graphitization of aromatic benzene ring should be intensified. In fact, mesophase-pitch based C fibers show higher conductivity than PAN based C nanofibers due to the different degree of graphitization. To further enhance the functionality of nanofibers by increasing chemical reaction efficiency, nanofluidic behavior, bi-functional properties, mechanical strength, the secondary nanostructures such as core/shell, hollow, and porous structures.^[2]

C nanofiber itself can be applied to electrode materials for electrochemical capacitors, anode electrode of Li-ion battery without active materials. In **Figure 1.3a**, as the calcination temperature increases from 700 to 850 °C, the electric double layer capacitance increases and it is over 150 F/g at the current density of 10 mA/cm². Especially, according to the various C based materials, such as activated C, carbon nanotube (CNT), electrospun C nanofiber after electrospinning shows higher adsorption capacity of metal ions (**Figure 1.3b**). In the case of Sn/SnO_x loaded C nanofibers in porous C nanofibers, it shows a good cyclability with higher capacity in

Chapter 1: Introduction

the anode of Li-ion battery (**Figure 1.3c,d**). The effect of metal compound based active materials on electrochemical activity has been studied in **Figure 1.3e,f**. Compared to the bare C nanofibers, MnO_x loaded nanofiber showed 1.5 times higher capacity. Therefore, in electrochemical reaction, the electrical conductivity of C nanofibers and precise control of active materials are critical for optimization of the performance.

Generally, previous researches about these heterogeneous catalysts were limited on the surface reaction kinetics between guest materials and catalysts which are composed of active material and supporter (**Figure 1.4a**). The quantum chemical calculations were biased to the prediction of optimal atomic arrangement for the performance optimization. In fact, trial-and-error based experiments were applied to fabricate those materials. Escaping from the conventional aspects of research, a new fabrication method which enables predicted synthesis for phase and structure control of metal compound/C hybrid nanomaterials will be suggested in this thesis. The types of active materials in C nanofibers can be classified metal/C, metal oxide/C, metal compound/C system (**Figure 1.4b**). In metal/C system, single or dual metallic species can be formed within C nanofiber. By the degree of C decomposition, the structures of metal can be controlled. In metal oxide/C system, oxygen (O_2) during calcination can interact with metal ion or C. Not only the structures of metal oxide, but also the oxidation number of metal ion can be modulated. Furthermore, according to the excess Gibbs free energy of mixing, and activity coefficient, metal oxide can be categorized into single cationic ($\text{M}_{1x}\text{O}_y + \text{M}_{2x}\text{O}_y$) or double cationic ($\text{M}_{1x}\text{M}_{2y}\text{O}_z$) system. In the case of metal compound/C system, the anions such as sulfur (S), phosphor (P), nitrogen (N), can be applied within the solid state nanofibers. In the case of O_2 ambient calcination for combustion based C decomposition, there are 4 atomic species.

Chapter 1: Introduction

For effective phase and structure control of metal compound, the redox reactions between them should be systematically studied. Especially, interaction between molybdenum (Mo) and S can induce two-dimensional (2D) layer structured molybdenum disulfide formation inside 1D C nanofibers.

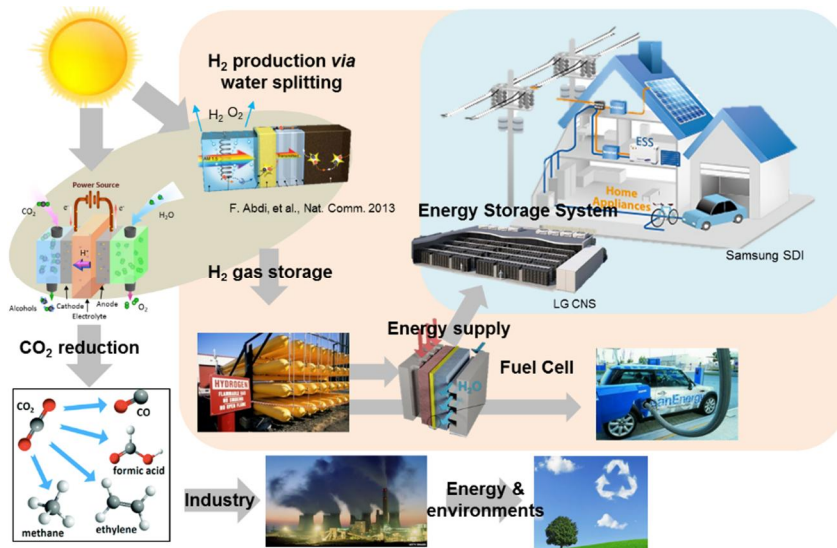


Figure 1.1. Renewable energy circulation from the sun-light, CO₂, and water resources.

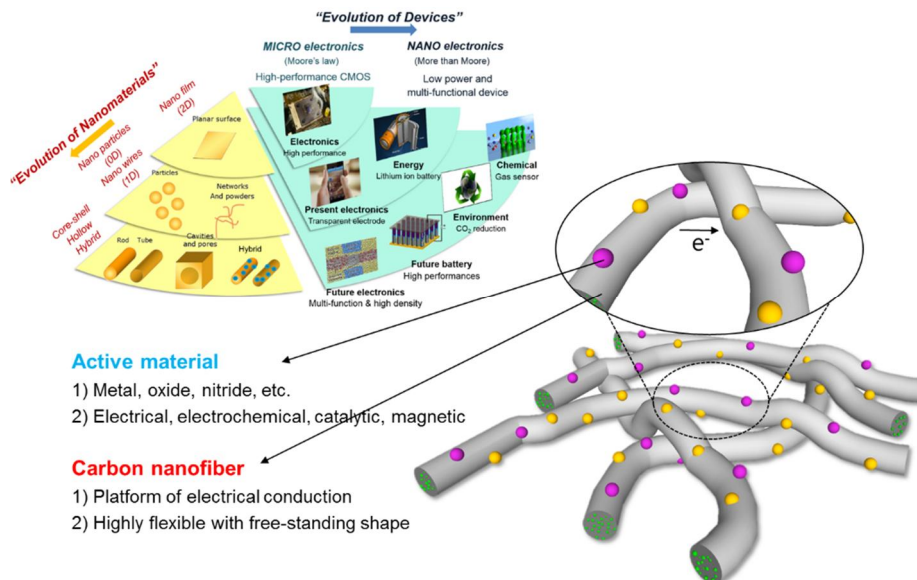


Figure 1.2. Schematics for displaying the components of metal (composite)/C hybrid nanofibers for energy and environmental application.

Chapter 1: Introduction

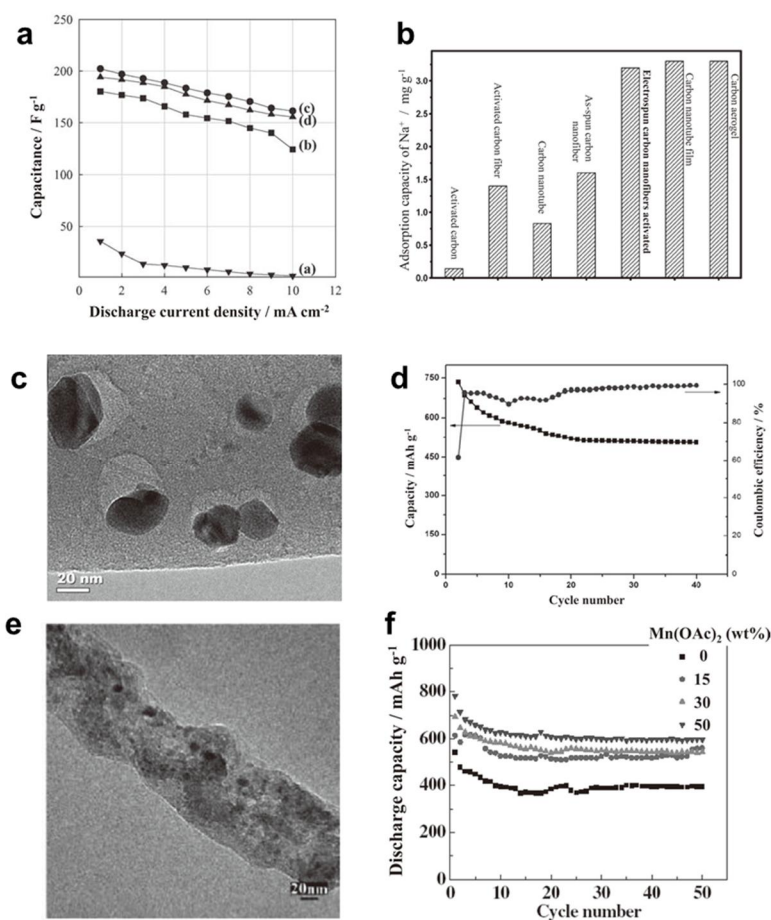


Figure 1.3. Effect of metal(composite) loading on C nanofiber properties. **(a)** Dependence of electric double-layer capacitance on discharge current density according to the calcination temperature,^[3] **(b)** Electrochemical adsorption capacity of Na ion,^[4] **(c)** TEM image of Sn/SnO_x containing C nanofibers, **(d)** Cycle performance in Li-ion battery with a current density of 30 mA/g,^[5] **(e)** TEM image of MnO_x-loaded C nanofiber, and **(f)** Cycle performance of Li-ion battery according to the loading amount of Mn(OAc)₂ precursor.^[6]

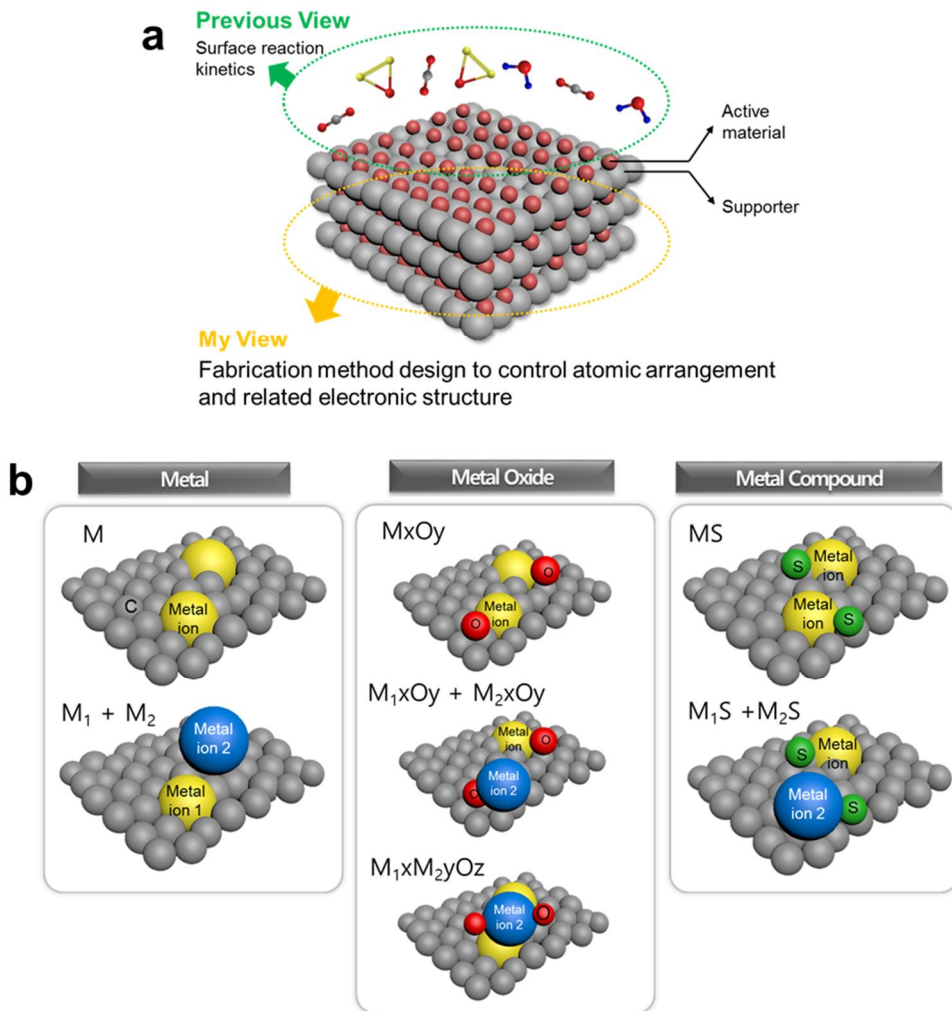


Figure 1.4. (a) The research scope of this thesis about the active material/supporter hybrid nanomaterials. It is fabrication method design to control atomic arrangement and related electronic structure. **(b)** Categorization of active material/C hybrid nanofibers according to the composition of functional materials.

1.2. Phase and structure control issues of metal/C nanofibers

1.2.1. Solution process based active material loading inside C nanofibers

Generally, electrospinning is the simplest and versatile technique for fabrication of 1D nanostructures. It has been mainly utilized for polymeric application such as membrane, water and air filter, tissue engineering, bio sensors, neural prosthesis, artificial heart valve, etc.^[7] When calcination process proceeds after electrospinning, polymer nanofibers can show electrical conductivity which has been considered in **Section 1.1**.^[1] Diversely functionalized metal compound/C nanofibers can be induced by the coexistence of electrically conductive C nanofibers with the metal compounds as an active material. In nanofiber, metal ions can be supplied in solution process before electrospinning.

First, the most straightforward method is a direct insertion of active materials into the polymer matrix + solvent solution (**Figure 1.5a**). It is hard to uniformly disperse inorganic material inside solution. In this case, the final product such as metal, oxide nanoparticles are directly included in nanofibers. For example, 20~200 nm size Ag nanoparticles were dispersed in polymer matrix.^[8] Yang, *et al.* studied the dispersion of CdTe quantum dots in PVP nanofibers.^[9] In these cases, the additional treatment with surfactant such as cetyltrimethylammonium bromide (CTAB) was required for nanoparticle dispersion. In addition to the metal or ceramic nanoparticles, CNTs can be directly-dispersed by this methodology. However, this methodology shows the limitations in low possibility of active material structure control, low dispersion, nozzle blocking problems.

Second, active materials can be precipitated inside C nanofibers by the gas-solid

Chapter 1: Introduction

reactions between calcination (**Figure 1.5b**). Unlike the direct-dispersion method, this method utilizes the metal precursor which contains metal ions. The process of gas-solid reaction is composed of co-dissolve metal salt and polymer into one solvent to make a homogeneous solution and electrospinning to induce metal precursor/polymer matrix nanofibers.^[10] PbS/C nanofibers could be fabricated by the reaction between H₂S gas and Pb acetate during calcination.^[11] Compared to direct dispersion method, it shows a possibility for structure and phase control due to the phase transformation of metal ion during calcination. Also, due to the high solubility of precursor in solvent, active materials are dispersed uniformly.

Third, in-situ photoreduction can generate metal nanoparticles in electrospinning solution (**Figure 1.5c**). After insertion of metal precursor into the solution, metal ion is reduced by photo reduction with UV irradiation. Park, *et al.* fabricated Ag nanoparticles embedded nanofibers by applying AgNO₃ as a metal precursor.^[12] According to the concentration of precursor and photoreduction time, the size of nanoparticle can be controlled. Finally, sol-gel method is utilizing the relative reaction between different precursors in solution (**Figure 1.5d**). These are primary method for applying active materials inside C nanofibers. For the optimization of electrical, electrochemical activities, the phase and structure control of metal compound/C nanofiber is required.

In previous researches, the structure control of metal compound/C nanofibers was enabled by process modification or additional treatment after calcination (**Figure 1.6**). By designing the dual-layered syringe needle tip and utilizing different properties (volatility, solubility) between inner and outer solutions during electrospinning, core/shell, hollow, porous structures can be induced. However, it shows the limitations for requirement of various raw materials according to the target structures. After

Chapter 1: Introduction

electrospinning, Kr⁺ ion beam irradiation can align the Ni nanoparticles inside C nanofibers. It is rather expensive process and can induce destruction of nanofiber structures by the high intensity of irradiation.^[13] After electrospinning and two-step calcination under air and H₂, atomic layer deposition (ALD) process has been applied for the formation of outer protective shell structure.^[14] These methods cannot control the structures of functional materials and C simultaneously. They show the low generality which is related with the fragmentary control for limited range of applications.

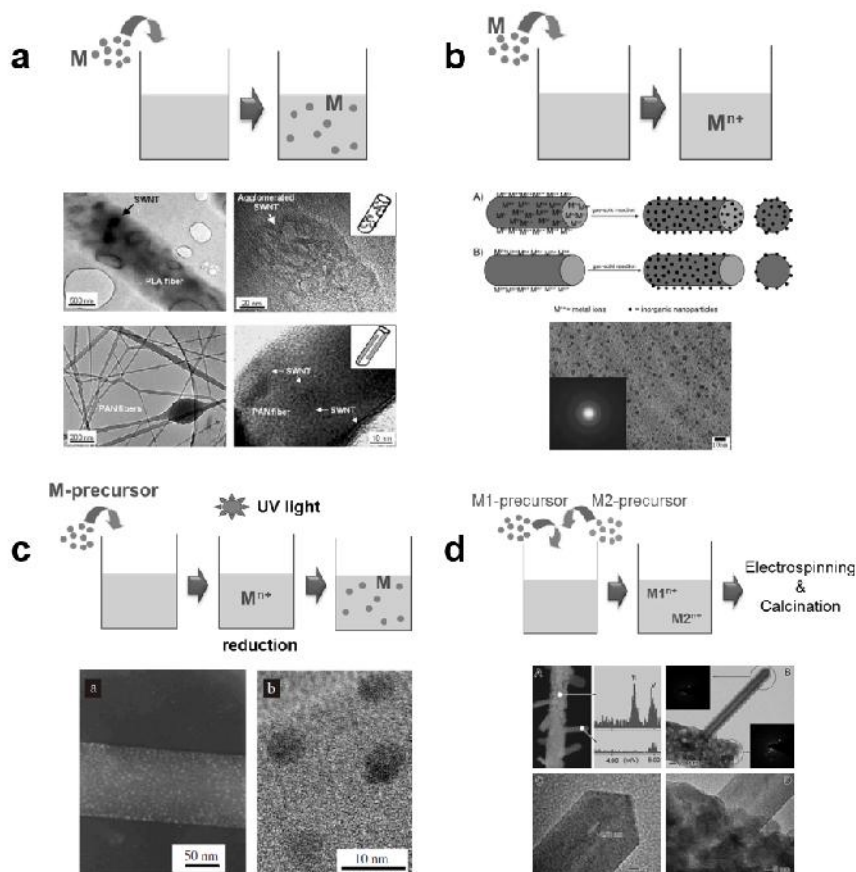


Figure 1.5. Electrospinning methodology for the fabrication of metal compound containing heterogeneous nanofibers. **(a)** Direct-dispersed electrospinning, **(b)** Gas-solid reaction, **(c)** In-situ photoreduction, **(d)** Sol-gel method.^[10]

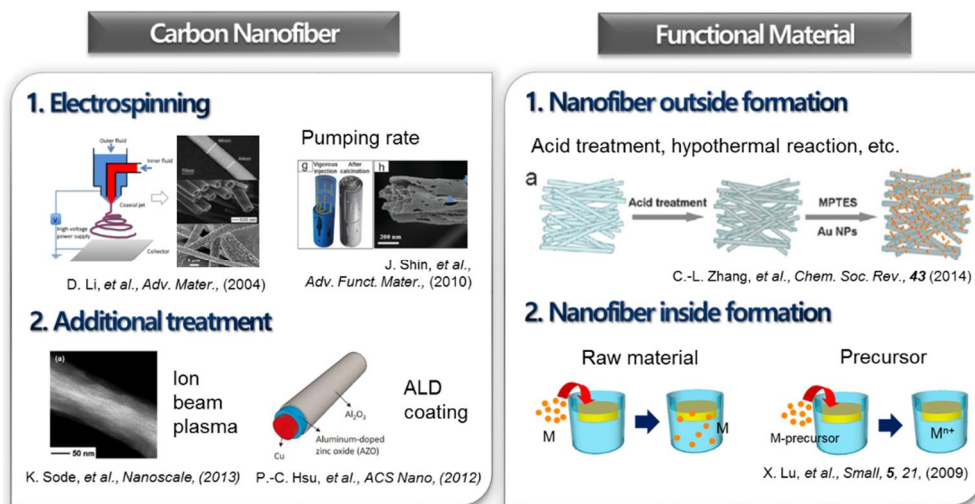


Figure 1.6. Previous researches for metal compound/C nanofiber structure control in the aspects of active material and C nanofibers.^[10,13–17]

1.2.2. Thermodynamics for phase control

Phase diagram enables to predict the phase evolution of materials according to the processing parameters such as pressure, temperature, and materials compositions. In the case of fabricating stable phase in phase diagram, it can be induced by controlling those processing parameters and materials compositions in bulk scale such as metallurgy. When the scale of material decreases to the nanoscale, the effect of surface energy term increases and it affects the Gibbs free energy for reaction.

There were previous attempts to predict the phase of nanoscale oxide materials by calculating the nanoscale phase diagram. **Figure 1.7a,b** are the phase diagrams induced by density functional theory (DFT) calculation to investigate the phase stability of Na_2O_2 , NaO_2 . When the dimension of nanomaterials decreased to 1~5 nm, the $p\text{O}_2$ for increasing oxidation number decreases (**Figure 1.7b**). It means that nanoscale materials oxidize easier than bulk scale materials. Lower surface energy of NaO_2 stabilizes small NaO_2 particles over Na_2O_2 particles.^[18] The chemical potential of O_2 gas according to the $p\text{O}_2$ can be defined as follows:^[18]

$$\mu_{\text{O}_2}(T, P_{\text{O}_2}) = E_{\text{O}_2}^{\text{total}} + \Delta H_{\text{O}_2}(T) - TS_{\text{O}_2}^{\text{expt}}(T) + k_B T \left(\frac{P_{\text{O}_2}}{P_{\text{O}_2}^0} \right) \quad (\text{Eq. 1.1})$$

where $E_{\text{O}_2}^{\text{total}}$ is the total energy of O_2 , ΔH_{O_2} is the enthalpy difference of O_2 gas, $S_{\text{O}_2}^{\text{expt}}$ is the entropy of O_2 gas at 1atm obtained from experiments. Also, ab initio calcination has been applied for the calculation of surface energy which affects the nucleation of the compound.^[19] **Figure 1.7c** shows the facet evolution according to the Mg ratio in calcite. For example, dominant facets of aragonite are expected as (001), (011), (010), and (110). **Figure 1.7d** is the kinetic diagram about the nucleation rate

Chapter 1: Introduction

and Mg:Ca ratio. They both reveals that crystalline facet can be theoretically predicted by the calcination of surface energy at nanoscale. The effect of nanoscale materials on oxidation status of metal oxide can be expanded to the Li oxide (Li_2O_2 , Li_3O_4 , LiO_2) in **Figure 1.7e,f**. There have been previous attempts to predict the phase evolution of nanomaterials by the considering the effect of surface energy to the Gibbs free energy. However, the size effect on phase transition between oxide has been mainly studied. It has not been investigated in multi-atomic component system for inducing selective redox reactions.

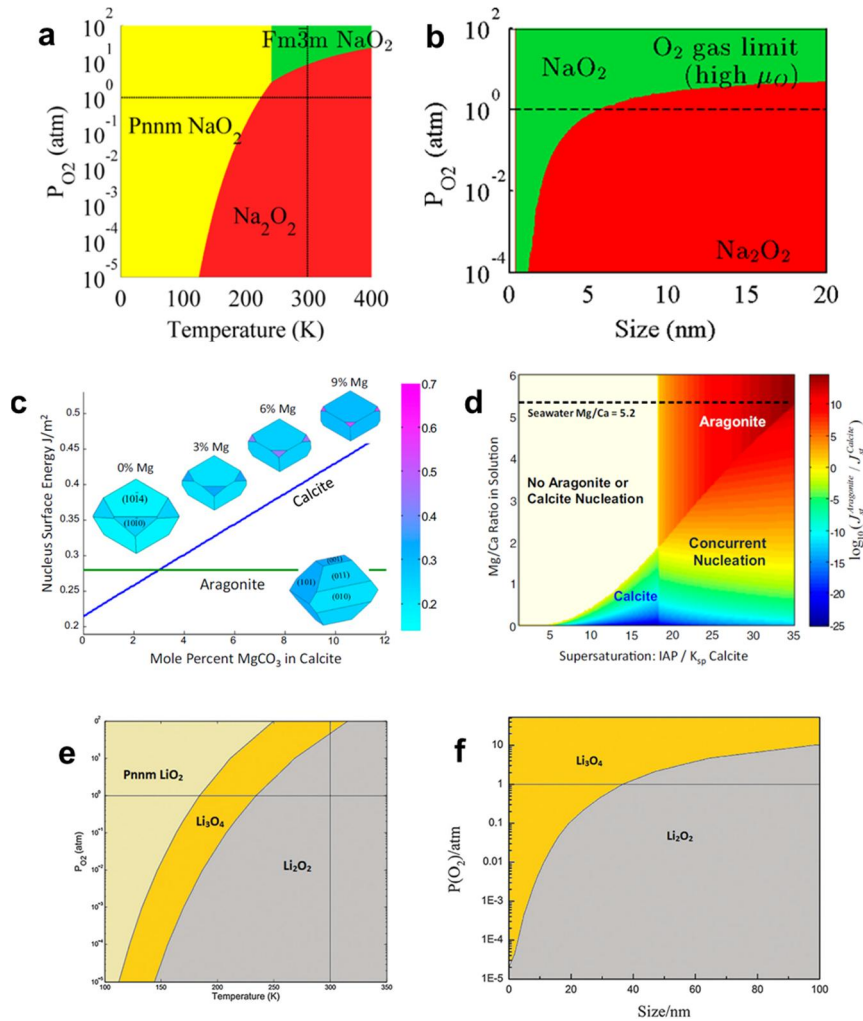


Figure 1.7. (a) Phase diagram of Na-O as a function of temperature and p_{O_2} . (b) Phase diagram of Na_2O_2 and NaO_2 at 300 K as a function of particle size and p_{O_2} .^[18] (c) Facet related morphology evolution of Mg-calcite and aragonite with a function of Mg^{2+} . (d) Kinetic phase diagram of the nucleation rate related with Mg:Ca ratio.^[19] (e) Bulk phase diagram of Li-O as a function of temperature and pressure. (f) Nano-scale phase diagram of Li_3O_4/Li_2O_2 .^[20]

1.2.3. Kinetics for atomic diffusion induced structure control

In the heterogeneous metal core and metal oxide shell system, outer diffusion of metallic species can be induced by the thermal annealing treatment. Interestingly, the stress originated by the difference of thermal expansion coefficient between inner metal and outer metal oxide can induce outer metal diffusion.^[21]

$$J = D[-\nabla c - \frac{c\nabla V}{kT}] \quad (\text{Eq. 1.2})$$

where D is diffusivity, ∇c is concentration gradient, ∇V is potential gradient. In the system of inner Cu and outer Al_2O_3 shell nanowire, this principle can be applied. Interestingly, according to the structural aspects of outer Al_2O_3 shell, the degree of outward Cu diffusion could be modulated.

The effect of porosity of oxide shell has been studied by Qin *et al.*^[22] In the case of alucone Al_2O_3 nanotubes, outer Cu diffusion was prevented after 650 °C calcination. However, in the case of porous Al_2O_3 nanotubes, calcination induced the outward Cu diffusion. **Figure 1.8** shows the thickness dependence of the degree of outward Cu diffusion. As the thickness of outer oxide shell decreases, enlarged Cu agglomerates formed and it means that the reaction controlled growth has been occurred with the high rate of Cu diffusion. This overall result indicates that the atomic diffusion related kinetics can be affected by the structural aspects of matrix material. It can give an insight to control the structure of active materials by controlling the density and porosity of C nanofibers.

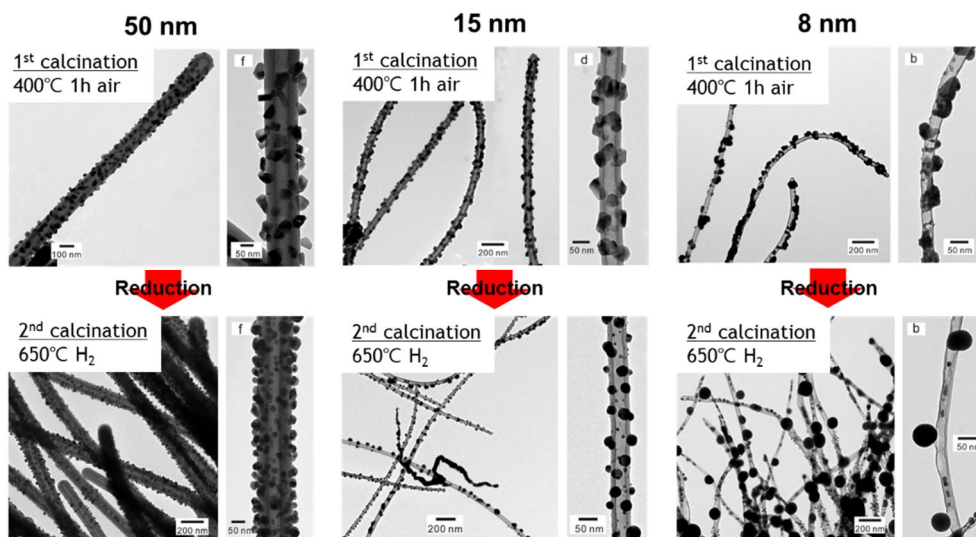


Figure 1.8. Effect of thickness of outer Al₂O₃ shell on the degree of outer Cu diffusion after calcination. As the thickness of oxide decreases, the degree of Cu diffusion increases and the size of Cu agglomerates increases.^[22]

1.3. Objective of the thesis

Electrospun metal compound/C nanofibers are receiving great attention for the energy and environmental applications due to their high surface to volume ratio, electrically conductive supporter, and tunable electrochemical properties of active materials. Metal compound acts an active material which shows high electrochemical activity and C plays a role as a supporter which contributes to the electric conduction with the high-aspect ratio structure. The structure and phase control of active materials are the most crucial factor for diversifying the functionality and optimizing the performance in various applications.

Active materials can be loaded in C nanofibers by solution process. Gas-solid reaction based metal precursor insertion exhibits higher utility in the aspects of phase and structure control of active materials compared to direct-insertion, in-situ photoreduction, and sol-gel method. The structure control of metal compound/C nanofibers was enabled by process modification such as coaxial eletrospinning or additional treatment after calcination such as ion beam irradiation, ALD coating. They showed the limitations of requirement of various raw materials and complex treatment, and fragmentary control for limited applications.

The objective of this thesis is the demonstration of novel fabrication methodology for controlling the phase and structure of active materials and C nanofibers by inducing selective redox reaction during calcination (**Figure 1.9**). Escaping from the control in solution process, it is based on gas-solid reactions which can realize the mass production of complex multi-atomic nanomaterials with high uniformity. Especially, through the thermodynamic consideration about the ΔG for reaction of the composition elements in materials, the processing parameters such as temperature and pressure, and materials

Chapter 1: Introduction

compositions can be predicted before experiment. It enables to selectively induce target phase by controlling the redox reaction between the elements. Furthermore, the diversified structures of active materials are induced by utilizing C as a descriptor to determine the internal migration rate of metal atoms. The rate of nucleation and growth of active materials can be adjusted by structure engineering of C by thermal decomposition process (**Figure 1.10**).

The first focus is the demonstration of selective C oxidation induced reductive metal morphology control. Compared to the oxidation ΔG of C, metals can be categorized into reductive and oxidative metals according to the ΔG for oxidation. In the case of reductive metals such as Co, Ni, Cu, Pt, etc., selective redox reaction which induce C oxidation and metal reduction. According to the pO_2 in this condition, full-filled C nanofibers with embedded metal nanoparticles, metal/C core/shell nanofibers, hollow and porous C nanofibers are formed. The mechanism of this structure evolution according to the pO_2 has been studied by the catalyzed C oxidation at the surface of metallic species.

The second focus is an in-depth study about the effect of C porosity on the structures of oxidative metallic species. The size and distribution of Sn, which shows high capacity active material in Li-ion battery anode, was modulated by managing the outward Sn diffusion during calcination. For minimizing the volumetric expansion based material degradation, the strategy for inducing Sn nanoparticles fully-embedded has been established. By utilizing the pressure equilibrium to derive reverse direction of Boudouard reaction, C porosity could be controlled by pyrolysis, unlike previous section. Optimized Sn/C nanofibers have been applied to the all-solid-state Li-ion battery anode.

Finally, selective redox reaction scheme has been verified in multi-atomic component system to control MoS_2 inside C nanofibers. The redox reactions of Mo-S-

Chapter 1: Introduction

C-O was categorized according to the pO_2 . Especially, at the pO_2 between ΔG of C and Mo oxidation, C is decomposed by combustion with MoS_2 formation. In ternary phase diagrams, Mo-S-C-O mole fraction was determined to form MoS_2 and gaseous C oxide such as CO and CO_2 . The calcination in this region induced to control MoS_2 structures by nucleation and growth process inside C nanofibers. According to the pO_2 , the vertical stacking and lateral growth of MoS_2 stacking unit has been controlled, and various MoS_2 structures such as length, stacking number, distribution, and alignment were induced.

In this thesis, it has been revealed that the structure and phase of metal compound/C nanofibers can be precisely controlled by the predicted parameters from the same metal precursor and polymer matrix nanofibers. This customized fabrication has a potential to tuning the properties of metal compound/C nanofibers for various applications such as electronic, chemical, energy, and environment fields (**Figure 1.11**).

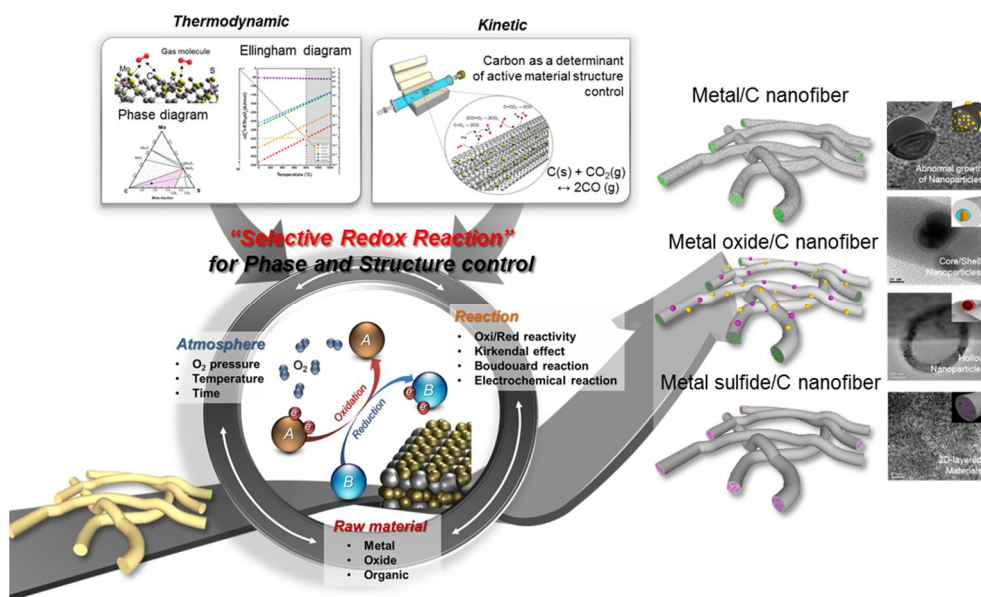


Figure 1.9. Overview of the thesis

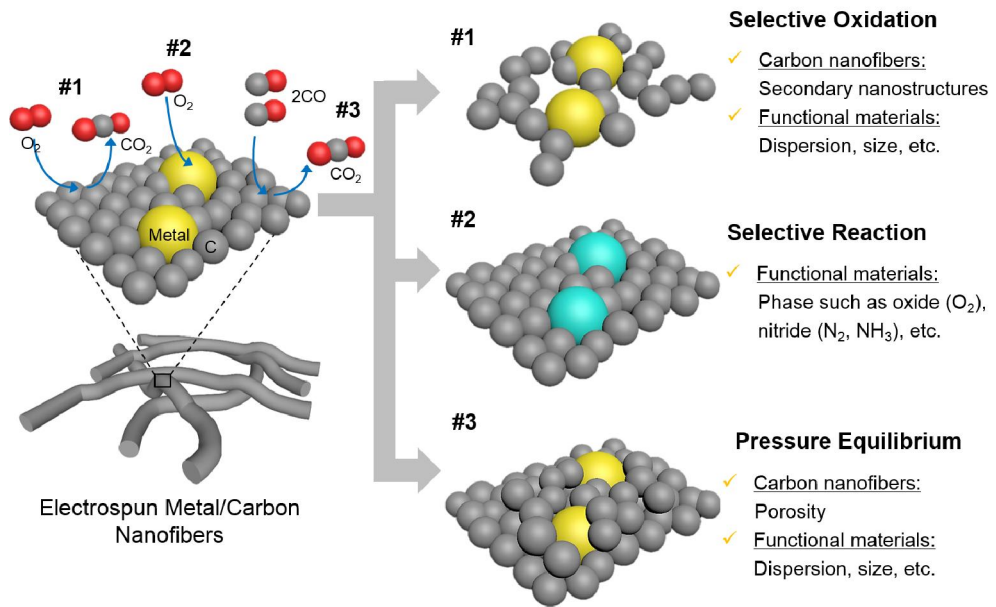


Figure 1.10. Gas-solid reaction based control scheme.

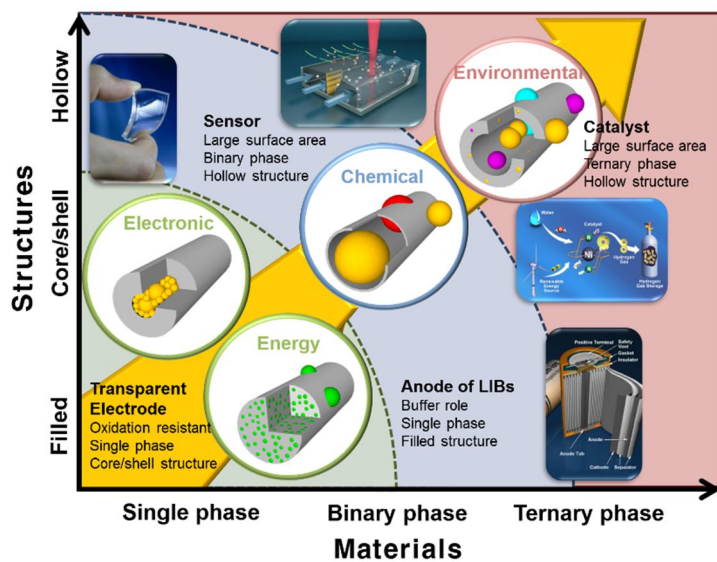


Figure 1.11. Potential applications of phase and structure controlled metal compound/C nanofibers.

1.4. Organization of the thesis

This thesis consists of eight chapters. In Chapter 2, nanofiber as 1D nanostructure, electrospinning and calcination process for nanofiber fabrication, selective reaction and Boudouard reaction for active material structure and phase control strategies, thermodynamic tools for prediction of processing parameters and materials composition, are introduced in Chapter 2. Chapter 3 includes the experimental procedure from fabrication to the investigation of properties. Chapter 4 describes the methodology about the selective C oxidation based reductive metal/carbon nanofiber structure control. Chapter 5 is an in-depth study about the mechanism of hollow C structure formation by the selective C oxidation in Chapter 4. Chapter 6 reports the pressure equilibrium based C porosity engineering for oxidative metal structure control. Chapter 7 describes the thermodynamic based reaction prediction of multi-component atomic system for kinetic van-der Waals solid structure control. Chapter 8 summarizes the results of this study and suggests the related future works in this study.

CHAPTER 2

Theoretical Background

2.1. Nanofibers

One dimensional (1D) nanostructured materials are receiving great attention due to their versatility and unique properties such as high electrical and thermal conductivity, in various applications. According to the aspect ratio, 1D nanostructured materials can be categorized into nanorod (aspect ratio < 20), nanowire (20 < aspect ratio < 1000), and nanofiber (aspect ratio > 1000) (**Figure 2.1**). Based on percolation theory, 1D nanostructured material with higher aspect ratio shows the merit in conductivity.^[23] This theory, which consider the electronic condition in 1D nanostructures, requires the assumption of charge transport along the wires and across the junctions between them. The conductivity of 1D nanostructures can be defined as follows:

$$\sigma \propto (N - N_c)^\alpha \quad (\text{Eq. 2.1})$$

where σ is conductivity and N_c is percolation threshold. This percolation threshold is related with the length (l) of 1D nanostructured material.

Chapter 2: Theoretical Background

$$l \propto \frac{1}{\sqrt{N_c}} \quad (\text{Eq. 2.2})$$

Based on this theory, the relationship between conductivity and aspect ratio can be considered. Unlike the conventional information about the electrical resistance of conductor, thinner and longer (high aspect ratio) materials show the higher conductivity (**Figure 2.2**). It can be explained by the extremely high resistance at the junction between 1D nanostructured materials. In the aspects of length of 1D conductor, the junctions are distributed in the series and total junction resistance can be defined as follows.

$$R_{Total} = R_1 + R_2 + R_3 + \dots \quad (\text{Eq. 2.3})$$

As the length of 1D conductor increases, the number of series junction decreases and it contributes to lowering the total resistance. Therefore, longer 1D nanostructured material show the merit of conduction. In the case of thickness of 1D conductor, the junctions are distributed in parallel and total junction resistance can be defined as follows.

$$\frac{1}{R_{Total}} = \frac{1}{R_1} + \frac{1}{R_2} + \frac{1}{R_3} + \dots \quad (\text{Eq. 2.4})$$

As the thickness of 1D conductor decreases, the number of parallel junction increases and it contributes to lowering the total resistance. Therefore, nanofibers with higher aspect ratio than nanowires exhibit an advantage for electrical conduction.

Chapter 2: Theoretical Background

Furthermore, compared to the nanowires fabricated from the solution of metal precursor and reducing agent, nanofibers are produced in higher yield with controllable dimensions (**Figure 2.3a**). The importance of diameter control on the aspect ratio can be explained in this manner. When the diameter of fiber decreased from 10 μm to 100 nm, the length can be increased from 13 km to 130,000 km from 1g polyethylene.^[24] The dimension of nanofiber shows a wide range of applications and their intrinsic properties such as Fermi level and reduction potential shift can be controlled (**Figure 2.3b**).^[24]

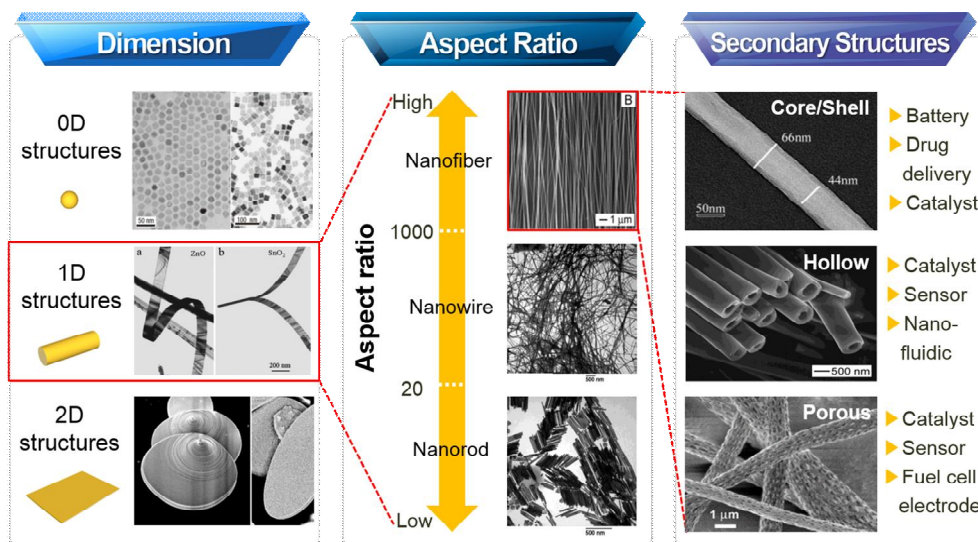


Figure 2.1. Categorization of nanomaterials according to the structural dimension and aspect ratio. Nanorod, nanowire, and nanofiber are 1D nanostructured materials and they can be classified by the aspect ratio. Secondary nanostructures such as core/shell, hollow, and porous can be induced in nanofibers with the aspect ratio of 1000.^[25]

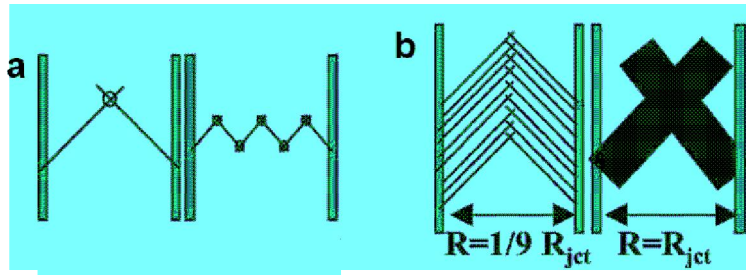


Figure 2.2. (a) Length and (b) thickness dependence of 1D nanostructured materials on percolation theory based electrical conduction.^[23]

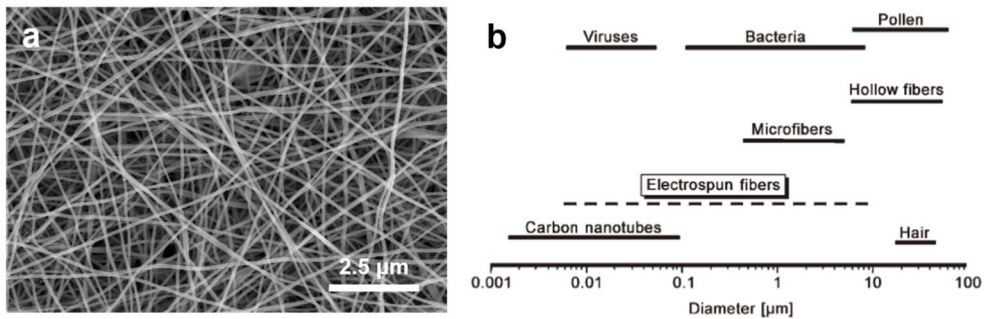


Figure 2.3. (a) FE-SEM image of nanofiber fabricated by electrospinning. (b) Dimension of electrospun nanofibers.^[24]

2.2. Electrospinning

Electrospinning is a fabrication method by applying uniaxial stretching of a viscoelastic jet derived from a solution.^[15] From the point of view to overcome the surface tension of a liquid with the electrical potential by Lord Rayleigh in 1882, the fabrication method of nanofibers was demonstrated with electrospinning.^[24] The solution for electrospinning is composed of polymer matrix to form the initial structures of nanofiber and solvent. As a polymer matrix, polyvinyl alcohol (PVA, $[\text{CH}_2\text{CH}(\text{OH})]_n$), polyvinyl pyrrolidone (PVP, $(\text{C}_6\text{H}_9\text{NO})_n$), polyacrylonitrile (PAN, $(\text{C}_3\text{H}_3\text{N})_n$), and poly(methyl methacrylate) (PMMA, $(\text{C}_5\text{O}_2\text{H}_8)_n$) can be applied. According to the types of polymer matrix, the forms of nanofiber mat can be differed such as PAN induces freestanding nanofiber mats while PVA induces high adhesion to the substrate. In order to diversify the functionalities of nanofibers, metal ions can be added with the form of metal precursor such as acetate, nitrate, chloride. For the phase control of metal ions in precursor, calcination should proceed. Solvent such as water, ethanol, N,N-dimethyl formamide (DMF) should solve the polymer matrix and metal precursor.

The electrospinning equipment is composed of syringe pump to precisely press the syringe with the solution loaded and voltage source to apply potential to the solution. By applying electric field to the solution, hemispherical shaped solution turns to the conical shape. It is affected by the interaction between surface tension and repulsive electrostatic force. With the surface tension is higher than repulsive electrostatic force, this conical shape is maintained. When the effect of repulsive electrostatic force become higher, charged jet is formed and nanofibers are fabricated by pumping the syringe. The collector is ground state and charged nanofibers can be deposited.

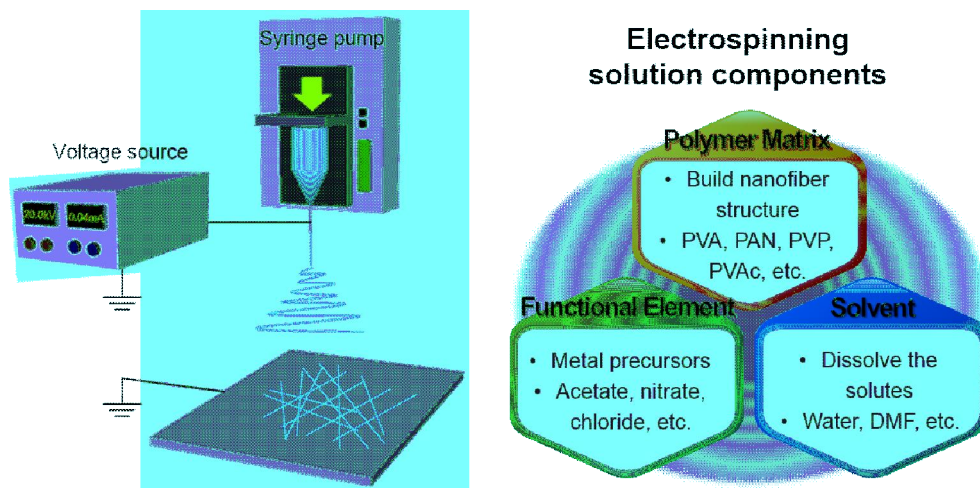


Figure 2.4. Electrospinning system for fabrication of nanofibers. Equipment is composed of voltage source, syringe pump, and collector. The solution for electrospinning is composed of polymer matrix to build nanofiber structure, metal precursor for functional element, and solvent to dissolve the solutes.

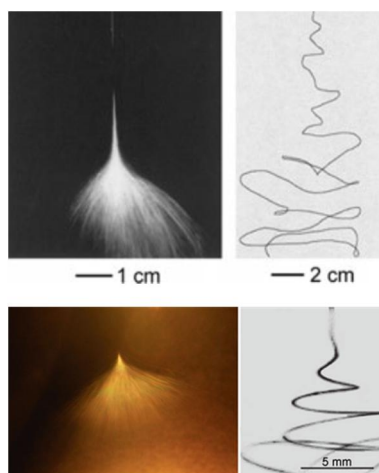


Figure 2.5. Optical images for displaying the whipping motion of electrospinning jet. ^[15,24]

2.2.1. Effect of solution parameters

The morphology of nanofibers is affected by the solution and processing parameters. Viscosity of solution, polymer concentration, molecular weight of polymer, solution conductivity, and surface tension are included in the solution parameters. Among them, viscosity dominantly affects the morphology of nanofibers. It is related with the bead formation at the electrospun nanofibers. Viscosity can be defined with the term of concentration and molecular weight of polymer matrix (PVA) as follows:

$$[\eta]C = 6.51 \times 10^{-4} M_w^{0.628} C \quad (\text{Eq. 2.5})$$

where η is viscosity, C is concentration, and M_w is molecular weight of polymer matrix. As the solution viscosity increases, bead structure disappears in nanofiber. Furthermore, there exists the relationship between the viscosity and surface tension of the solution.

$$\ln \sigma = \ln A + \frac{B}{\eta} \quad (\text{Eq. 2.6})$$

where η is viscosity, σ is surface tension, and A, B are constants. In the case of low viscosity, surface tension becomes dominant. Based on this condition, liquid drops form at the needle tip instead of fiber formation. It is a kind of dripping behavior. In contrast, in the case of high viscosity, viscosity of solution becomes dominant. It maintains a flow of polymer solution by cohesive natures. It shows the whipping behavior.

Chapter 2: Theoretical Background

2.2.2. Effect of processing and ambient parameters

The morphology of nanofibers can be affected by not only solution parameters, but also processing and ambient parameters. Processing parameters contain applied voltage, distance, and flow rate. As the applied voltage increases, the repulsive electrostatic force become dominant and it reduces the diameter of the nanofibers. The shape of initiating drop changes with voltage. Distance between the tip and collector have an intimate relationship with solvent evaporation. As the distance decreases, flatter shaped fibers are fabricated. In contrast, as the distance increases, rounded fibers are fabricated. Flow rate is directly related with the diameter of fibers. Beads can be formed due to short drying time when the flow rate is too high. Also, humidity and temperature play an important role in the evaporation of solvent during electrospinning. High humidity results in circular pores on the fibers.

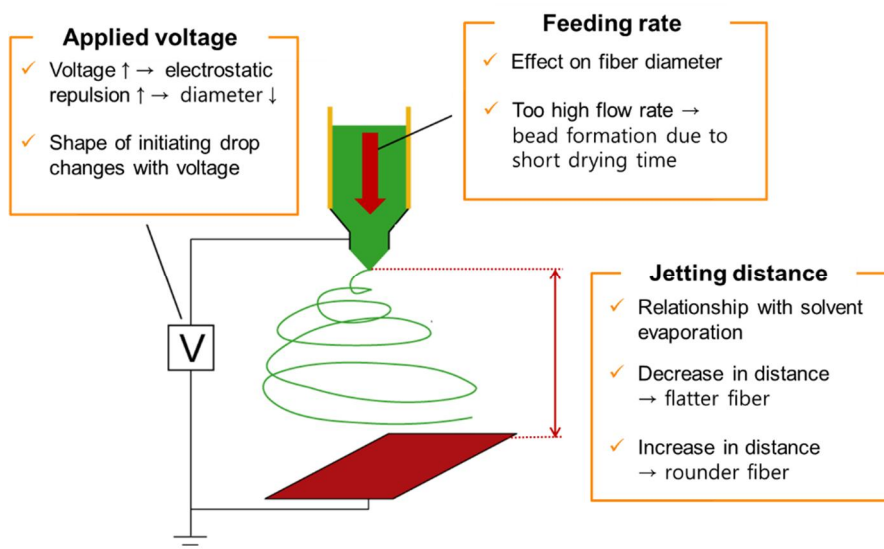


Figure 2.6. Effect of processing parameters such as applied voltage, feeding rate, and jetting distances on the morphologies of electrospun nanofibers.^[26]

2.2.3. Coaxial-Electrospinning

To expand the functionality of electrospun nanofibers, co-axial electrospinning has been developed by replacing the capillary with a coaxial nozzle (**Figure 2.7**). Through this, two solutions with different compositions can be pumped from the syringe at the same time. According to the combination of the various solutions types, core/shell, hollow, and porous nanofibers are fabricated. In the case of core/shell nanofibers, two solutions with different metal precursors should be supplied with the immiscible state (**Figure 2.8a**). It is for inducing the dual functionality of 1D structured nanomaterials. Also the viscosities of the solutions are different according to the displacement of core and shell part. To fabrication of hollow nanofibers, inner solutions should be immiscible mineral oil (**Figure 2.8b**). By inducing the different flow rate of the inner and outer solutions, the inner diameter and thickness of hollow nanofibers can be modulated. Due to the high surface to volume ratio, it shows the advantages in catalyst supports, optical waveguides, nanofluidic devices.^[25] In the case of porous structures, it requires the solution condition for miscible solvents with immiscible polymers (**Figure 2.8c**). It can exhibit remarkable performances in catalysis, gas sensors, fuel cell, solar cell, and battery electrodes.

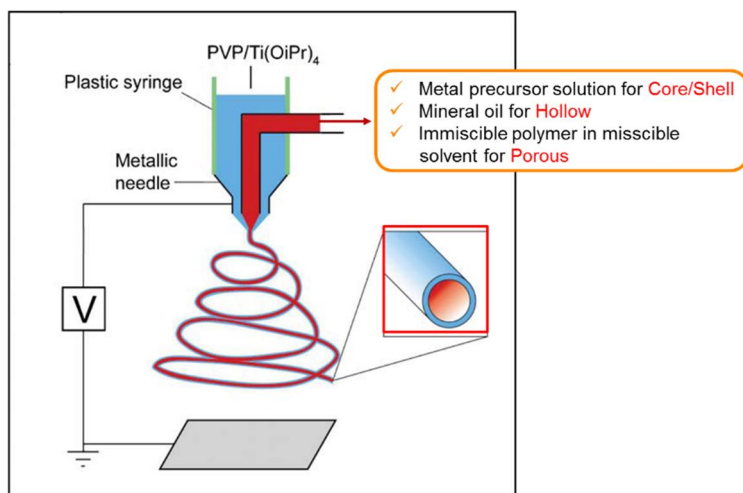


Figure 2.7. Schematic for indicating the coaxial electrospinning with the dual nozzle to simultaneously induce the flow of two solutions with the different composition. Based on this method, core/shell, hollow and porous nanofibers are fabricated.^[27]

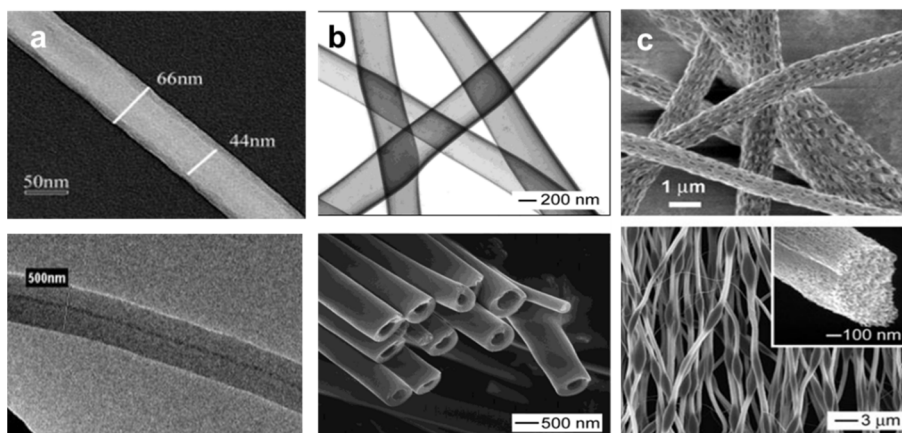
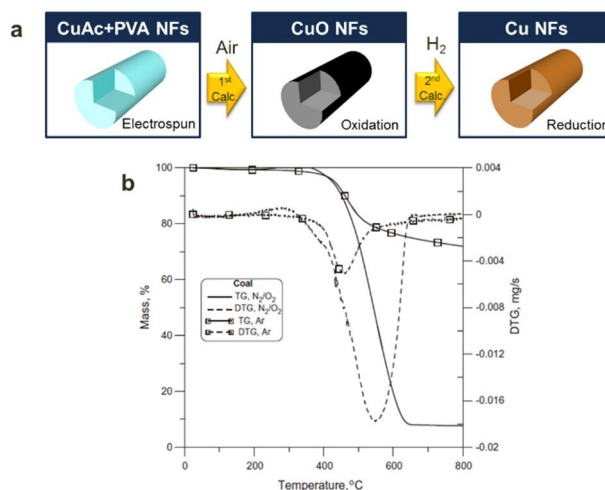


Figure 2.8. Structures of nanofibers fabricated by the co-axial electrospinning. (a) core/shell nanofibers,^[28] (b) hollow nanofibers,^[25] (c) porous nanofibers.^[25]

2.3. Calcination

After electrospinning of metal precursor + polymer matrix hybrid nanofibers, calcination is required for the phase transformation of metal ion in precursor and C decomposition to induce functionalities of nanofibers. Calcination is a thermal treatment under ambient controlled condition such as pO_2 to induce chemical status transformation. For example, after calcination of copper acetate (CuAc) + polyvinyl alcohol (PVA) nanofiber under air, copper oxide (CuO) nanofibers generate. After calcination under H_2 , Cu^{2+} in CuO is reduced to pure Cu. Types of C decomposition are divided into pyrolysis and combustion according to the ambient condition. Pyrolysis under inert ambient is breaking the bonding between C atoms and induce low molecular weight residual C. In contrast, combustion under air is the reaction between C and O_2 to form gaseous decomposition product such as C oxide (CO, CO_2).^[29]



Chapter 2: Theoretical Background

Figure 2.9. (a) Calcination process of electrospun copper acetate+polyvinyl alcohol nanofibers. (b) Thermogravimetric analysis (TGA) of coal for comparison of combustion and pyrolysis.^[29]

2.3.1. Selective oxidation

In metal/C composite system, the redox reactions such as oxidation and reduction can be independently applied to individual elements. Based on the standard Gibbs free energy (ΔG°) for oxidation of C, the oxidation tendencies of metal are classified as oxidative and reductive metal group in this thesis. In the case of oxidative metals such as Mg, Mn, Ti, the ΔG° for oxidation is lower than that of C and they preferentially oxidize than C. In contrast, in the case of reductive metals such as Cu, Co, Ni, the ΔG° for oxidation is higher than that of C and C preferentially oxidizes than those metal.

Based on the ΔG° difference between elements in metal/C composite system, redox reactions can be categorized into full reduction, full oxidation, and selective oxidation. Full oxidation is the condition for higher pO_2 than ΔG° for oxidation of metal and C. It induces the oxidation of metal and C under the high pO_2 condition such as calcination under air. Metal ion in nanofiber interacts with oxygen and metal oxide form. Oxidation based C combustion occurs and gaseous decomposition products such as CO, CO_2 form. Full reduction is the condition for lower pO_2 than ΔG° for oxidation of metal and C. Unlike the full oxidation, it induces the reduction of metal and C under the low pO_2 condition such as calcination under high vacuum ($<10^{-6}$ Torr), or inert ambient.

The specific pO_2 region between ΔG° of metal and C, the redox reaction can be applied selectively according to the oxidation tendencies of metal ion. In this thesis, this phenomenon has been defined as selective oxidation. In the case of reductive metal/C, metal reduction and C oxidation are induced. It enables to decompose C with combustion and formation of pure metal. In contrast, in the case of oxidative metal/C,

Chapter 2: Theoretical Background

metal oxidation and C reduction are induced. It induces reduction based pyrolysis with residual C and metal oxide formation (**Figure 2.10**).

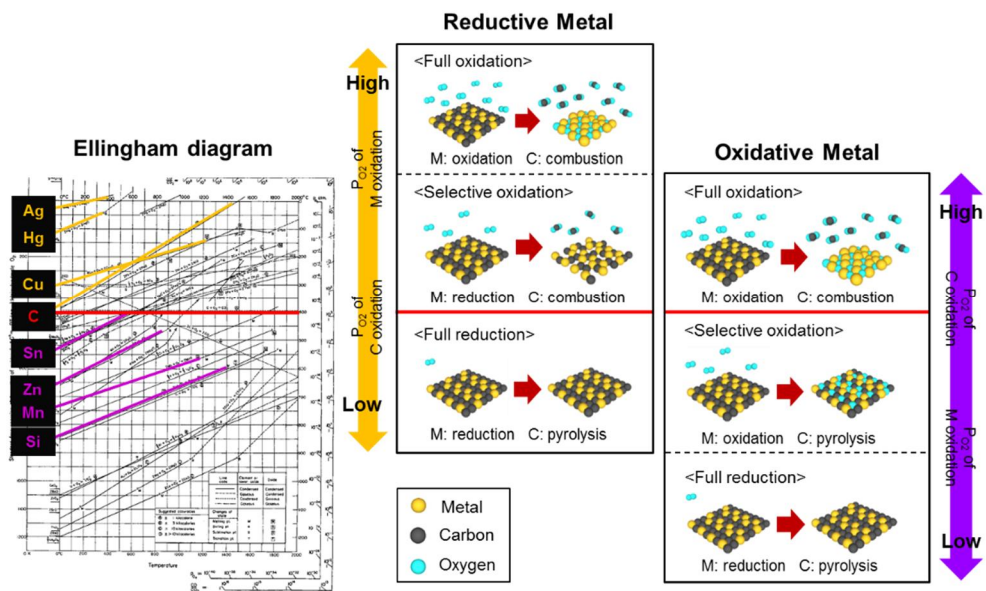


Figure 2.10. Categorization of redox reactions of metal and C according to the Gibbs free energy of oxidation in Ellingham diagram. Aspects of phase transformation of metal ion and C decomposition are classified as full oxidation, full reduction, and selective oxidation.

2.3.2. Boudouard reaction

The Boudouard reaction is a redox reaction of carbon monoxide (CO) and carbon dioxide (CO₂) according to the following chemical equilibrium: $C (s) + CO_2 (g) \leftrightarrow 2CO (g)$.^[30–32] It provides a theoretical background of chemical metallurgy in metal refining process by gas-solid reaction based carbothermic reduction. The thermodynamic phase stability of iron (Fe) and iron oxide (Fe₂O₃, Fe₃O₄, and FeO) is determined from the pCO/pCO₂ equilibrium ratio, which is related to oxygen partial pressure (pO₂).^[33] Generally, the activation energy of Boudouard reaction is range from 130 to 370 kJ/mol while the activation energy of iron oxide reduction by CO:CO₂=90:10 is 47 kJ/mol. In **Figure 2.11**, the P_{CO}/P_{CO2} shows a deviation from FeO-Fe equilibrium to Boudouard reaction. As the temperature increases from 1000 to 1200 °C, the Boudouard reaction control shows a decreased degree. This diminishing rate-surface area showed a decrease in Boudouard reaction with increased temperature. However, the reduction rate increases as the temperature increases.

Mechanistic reaction between metal oxide and gaseous intermediates (CO, CO₂) is governed by the Boudouard reaction. The surface area of solid C sources – such as char, coke, and graphite – also affects the reaction kinetics. It is known that carbothermic reduction rate increases with decreasing C particle size, increasing C contents, and the presence of Boudouard reaction agents. This principle has been applied to control phase and structure of nano-sized metal (composite)/C hybrid materials, where surface energy distorts the expected behavior of bulk-scale production. In nanoscale, not only the phase but also the structure can be controlled *via* dynamic motion of solid elements accompanied by the behavior of gas molecules.

We demonstrate this intriguing phenomenon as a ‘nanoscale Boudouard reaction’,

Chapter 2: Theoretical Background

which tunes nanoscale gas reaction by pressure and temperature. Typically, for the reduction of metal ions in the precursor, it has long been believed that a reducing environment such as H₂ gas or high vacuum (<10⁻⁵ Torr) is required. However, the insertion of a guest material (C) with higher oxidation tendency than target material (metal) enables the carbothermic reduction of metal ions.^[2]

Figure 2.12 represents the applying the Boudouard reaction for the porosity control of C based nanomaterials. In the case of calcination under high vacuum induced by continuous extraction of gas in chamber by rotary and turbo molecular pump, During this calcination, the pressure of chamber is constant and there is no preference in Boudouard reaction. In the Ar calcination, the pressure of chamber increases due to the confined chamber condition, increasing temperature, and gaseous decomposition products. For pressure equilibrium of chamber, Boudouard reaction proceeds reverse direction to lowering the molar number of gaseous molecules from 2CO (g) to CO₂ (g). It induces the formation of C (s) from 2CO (g) with the generation of CO₂ (g). It decreases the porosity of C nanofibers.

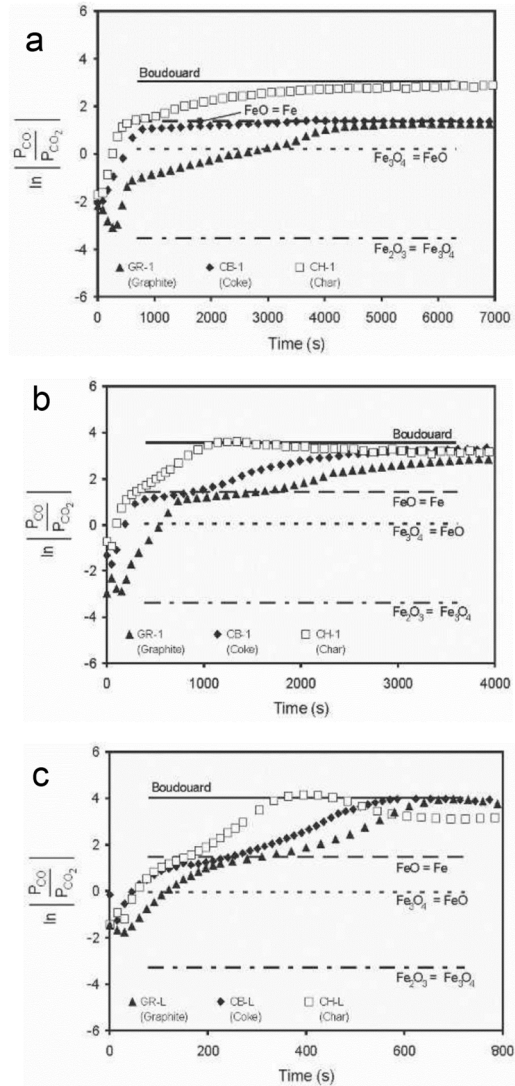


Figure 2.11. Reaction off-gas P_{CO}/P_{CO_2} for graphite, coke, char with lime additions at the temperatures of (a) 1000 °C, (b) 1100 °C, (c) 1200 °C.^[33]

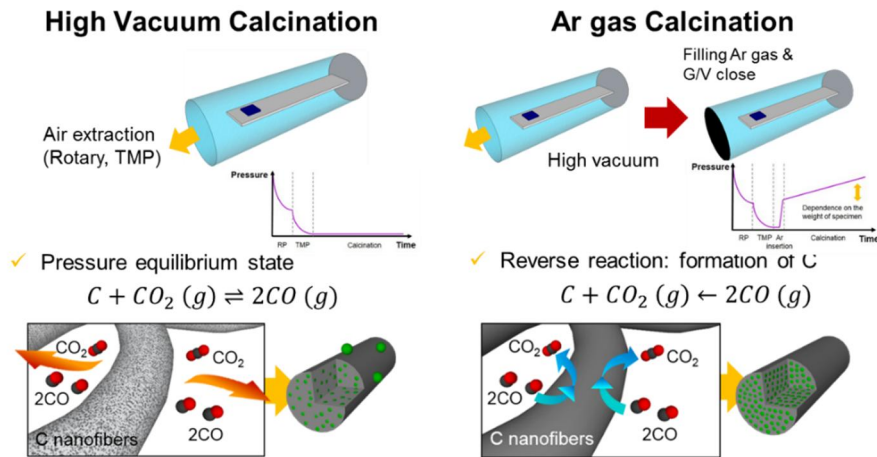


Figure 2.12. Application of Boudouard reaction to control the porosity of C nanofibers according to the pressure equilibrium of the chamber. In high vacuum calcination, overall chamber pressure is constant. There is no preference in Boudouard reaction. In Ar gas calcination, overall chamber pressure increases and reverse Boudouard reaction proceeds.

2.4. Thermodynamic tools for predictive synthesis

Phase diagram is a framework to predict the equilibrium phases at the specific condition such as temperature and time. In my thesis, phase diagram such as binary, ternary, quaternary system was applied to the prediction of materials composition in the fabrication of multi-atomic component nanomaterials. In the case of calcination for inducing selective oxidation of metal/C nanofibers, three components of metal-C-O are included in the system and ternary phase diagram needs to be studied. At the specific processing conditions such as pressure and temperature, which were induced from the Ellingham diagram, the Gibbs phase rule can predict the maximum three phases in the any portion of elements. In ternary phase diagram, the elements at the corner are in the state of stable formation when they compose the system. Materials range of three phases equilibrium in ternary phase diagrams is displayed as triangle in isothermal section. Based on the thermodynamic database about the Gibbs free energy, tie lines between two phases are determined in ternary phase diagram. The phases displaced on tie lines are stable according to the mole fraction between the elements. Based on Gibbs phase rule, the tie lines should not be overlapped each other.

Chapter 2: Theoretical Background

2.4.1. Ellingham diagram

Ellingham diagram denotes the standard Gibbs free energy (ΔG°) of metal compound formation with the variables of temperature and related partial pressure of gaseous components such as oxygen (O_2), carbon monoxide (CO), carbon dioxide (CO_2), and hydrogen (H_2). The ΔG° of the components with various metal ion cations is defined as follows:^[30]

$$\Delta G^\circ = A + BT \quad (\text{Eq. 2.7})$$

where the constant A is temperature-independent standard enthalpy change of the reaction, ΔH° , and the constant B is related with the temperature-independent standard entropy change of the reaction, ΔH° .

The left y-axis denotes the standard Gibbs free energy of compound formation (ΔG°) and right y-axis denotes the oxygen partial pressure (pO_2) in **Figure 2.13**. ΔG° and pO_2 can be matched by linking the extended line at the specific temperature of x-axis. They show the relationship as follows:^[30]

$$\Delta G^\circ = RT \ln pO_2 \quad (\text{Eq. 2.8})$$

where R is gas constant, and T is temperature of the system. By comparing the ΔG° values of compounds, the preference of oxidation and reduction between the elements can be determined in Ellingham diagram. Furthermore, the ΔG° of various compounds such as oxide, nitride, sulfide, carbide, etc. is compared according to the temperature.

Chapter 2: Theoretical Background

2.4.2. Ternary phase diagrams

In ternary phase diagram, the length of side indicates the composition of the elements such as mole fraction, mass fraction, and is equal to the one hundred.^[34] The composition of the compound can be induced by the distance from the three sides of triangle according to the elements. When the tie line is formed at the side of triangle, the mole fraction of elements is calculated by lever rule. According to the distribution of tie-lines, ternary phase diagrams can be classified. When the tie line is linked with specific phase compounds and element at the corner, it is specific phase dominant phase diagram. However, when the tie-lines are linked between the compound phases, it is no-phase dominant phase diagram. R. Beyers, *et al.* utilized this Gibbs phase rule to categorize the reaction aspects in metal-Ga-As system and investigated the phase equilibria.^[35] This kind of phase diagram classification can be understood with this point of view. **Figure 2.14a-c** show the specific phase dominant phase diagram. When the tie lines are linked with the specific phase and element, equilibrium phase generally includes the specific phase in all materials composition because of the phase rule which concerns no overlapping between tie-lines. However, in the case of 'no phase dominant', tie lines are linked with the composite phase, not element (**Figure 2.14d**). Based on Gibbs phase rule, the product phases can be varied according to the elemental mole fraction. It is lack of any tie-lines between a binary compounds and third element remains. This principle can be generally applied to mutl-atomic component system. For example, *K. J. Hubbard, et al.* studied M-Si-O system where M is the metal such as Ti, Zr, Ta, Mo, and W.^[36] In this case, the phase diagrams of M-Si-O system can be classified into SiO₂ dominant, no phase dominant, metal oxide dominant cases according to the formation of tie-lines between elements and

Chapter 2: Theoretical Background

compounds (**Figure 2.15**). The possible reactions between them are defined as follows:^[36]



When the Eq (2.9) proceeds forward direction due to higher oxidation tendency of Si than metal, Eq (2.11) should be considered. When $\Delta G < 0$, no phase dominant phase diagram is induced. However, if the condition is $\Delta G > 0$, SiO_2 dominant phase diagram generates. In contrast, if the Eq (2.9) proceeds reverse direction, Eq (2.10) needs to be considered in terms of ΔG . When the Eq (2.10) proceeds forward direction by the condition of $\Delta G < 0$, metal oxide dominant phase diagram is induced. Therefore, it can be determined that the aspect of phase production is varied according to the thermodynamic reaction Gibbs free energy. If M-Si-O system contains more than one oxide compound, the oxide formation ΔG should be applied for determining the phase diagram. Furthermore, if the system contains multiple silicide, the silicide formation ΔG needs to be studied.

Generally, for the calculation of ternary phase diagrams, CIS equation, Kohler and Toop equations are applied (**Figure 2.16**). CIS equation is based on statistical mechanical perturbation theory. The excess Gibbs free energy of ternary element system with the components 1, 2, 3 can be defined as follows:^[37]

$$g^E = \sum_m \sum_{n < m} \Phi_{11(mn)} Y_m Y_n + \sum_{m \neq n} \Phi_{21(mn)} Y_m^2 Y_n + \sum_{m < n} \Phi_{21(mn)} Y_m^2 Y_n^2 - \left(\Phi_{21(12)}^{\frac{1}{3}} + \Phi_{21(13)}^{\frac{1}{3}} \right) \left(\Phi_{21(23)}^{\frac{1}{3}} + \Phi_{21(21)}^{\frac{1}{3}} \right) \times \left(\Phi_{21(31)}^{\frac{1}{3}} + \Phi_{21(32)}^{\frac{1}{3}} \right) Y_1 Y_2 Y_3 + \sum_{m \neq n < k} 2 (\Phi_{22(mn)} \Phi_{22(mk)})^{1/2} Y_m^2 Y_n Y_k \quad (\text{Eq. 2.12})$$

Chapter 2: Theoretical Background

where g^E is excess Gibbs free energy after solution mixing, Y is equivalent ionic fractions. Kohler and Toop equations are defined as follows.^[37]

$$g_{(P)}^E = (1 - X_3)^2 g_{(a)}^E + (1 - X_1)^2 g_{(b)}^E + (1 - X_2)^2 g_{(c)}^E \quad (\text{Eq. 2.13})$$

$$g_{(P)}^E = \frac{X_1}{X_1 + X_3} g_{(a)}^E + \frac{X_3}{X_1 + X_3} g_{(b)}^E + (1 - X_2)^2 g_{(c)}^E \quad (\text{Eq. 2.14})$$

Those equations are exact in the circumstance of regular solution. Especially, Kohler equation has an advantage of being symmetrical among the three components. In the case of unsymmetrical component, the Toop equation is preferred. The CIS equation applies equally to charge symmetrical and unsymmetrical system and is generally preferred in fused salt solutions. However, in the case of solid solutions, theoretical basis for CIS equation no longer holds.

Based on this phase diagram categorization, we can predict the phase of products according to the mole fraction of the elements placed at the corner of triangle. It can be a thermodynamic prediction tool to induce specific mole fraction to induce phase control and related spontaneous atomic assembly.

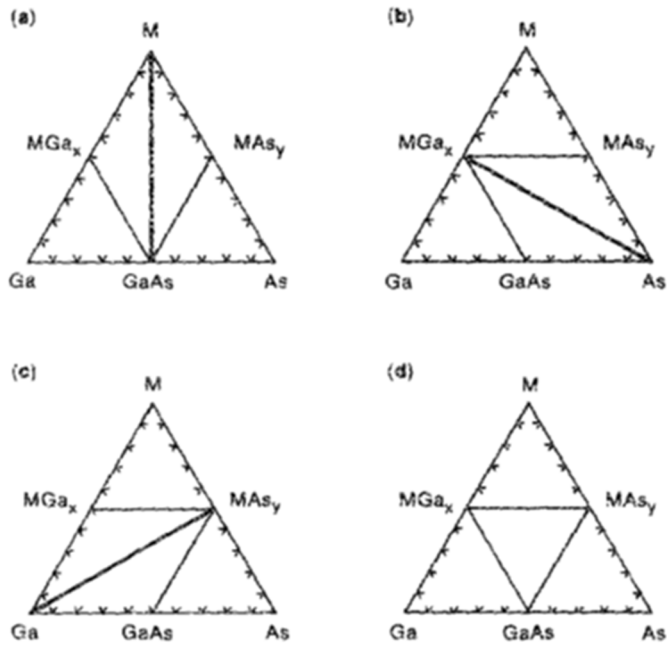


Figure 2.14. Ternary phase diagram classification according to the distribution of tie-lines. (a) GaAs dominant, (b) MGa_x dominant, (c) MAs_y dominant phase diagram, (d) No phase dominant phase diagram.^[35]

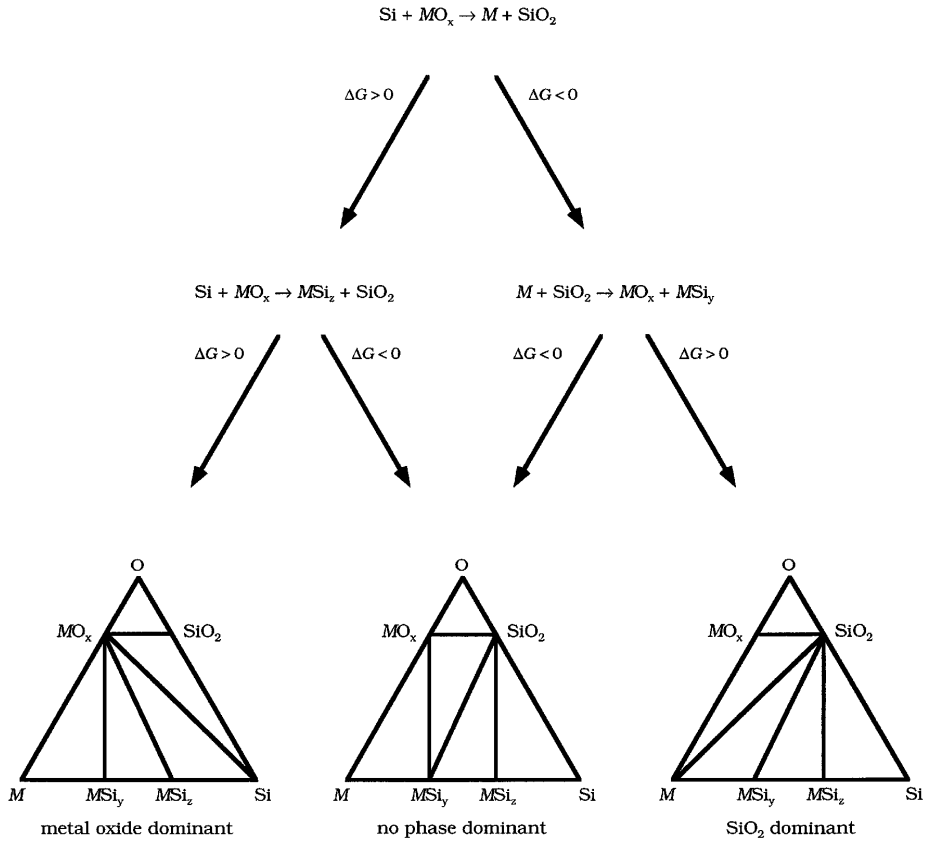


Figure 2.15. Effect of Gibbs free energy of the reaction between compounds on the types of thermodynamic ternary phase diagram. According to the reaction activity between elements, metal oxide dominant, no phase dominant, SiO₂ dominant phase diagrams are determined with the assumption of no ternary phases (MSi_xO_y) and only one M_x phase.^[36]

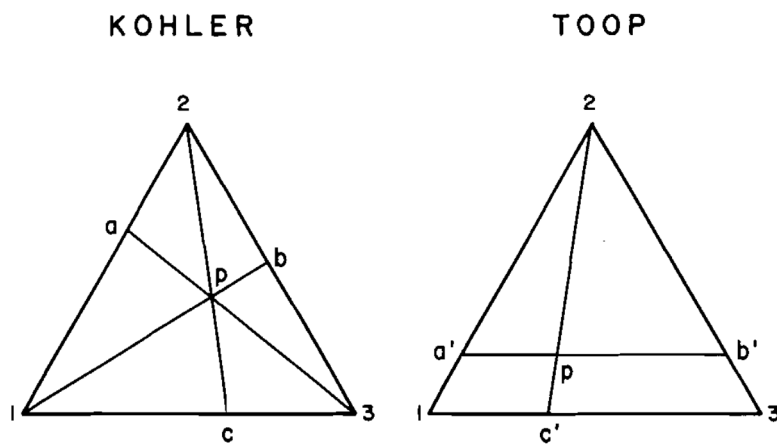


Figure 2.16. Comparison of Kohler and Toop equation theories for the demonstration of ternary phase diagrams.^[37]

2.4.3. Reciprocal phase diagram

Generally, reciprocal phase diagrams contain two cations and two anions. Although there exist 4 atomic components, one degree of freedom decreases due to the charge neutrality. In reciprocal phase diagrams, x, y axis represents the composition of cation and anion. The corners are the compounds formed by combination of cation and anion with maintaining the charge neutrality. Among the principles to induce ternary phase diagrams, CIS equation has been applied for the demonstration of reciprocal phase diagram from the binary system.^[37] In **Figure 2.17**, Excess Gibbs free energy at the point P can be plotted by the simultaneous consideration of cationic (X_N) and anionic (X_Y) fraction. By reducing the one degree of freedom in reciprocal phase diagrams, it enables to predict the equilibrium phase at specific mole fraction of the elements. The excess Gibbs free energy in reciprocal phase diagrams is defined as follows:^[37]

$$g^E = Y_M Y_N \Delta G^{EX} + (Y_M g_M^E + Y_N g_N^E + Y_X g_X^E + Y_Y g_Y^E) + Y_M Y_N Y_X Y_Y \Lambda \quad (\text{Eq. 2.15})$$

where g_M^E , g_N^E , g_X^E , g_Y^E is excess equivalent Gibbs free energies at the edge of reciprocal phase diagram. This reciprocal phase diagram can be applied in multi-cation and anion system.

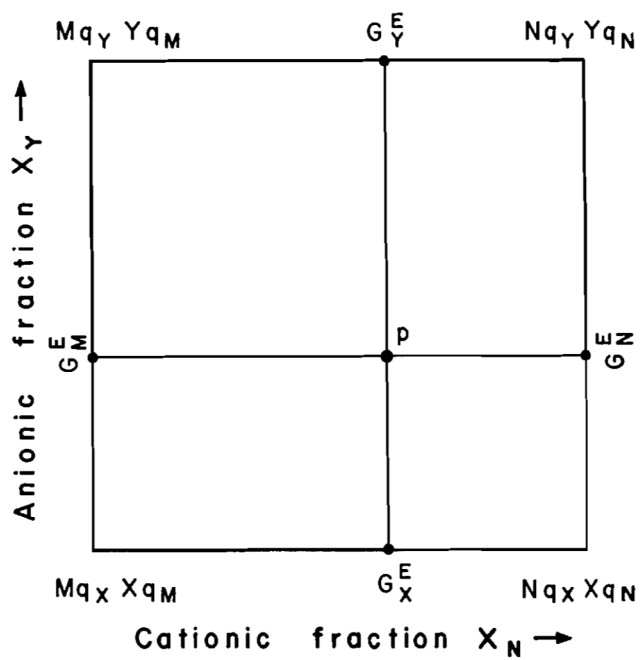


Figure 2.17. Composition square of reciprocal phase diagrams in the geometrical basis of the CIS equation.^[37]

2.4.4. Relationship between phase diagram and Ellingham diagram

Phase diagram is based on the calculation about the stability of compound phase at the specific condition such as atomic mole fraction, temperature, and pressure in multi-atomic components. It uses Gibbs free energy (ΔG) which considers the states of mixing between elements.

Ellingham diagram denotes the standard Gibbs free energy (ΔG^0) at the specific pressure and temperature conditions. It is based on the states of pure system. Therefore, it is used to determine the preference of the reactions such as oxide, sulfide, nitride, carbide formation. The relationship between phase diagram and Ellingham diagram can be understood by the Gibbs free energy and standard Gibbs free energy (Eq. 2.16).^[30]

$$\Delta G = \Delta G^0 + RT \ln a_i \quad (\text{Eq. 2.16})$$

It can be expanded by the definition of Gibbs free energy with enthalpy and entropy relationship. For example, with the elements of A and B, total Gibbs free energy can be defined by the following equation (Eq. 2.17).^[30]

$$G = X_A G_A + X_B G_B = X_A (G_A^0 + RT \ln a_A) + X_B (G_B^0 + RT \ln a_B) = X_A G_A^0 + X_B G_B^0 + RT (X_A \ln a_A + X_B \ln a_B) = X_A G_A^0 + X_B G_B^0 + RT (X_A \ln X_A + X_B \ln X_B) + RT (X_A \ln \gamma_A + X_B \ln \gamma_B) \quad (\text{Eq. 2.17})$$

Figure 2.18 directly shows the difference between the Gibbs free energy in Ellingham diagram and phase diagram. The Gibbs free energy in phase diagram considers the activity term which is originated from the mixing between different elements.

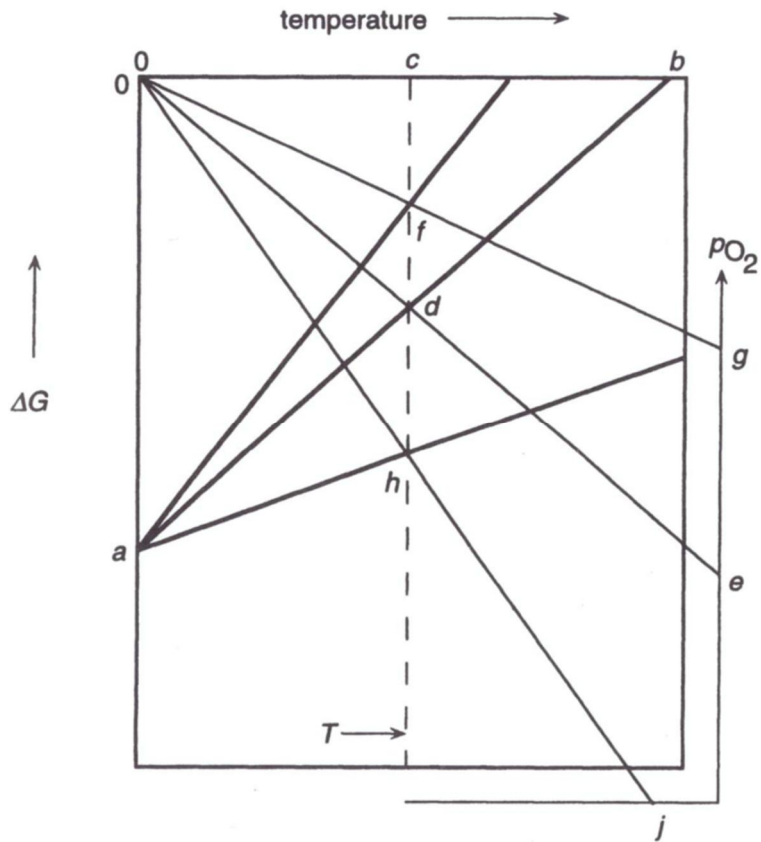


Figure 2.18. Comparison of the Gibbs free energy between Ellingham diagram and phase diagram. Line cd shows the standard Gibbs free energy term in pure element system. When the element M is in solid solution at a_M , the energy term changes to cf . When the compound MO_2 is in solid solution at a_{MO_2} , the energy term changes to ch .^[30]

CHAPTER 3

Experimental Procedures

3.1. Sample preparation by electrospinning

3.1.1. Reductive metal/C nanofibers

For metal/C nanofiber preparation *via* electrospinning (**Chapter 4, 5**), the solution was prepared by mixing metal precursor and polymer matrix. According to the types of metal, different precursor has been used for water solubility. In the case of Co, Ni, Cu, acetate ($\text{Co}(\text{CH}_3\text{COO})_2$, $\text{Ni}(\text{CH}_3\text{COO})_2$, $\text{Cu}(\text{CH}_3\text{COO})_2$) was used. In the case of Fe and Pt, nitrate ($\text{Fe}(\text{NO}_3)_3$) and chloric acid (H_2PtCl_6) was used. The polymer matrix (1.235 g) was dissolved in a distilled water (4.9 g) and ethanol (2.1 g) mixture to a concentration of 15 wt.% and stirred for 2 h at 70 °C. For the optimization of nanofiber morphology after electrospinning, the concentration of polymer matrix was selected as a main parameter for viscosity control (**Figure 3.1**). As the polymer matrix concentration increased, uniform nanofibers were fabricated with hindering the formation of bead.

Chapter 3: Experimental Procedure

The solutions were then mixed and stirred for 10 h to reach the required viscosity for producing a uniform nanofiber. Polyvinyl alcohol (PVA, $M_w = 89,000 \sim 98,000$ g/mol, Sigma-Aldrich) was applied in all cases. The solution was loaded into a syringe with a metal needle tip (18 G). While applying 20 kV from a high voltage source to the metal needle tip, the syringe was pressed by a syringe pump (KDS 100, KD Scientific) at a rate of 0.2 mL/h. The distance between the needle tip and the grounded collector during electrospinning was 12 cm.

3.1.2. Oxidative metal/C nanofibers

Sn/C nanofibers (**Chapter 6**) were fabricated by electrospinning. The solution was composed of tin acetate (SnAc, $M_w = 236.8$ g/mol, Sigma-Aldrich), polyacrylonitrile (PAN, $M_w = 150,000$ g/mol, Sigma-Aldrich) and N,N-dimethylformamide (DMF, Sigma-Aldrich). PAN was selected for fabrication of free-standing nanofiber mat after electrospinning and calcination. First 1.494 g SnAc were dissolved in 5 g DMF, and 0.747 g PAN was dissolved in 5 g DMF. They were stirred on a hot plate during 2 h (120 °C). After dissolution, SnAc solution and PAN solution were mixed and stirred at room temperature. While applying 15 kV from a voltage source to the metal needle tip, the solution-loaded syringe was pressed by a syringe pump (KDS 100, KD Scientific) at a rate of 0.4 ml/h.

3.1.3. Metal compound/C nanofibers

For MoS₂/C nanofiber fabrication (**Chapter 7**), the solution was prepared by mixing ammonium tetrathiomolybdate (ATTM, $M_w = 260.28$ g/mol, Sigma-Aldrich)

Chapter 3: Experimental Procedure

and PAN ($M_w = 150,000$ g/mol, Sigma-Aldrich) into N, N-dimethylformamide (DMF, Sigma-Aldrich). ATTM (1.4 g) was dissolved in DMF (5 g) and stirred for 2 h at 120 °C. PAN (0.7855 g) was dissolved in DMF (5 g) and stirred for 2 h at 120 °C. After dissolution, the solutions were then mixed and stirred for 10 h to reach the required viscosity for producing a uniform nanofiber. The solution was loaded into a syringe with a metal needle tip (18 G). The distance between the tip and the collector was 15 cm. While applying 15 kV from a high voltage source to the metal needle tip, the syringe was pressed by a syringe pump (KDS 100, KD Scientific) at a rate of 0.3 mL/h.

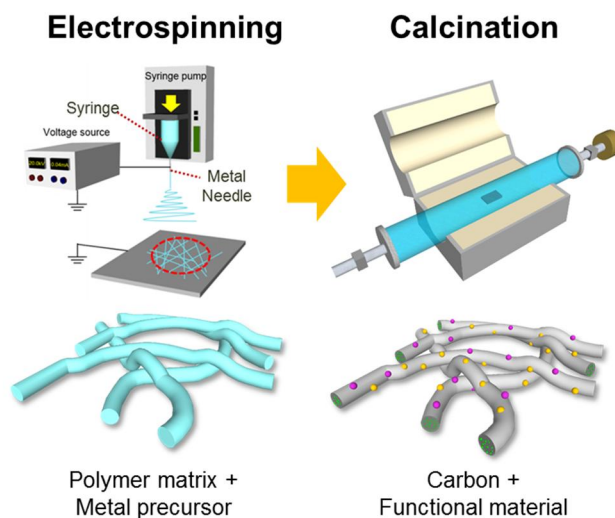


Figure 3.1. Metal (composite)/C Nanofiber fabrication process by electrospinning and calcination

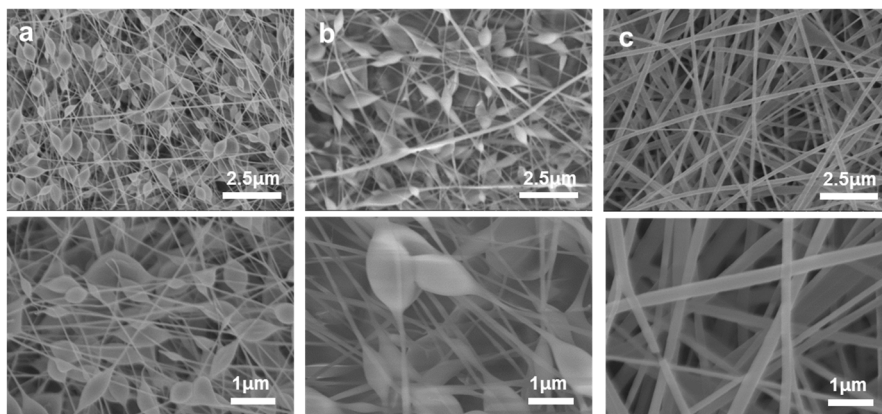


Figure 3.2. Effect of viscosity of electrospinning solution on the nanofiber morphology. **(a)** 10 wt.% PVA with the viscosity of 8.38 poise, **(b)** 13 wt.% PVA with the viscosity of 10.90 poise, **(c)** 15 wt.% PVA with the viscosity of 12.90 poise.

3.2. Calcination

3.2.1. Oxygen partial pressure controlled calcination

The electrospun nanofibers were calcined *via* a CVD furnace at a temperature and ramping rate of 700 °C (metal/C nanofibers), 800 °C (MoS₂/C nanofibers) and 3 °C /min, respectively. In this thesis, a novel methodology for oxygen partial pressure control has been demonstrated. The pO₂ was modulated by adding O₂ gas to a 1.0×10⁵ Torr vacuum. After forming the high vacuum using a rotary pump (RP) and turbo molecular pump (TMP), O₂ gas was allowed to flow at 1~10 sccm using a mass flow controller (MFC). After flowing O₂ for 10 minutes, the gate valve connected to the TMP was closed, and the gas began filling the chamber. Once the chamber pressure reached the specific condition, the gas line valve was closed (**Figure 3.3**). Unlike the O₂ gas flowing method, this method enables to quantitatively control the amount of O₂ in chamber. During calcination, O₂ in chamber is consumed by the reaction between C. This method induces the increase of chamber pressure due to the generation of gaseous C decomposition products such as CO, CO₂ (**Figure 3.4**).

3.2.2. Oxygen empty ambient condition induced calcination

High vacuum (HV) calcination proceeded at a pressure below 10⁻⁵ Torr. Using a rotary pump (RP), a pressure lower than 10⁻² Torr was formed. After that, the HV level (< 10⁻⁵ Torr) was obtained using a TMP. In the Ar calcination, Ar gas was introduced to a chamber at high vacuum. After closing the gate valve (G/V), Ar

Chapter 3: Experimental Procedure

flowed into the chamber at 5 sccm. When the pressure reached 1.5×10^{-1} Torr, the gas line valve was closed. A static Ar condition was prepared without gas flowing into the chamber. The calcination temperature, ramping rate, and time were the same in all conditions as 700 °C, 3 °C/min, and 5 h.

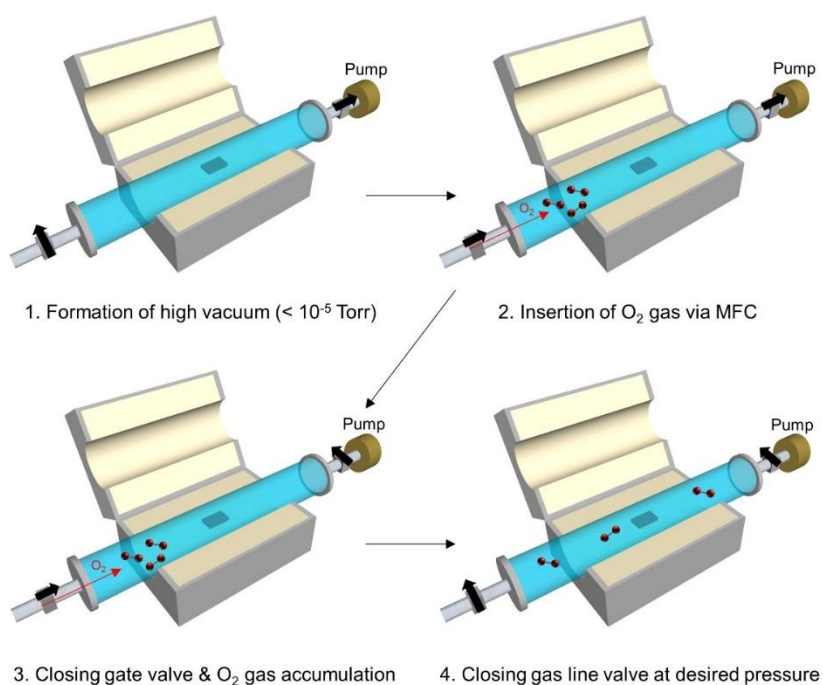


Figure 3.3. Oxygen gas confined calcination scheme for oxygen partial pressure control during calcination.

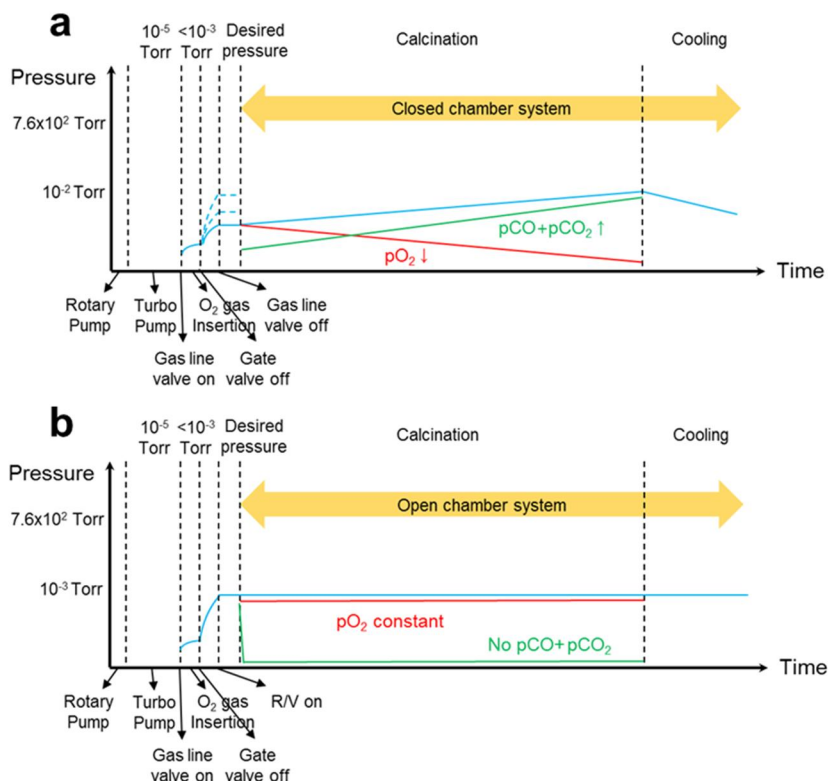


Figure 3.4. Schematic for displaying the difference of degree of pressure change according to the oxygen partial pressure control methodology. In the condition of **(a)** closed chamber system, chamber pressure increases due to the closed valve, accumulation of gaseous decomposition products inside chamber. In the condition of **(b)** open chamber system, chamber pressure maintains constant value due to the gas flowing out behavior by pump.

3.3. Microstructure analysis

The nanofiber microstructure was analyzed using a field emission scanning electron microscope (FE-SEM, S-4800, Hitachi), a high-resolution transmission electron microscope (TEM, Tecnai F20, FEI and JEM-2100F, JEOL), and cs-corrected STEM (cs-STEM, JEM-ARM200F, JEOL) with energy dispersive spectroscopy (EDS, EDAX, Oxford instruments). The samples for TEM were prepared by dispersing nanofiber in ethanol by ultra-sonicating and dispersing onto the Au meshgrid holder (Ted Pella, Inc.).

3.4. Chemical analysis

The metal phase and C decomposition in the nanofiber were analyzed using an X-ray diffractometer (XRD, New D8 Advance, Bruker) with Cu K α 1 radiation ($\lambda = 1.54$ Å) and *via* X-ray photoelectron spectroscopy (XPS, PHI 5000 VersaProbe, Ulvac-PHI). The metal precursor decomposition was analyzed via Fourier transform infrared spectroscopy (FT-IR, Thermo Scientific Nicolet 6700). The structure of MoS₂ and crystallinity of C were analyzed by Raman spectroscopy (T64000, Horiba) with Ar laser (514 nm). The porosity was measured using a BET analyzer with N₂ (purity N5, 99.999%) adsorption/desorption at the temperature of 77 K and the pressure of 0-1 bar (BELSORP-mini, MicrotracBEL).

3.5. Electrical and electrochemical property

3.5.1. Electrical conductivity

The electrical properties of the various metal/C nanofibers were measured *via* the Van der Pauw method to minimize the contact resistance. The morphology and size of nanofiber specimen on the SiO₂ substrate was square with 10×10 mm. Silver paste was placed on the corners of square to minimize the contact resistance between specimen and tip.

3.5.2. All solid state Li-ion battery anode performance

To assemble a test cell, related with electrochemical performance measurement, a 200 mg glass solid state electrolyte (SSE) pellet separator was first pressed at 1 metric ton inside a polyetheretherketone (PEEK) lined Ti test cell die.⁴⁵ The 77.5Li₂S-22.5P₂S₅ glass SSE used as the basis for the all-solid-state construction was prepared via ball milling with an appropriate ratio of Li₂S (99.9%, reagent grade, Sigma-Aldrich) and P₂S₅ (99%, Sigma-Aldrich) using a planetary ball mill (MTI Corporation SFM-1). The electrospun and calcined Sn/C nanofiber cloth was punched into a 10 mm diameter disk. A disk-type electrode composed of the Sn/C nanofiber was then pressed onto one side of the glass electrolyte pellet at 5 metric tons and a Li foil was attached to the opposite side of the pellet at 1 metric ton (**Figure 3.5**). The calculations of the specific energy assume that the Li metal is the counter electrode, and all specific capacities and current densities are given with respect to the total mass of the punched disk of Sn/C nanofibers electrode. The electrochemical performances were tested

Chapter 3: Experimental Procedure

using an Arbin BT2000 battery test station with a constant current density to cycle the cells at 60°C. These electrochemical half-cells were discharged and charged at 50 mA/g (0.05 C) with a voltage range of 0.005 – 1.8 V (vs. Li/Li⁺).

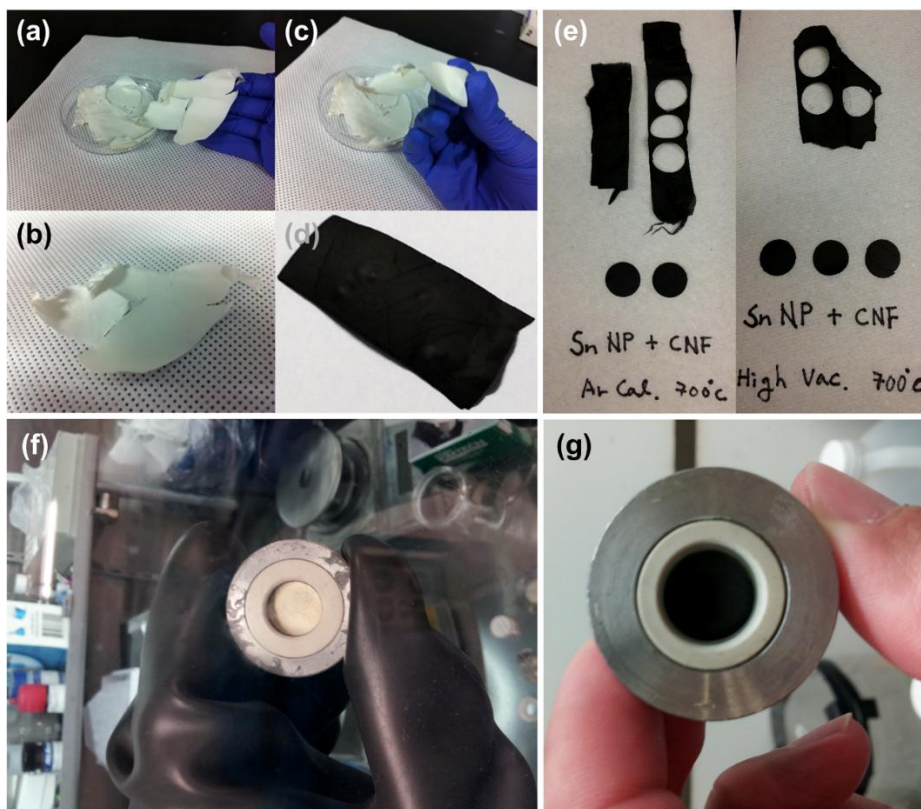


Figure 3.5. Optical images of (a) free-standing electrospun SnAc+PAN nanofiber mats with (b) magnified images and (c) after bending. (d) Free-standing Sn/C nanofiber mats after 700 °C 5h calcination and (e) after punching the mats into a 10 mm diameter disk. (f) Pressed 77.5Li₂S-22.5P₂S₅ solid electrolyte pellet in all-solid-state Li-ion battery testing cell die. (g) Pressed free-standing Sn/C nanofiber mats anode on the solid.

3.6. Computation

3.6.1. FactsageTM calculation

The ternary phase diagrams used to derive the materials composition in the Mo-S-C-O system calculated by a thermochemical database program (FactsageTM software). The database in this calculation was composed of the FACT pure substances database (FactPS) and the FACT light metal database (FTlite). Calculations of the ternary phase diagrams of Mo-S-C, Mo-S-O, Mo-C-O, and MoS₂-C-O were performed with the variable of pressure set to 10⁻⁵, 0.1, 0.2, 0.3, 0.4, 0.76, 4, and 760 Torr at a constant temperature of 800 °C. Furthermore, the solid and gas phase evolution for the 0.075 Mo - 0.302 S - 0.623 C ratio, according to the number of moles of O₂, was calculated with the assumption of infinite calcination time.

3.6.2. Density Functional Theory (DFT) calculation

The DFT calculation using VASP proceeded with the condition of metal fcc (111) and 2×2 surface which contains 4 layers. The functional was GGA-PBE (Perdew-Burke-Ernzerhof). The plane wave basis was set up to 400 eV. The k-point sampling was 3×3×1 Monkhorst-Pack mesh. The forces on each atom was lower than 0.02 eV/Å. Molecules were attached both sides of metal surface to prevent spurious charge transfer. Inversion symmetry and distance constraint were implemented in the original code.

CHAPTER 4

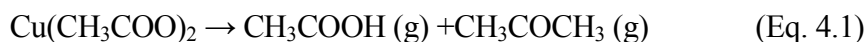
Selective Carbon Oxidation based Reductive Metal/Carbon Nanofiber Structure Control

4.1. Introduction

The objective of this thesis is to identify the effect of thermodynamic consideration during calcination on the structure control of metal/carbon nanofibers. For investigation of *selective oxidation* which induces simultaneous metal reduction and carbon oxidation, Gibbs free energy for oxidation of metal ion and carbon has been studied according to the oxygen partial pressure (pO_2). Selective carbon oxidation generates carbon concentration gradient inside the nanofiber and forms hollow and porous structures with increasing pO_2 . In this study, we report that fully filled carbon nanofibers, metal/carbon core/shell nanofibers, hollow carbon nanofibers, and porous/hollow carbon nanofibers with metal agglomerates can be formed accordingly with the predicted processing parameters. These structures are controlled by kinetic factors as pressure and time of calcination. The mechanism of hollow carbon structure formation and effect of metal species on the carbon oxidation are considered.

4.2. Ambient effect on the thermal decomposition during calcination

To correlate the theoretical thermodynamics and experimental calcination, the component reactions during calcination should be investigated. The atomic species consist of metal and carbon. The effects of calcination on the metal precursor and polymer matrix nanofibers can be separated into C decomposition and metal phase changes. The difference between calcination under air and inert gas (Ar) was considered in the case of CuAc+PVA thermal decomposition using thermogravimetric analysis (TGA) and the TEM images shown in **Figure 4.1**. Complete oxidation in air induces the oxidation based decomposition of CuAc (**Figure 4.1a**). PVA combusts to form CO₂ and H₂O. The final calcination product after calcining the CuAc+PVA nanofiber is CuO nanofibers with no organic components.



However, pyrolysis is the primary C decomposition mechanism during full reduction under Ar. Highly ordered PVA decomposes into low molecular weight hydrocarbons. The final PVA pyrolysis product is residual C. Therefore, the nanofiber weight differs after calcination. Notably, the reducing agent CO forms during the CuAc decomposition during full reduction. Therefore, pure Cu with residual carbon can be obtained.

Chapter 4: Selective Carbon Oxidation based Reductive Metal/Carbon Nanofiber Structure control

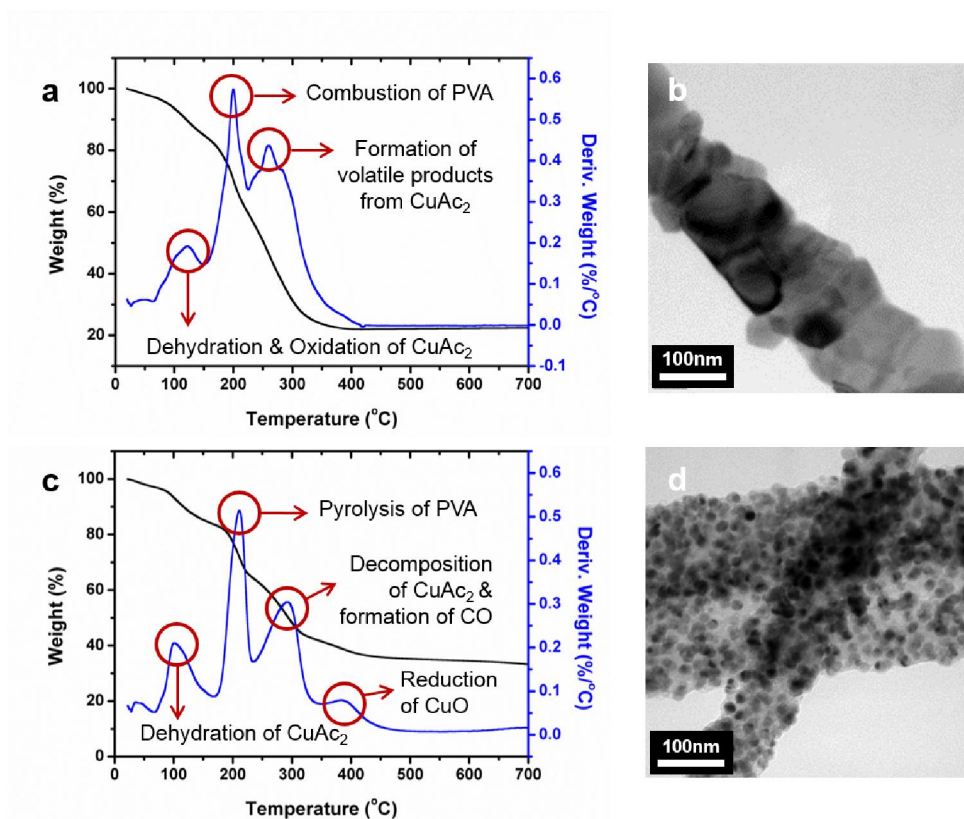
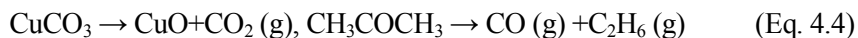


Figure 4.1. Thermogravimetric analysis (TGA) and TEM images of the electrospun CuAc and PVA nanofibers comparing the C decomposition degree of full oxidation and full reduction under **(a, b)** air for combustion and **(c, d)** Ar gas for pyrolysis.

Chapter 4: Selective Carbon Oxidation based Reductive Metal/Carbon Nanofiber Structure control

4.3. Thermodynamics in calcination of Cu/C nanofibers

Based on the consideration about the difference of Gibbs free energy (ΔG) for oxidation between metal and carbon, the nanofiber calcinations can be categorized into full oxidation, selective oxidation, and full reduction based on the pO_2 . It can be realized when C shows the lower ΔG for oxidation than that of metal. We demonstrated the proposed methodology using a copper (Cu)/carbon (C) hybrid nanofiber system in chapter 4. The electrospinning solution used to produce the Cu/C hybrid nanofibers consists of copper acetate as the metal precursor and polyvinyl alcohol (PVA) as the polymer matrix. At a given temperature, C oxidizes at a lower pO_2 than Cu because the Gibbs free energy of oxidation ($\Delta G_{\text{oxidation}}$) for Cu is higher than that for C.^[22] By controlling the pO_2 during calcination, 3 different redox reaction schemes can be obtained, as shown in **Figure 4.2**.

First, calcining with a high pO_2 oxidizes both Cu and C. PVA combusts into CO_2 and H_2O , and CuAc decomposes into CuO (full oxidation in **Figure 4.2a**, top).^[23,24] A following calcination under H_2 for reduction is required to obtain pure Cu. Cu nanofibers are generally formed *via* two step calcinations.^[6,25] However, the Cu nanofiber is damaged during the sequential oxidation and reduction steps. Also, an additional protection layer is required for Cu nanofiber application.

Second, under low pO_2 , both Cu and C are reduced. The PVA decomposes into low molecular weight hydrocarbons and forms residual C *via* pyrolysis.^[26] Cu and carbon monoxide (CO) form during the decomposition of CuAc (full reduction in **Figure 4.2a**, bottom).^[27,28] Therefore, the final structure is a composite of pure Cu nanoparticles embedded in a C nanofiber.^[29,30] However, there is no PVA combustion,

Chapter 4: Selective Carbon Oxidation based Reductive Metal/Carbon Nanofiber Structure control

and too much residual C remains, which retards the electrical conductivity of the nanofiber.

Third, calcination can occur in the pO_2 range between full oxidation and full reduction. Because the pO_2 required to oxidize Cu is higher than that required for C, a pO_2 in this range oxidizes C but reduces Cu (selective oxidation in **Figure 4.2a**, middle). It is important that the oxidation product of C is mainly gaseous products. As the degree of C oxidation increases, the amount of C in nanofibers is reduced. PVA decomposition yields limited residual C, while pure Cu is obtained in the nanofiber. More interestingly, the nanofiber structure can be controlled; various structures, including fully filled C nanofibers, Cu/C core/shell nanofibers, hollow C nanofibers, and porous/hollow C nanofibers can be formed by controlling the pressure and time (**Figure 4.2b**).

In these procedures, calcination proceeded at 700 °C for 1 ~ 10 h. The pO_2 was modulated by pumping the chamber to a high vacuum level ($< 1.0 \times 10^{-5}$ Torr) and filling with the desired O_2 pressure. The chamber was then closed, and the calcination proceeded. **Figure 4.3a** shows the X-ray diffractometer (XRD) analysis of the nanofiber after calcining under various pressures. It is important that processing parameters for inducing selective oxidation can be confirmed by the reduction of metal phase and change of C decomposition degree according to the pO_2 . In air (7.6×10^2 Torr), a CuO phase formed, indicating that the CuAc decomposed into a Cu oxide. Pure Cu formed at pressures from 1.0×10^{-5} Torr to 1.0×10^{-1} Torr. **Figure 4.3b** shows the weight percent (wt.%) of the Cu and C at the nanofiber surface based on X-ray photoelectron spectroscopy (XPS) analysis. Going from 1.0×10^{-5} Torr to 1.0×10^{-1} Torr decreased the C wt.% to 56 wt.%, suggesting that the PVA decomposed into gaseous components such as CO and CO_2 (combustion). At lower pressures, the C

Chapter 4: Selective Carbon Oxidation based Reductive Metal/Carbon Nanofiber Structure control

content change was small, demonstrating that the PVA decomposed into lower molecular weight C chains (pyrolysis). Therefore, the pressure range that formed pure Cu and caused the abrupt C content change was expected to provide selective oxidation.

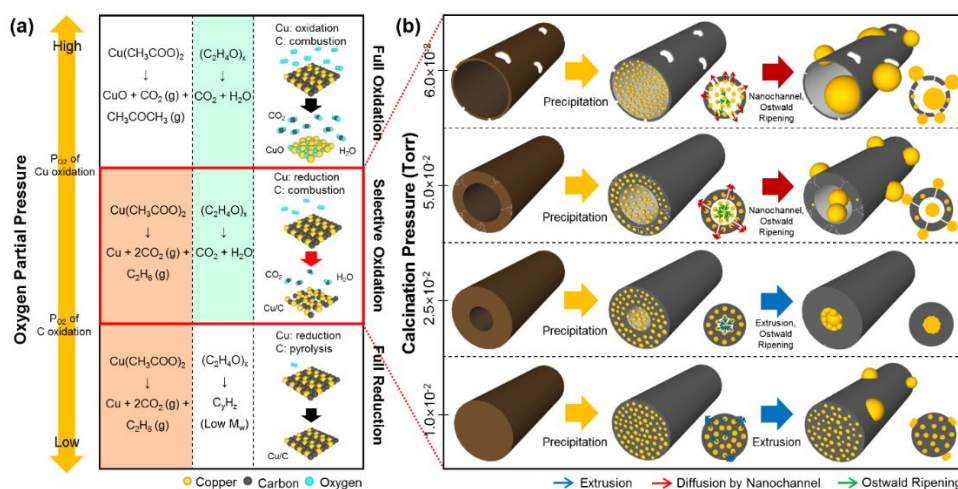


Figure 4.2. (a) Redox reaction schemes according to the effect of $p\text{O}_2$ during calcination on the electrospun CuAc+PVA nanofibers. (b) Schematic indicating the Cu/C nanofiber formation mechanism for the fully filled, core/shell, hollow, and porous/hollow nanofibers by selective oxidation. According to the structures of the C nanofiber, the inward or outward Cu diffusion related to the CTE differences between Cu and C is determined.

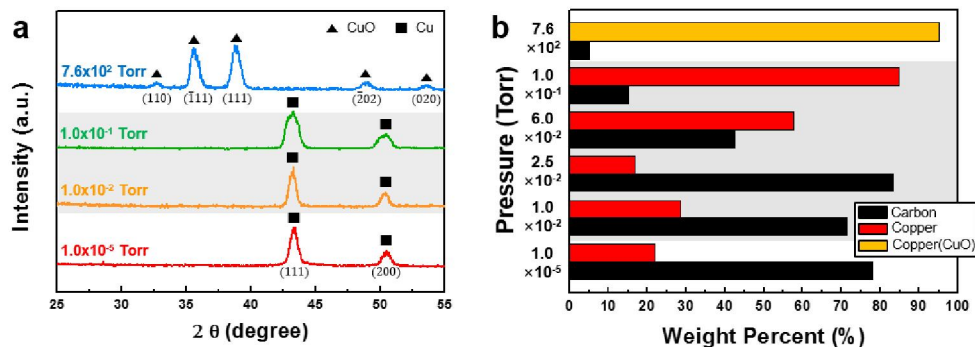


Figure 4.3. (a) Phase transformation for Cu relative to the calcination pressure as determined by XRD. (b) Quantitative XPS analysis of C decomposition in the Cu/C nanofibers. These analyses indicate that the pressure range from 1.0×10^{-2} to 1.0×10^{-1} Torr provides selective oxidation.

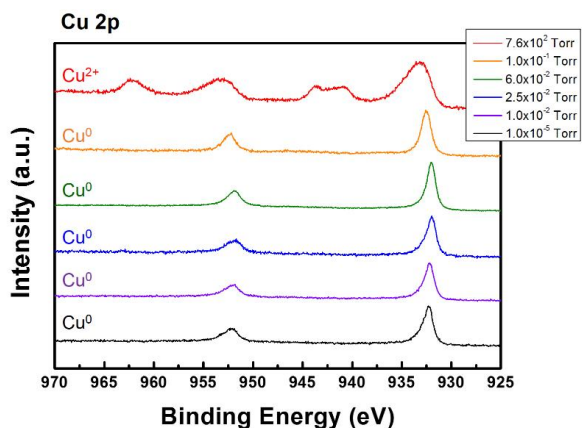


Figure 4.4. Comparison of the Cu 2p XPS spectra to investigate the existence of Cu phase in the nanofiber after calcination. With the exception of 7.6×10^2 Torr, a pure Cu phase was observed across the calcination range from 1.0×10^{-5} Torr to 1.0×10^{-1} Torr.

4.4. Microstructural changes of Cu/C nanofibers by selective oxidation

We studied the pressure range from 1.0 to 6.0×10^{-2} Torr for selective oxidation behavior. **Figure 4.5** shows field emission scanning electron microscopy (FE-SEM) and transmission electron microscopy (TEM) images for the nanofiber structures after 5 h of calcination. Interestingly, various Cu/C nanofiber structures formed according to the pressure, including fully filled C nanofibers, Cu/C core/shell nanofibers, hollow C nanofibers, and porous/hollow C nanofibers. First, at 1.0×10^{-2} Torr (**Figure 4.5a**), fully filled C nanofibers with embedded Cu nanoparticles were observed. Sparsely distributed Cu agglomerates also formed outside the nanofiber. Increasing the pressure to 2.5×10^{-2} Torr (**Figure 4.5b**) formed Cu/C core/shell nanofibers. The C formed a hollow structure and the Cu atoms located only in the C nanofiber core. No Cu agglomerates were observed outside the nanofiber. The diameter increased from 150 nm to 300 nm, and the C nanofiber surface was quite smooth. With a pressure of 5.0×10^{-2} Torr (**Figure 4.5c**), the C nanofiber structure was hollow, similar to **Figure 4.5b**, but the inner diameter increased. Cu agglomerates formed both inside and outside the hollow nanofiber. The additional difference relative to **Figure 4.5a** was the lack of embedded Cu nanoparticles in the C nanofiber. At 6.0×10^{-2} Torr (**Figure 4.5d**), damaged C nanofibers were observed. The inner diameter was further increased, decreasing the C nanofiber shell thickness. Relatively large Cu agglomerates (~ 100 nm) were observed both inside and outside the porous/hollow nanofiber.

The above results showed that various C nanofibers could be formed by simply controlling pO_2 ; the Cu atom distribution changed accordingly. A Cu/C core/shell structure formed at 2.5×10^{-2} Torr. To understand the Cu/C nanofiber structural

Chapter 4: Selective Carbon Oxidation based Reductive Metal/Carbon Nanofiber Structure control

evolution during calcination, the isothermal times at 700 °C were changed to 1 h, 3 h, 5 h, and 10 h with a fixed pO_2 of 2.5×10^{-2} Torr. After 1 h (**Figure 4.6a**), C nanofibers without hollow cores were observed. The nanofiber surface was not as smooth as that after 3 or 5 h. The Cu atoms agglomerated outside the nanofiber. After 3 h (**Figure 4.6b**), Cu/C core/shell structures started to form. The nanofiber surface was smooth, indicating that defects on the nanofiber surface were recovered by outward C diffusion. Cu was located in the C core and outside the nanofiber. The number of outer Cu agglomerates decreased as the core/shell structure developed. The structural evolution completely formed a Cu/C core/shell nanofiber after 5 h (**Figure 4.6c**). As the inner diameter of hollow nanofiber increased due to outward C diffusion during the 5 h calcination, more Cu diffused inward compared with that at 3 h. No outside Cu agglomerates were observed for this time point. Finally, after a 10 h calcination (**Figure 4.6d**), a porous/hollow C nanofiber formed. Cu agglomerates formed both inside and outside this nanofiber by Cu diffusion. This structure is similar to the one formed by calcination at 6.0×10^{-2} Torr (**Figure 4.5d**).

The formation of various Cu/C nanofibers is possible using C decomposition and diffusion of Cu and C based on the thermodynamic and kinetic driving forces during calcination. These results can be reproduced by modulating the calcination pressure and time. A structure map showing the evolution with pressure and time was constructed and is shown in **Figure 4.7**. The nanofiber structures range from the fully filled C nanofiber to the porous/hollow C nanofiber and are categorized into colors. The hollow C structure tended to form with increasing pressure and time. As the pressure increased, the hollow C structure formation rate increased. For example, the time to form similar structures was 10 h, 3 h, and 1 h for 1.0 , 2.5 , and 5.0×10^{-2} Torr, respectively. At 6.0×10^{-2} Torr after 10 h, the nanofiber structures were fully

Chapter 4: Selective Carbon Oxidation based Reductive Metal/Carbon Nanofiber Structure control

decomposed, and only Cu agglomerates remained. Therefore, the structural evolution from fully filled C nanofiber to porous/hollow C nanofiber was affected by the degree of C decomposition. The pressure controlled the rate of C decomposition, and the Cu/C nanofiber formation was controlled by kinetic factors (**Figure 4.8**). Furthermore, it can be determined that temperature, pressure, and time affect the process of hollow C nanofiber formation. With increasing degree of C decomposition, inner diameter of hollow C increases. This phenomenon can be induced by pressure and time control during calcination. As the pressure increases, the rate of hollow structure formation increases. As the temperature increases, the pressure region for selective oxidation increases in Ellingham diagram. These directly indicate that this process is under the control of kinetic principle.

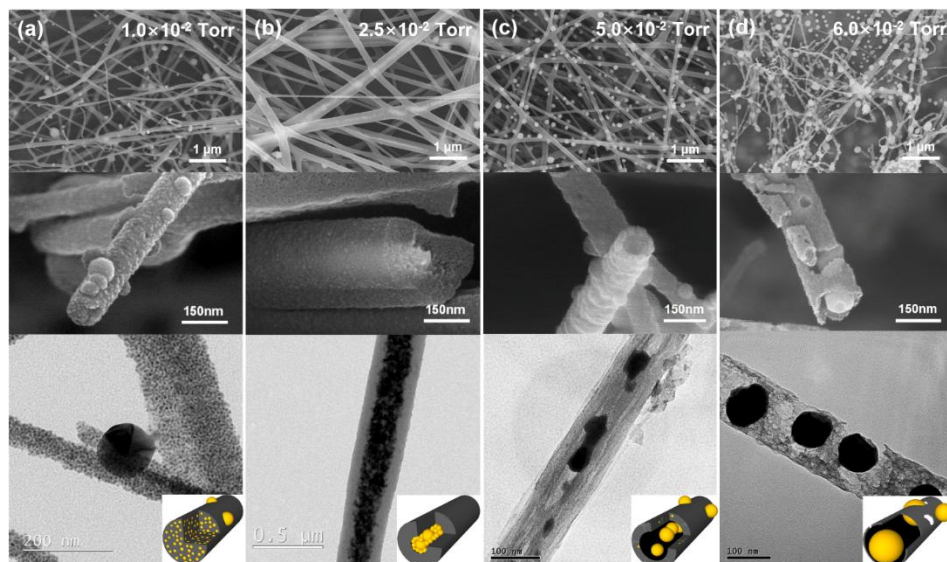


Figure 4.5. FE-SEM and TEM images of the Cu/C nanofibers formed via selective oxidation at 700 °C with a 5 h calcination at **(a)** 1.0×10^{-2} Torr, **(b)** 2.5×10^{-2} Torr, **(c)** 5.0×10^{-2} Torr, and **(d)** 6.0×10^{-2} Torr. Increasing the pressure decreases the C shell thickness of the Cu/C nanofiber. According to the pressure, various Cu/C structures are formed, including fully filled C nanofibers, Cu/C core/shell nanofibers, hollow C nanofibers, and porous/hollow C nanofibers.

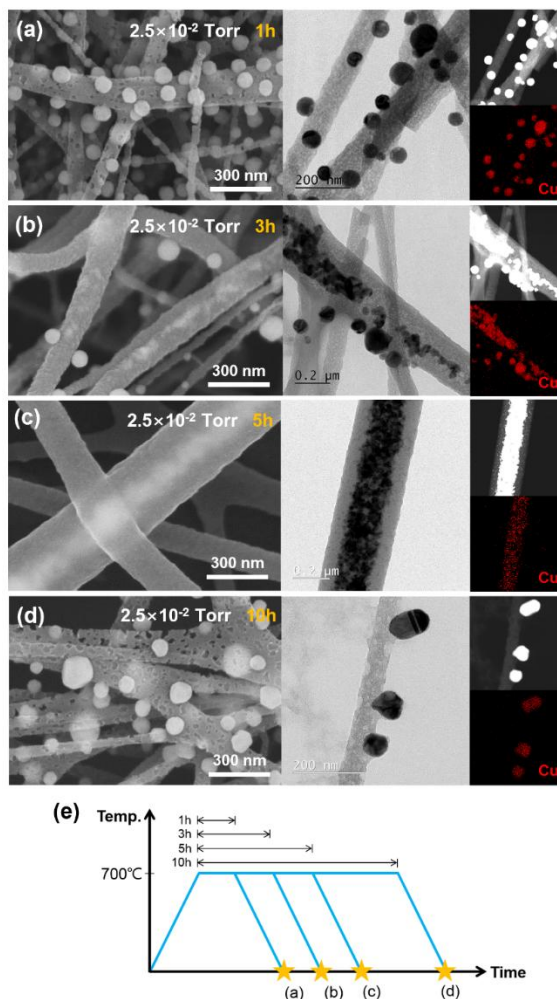


Figure 4.6. The Cu/C nanofiber structural transformation *via* FE-SEM and TEM images with HAADF and EDS for the 700 °C calcination at 2.5×10^{-2} Torr over **(a)** 1 h, **(b)** 3 h, **(c)** 5 h, and **(d)** 10 h with the **(e)** calcination profile. The calcination time effects revealed the growth of the inner diameter of the hollow C nanofiber, which induced inward/outward Cu diffusion based on the C decomposition amount.

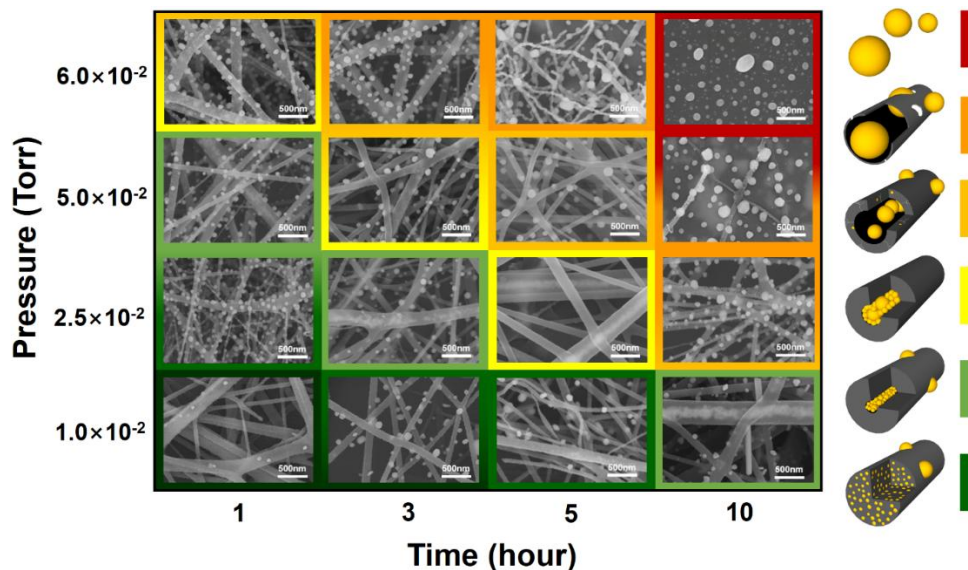


Figure 4.7. Structural transformation map of the Cu/C nanofibers simultaneously considering the calcination pressures from 1.0×10^{-2} Torr to 6.0×10^{-2} Torr and times from 1 h to 10 h using FE-SEM. The nanofibers are categorized by colors according to their degree of hollow C structure and Cu dispersion. The hollow structure formation rate increased with increasing pressure.

Chapter 4: Selective Carbon Oxidation based Reductive Metal/Carbon Nanofiber Structure control

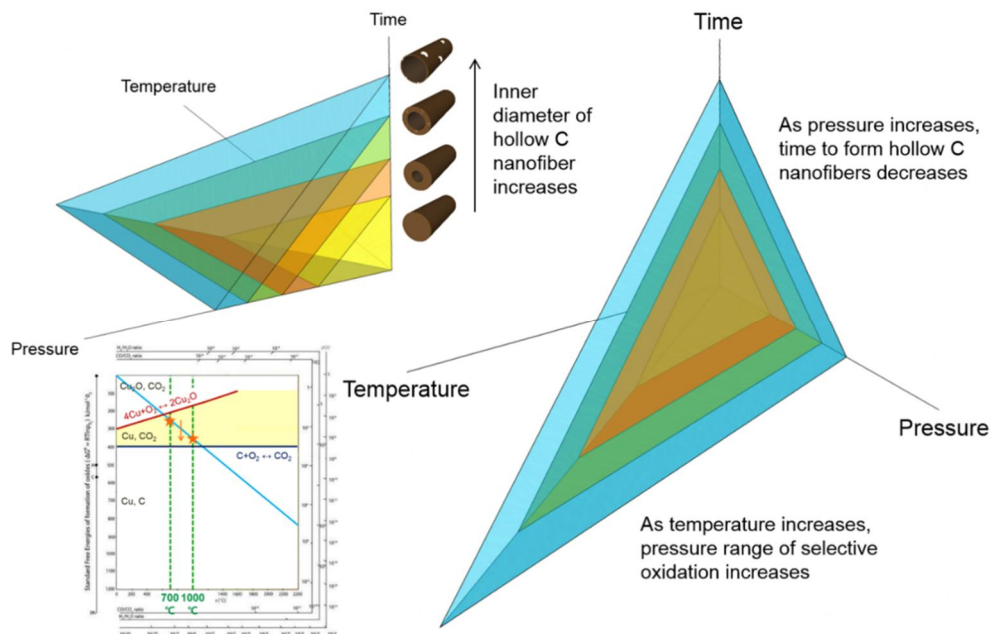


Figure 4.8. Effect of processing parameters in the aspects of temperature, pressure, and time on the process of hollow C nanofiber formation. With increasing degree of C decomposition, inner diameter of hollow C increases. It can be simultaneously induced by pressure and time control during calcination. As the temperature increases, the pressure region for selective oxidation increases.

4.5. Mechanism of Cu/C Nanofiber Formation

The mechanism of formation of the various Cu/C nanofibers during the selective oxidation process is schematically explained in **Figure 4.9**. In selective oxidation, CuAc decomposes into Cu and gaseous CO₂, which remain as voids in the nanofiber. To precisely investigate the CuAc decomposition, Fourier transform infrared spectroscopy (FT-IR) proceeded according to the temperature of ramping region during calcination in **Figure 4.9a**. They cover from the electrospun state to the calcination at 200 °C, 500 °C, and 700 °C of 2.5×10⁻²Torr. Existence of CuAc with specific chemical bonding is interpreted by the change of adsorptive peaks. CuAc shows 1760~1665 peak of C=O stretch and 1470~1450 peak of C-H bend.^[38] Until 200 °C of ramping temperature, peaks are similar with the electrospun nanofibers which contain CuAc. However, as temperature increases over 500 °C, broad peak at 3500~3200 cm⁻¹ which indicates the dehydration of CuAc disappears. Also, the peaks for C=O stretch and C-H bend which indicate the existence of CuAc disappear. It can be determined that the decomposition of CuAc starts over 200 °C and finishes before reaching at 500 °C.

The existence of CO₂ inside the nanofiber and the density difference between CuAc (1.88 g/cm³) and Cu (solid: 8.96 g/cm³, liquid: 8.02 g/cm³) induce the void formation. PVA decomposes into gaseous components by C oxidation. The formation of a hollow C nanofiber structure is related with the gaseous product formation by selective C oxidation. C concentration gradient exists between inner and outer part of nanofibers (**Figure 4.9b**). It is due to the higher degree of C oxidation at the outer part than the inner part of nanofibers. It means that the concentration of gaseous products of C oxide such as CO (g) and CO₂ (g) is higher at the outer part. The accumulation of

Chapter 4: Selective Carbon Oxidation based Reductive Metal/Carbon Nanofiber Structure control

pores at the core nanofiber forms hollow C structures. As more C decomposes, the inner diameter of the hollow nanofiber increases with a constant nanofiber diameter. Interestingly, the electrospun PVA nanofibers without CuAc cannot form hollow or core/shell structures, suggesting that the metal precursor is important for hollow structure formation (**Figure 4.10**). It is a key principle to understand the mechanism of metal/C structure formation by selective oxidation and it will be considered in next chapter.

As shown in **Figure 4.9c**, the fully filled C nanofiber was formed at 1.0×10^{-2} Torr because of the minimal C decomposition. Cu precipitation made densely embedded Cu nanoparticles within the C nanofiber. A large Cu agglomerate outside the nanofiber can be formed during cooling because of the difference in thermal expansion coefficients (CTE) for Cu ($16.5 \times 10^{-6} / ^\circ\text{C}$) and C ($1.5 \times 10^{-6} / ^\circ\text{C}$).^[39,40] A stress field was generated in the Cu embedded C nanofiber because Cu tends to shrink more than C. The outward Cu diffusion as a form of extrusion can be induced to relax such stress.^[21]

$$J = D(c\nabla V/kT) \quad (\text{Eq. 4.6})$$

where k denotes Boltzmann constant; T , the temperature; D , the diffusivity; c , the concentration; and ∇V , the potential gradient. Cu diffuses for the relaxation of ΔCTE based stress. At 2.5×10^{-2} Torr, the hollow structure began to be formed by C combustion and the related Kirkendall effect. Outward C diffusion smoothed the nanofiber surface and the Cu was located in the inner hollow of the C nanofiber. The agglomerate size was increased *via* Ostwald ripening. Increasing the pressure (5.0×10^{-2} Torr) further increased the inner diameter of the hollow C nanofiber and the Cu

Chapter 4: Selective Carbon Oxidation based Reductive Metal/Carbon Nanofiber Structure control

agglomerate size. Nanochannels were formed in the hollow C nanofiber at higher pressures, and the Cu diffusion during cooling was accelerated. Therefore, sphere-shaped Cu agglomerates were formed both inside and outside the nanofiber to reduce the surface energy. At 6.0×10^{-2} Torr, the nanochannel broadened to form a porous/hollow C nanofiber, which accelerated the outward diffusion of Cu and formed enlarged Cu agglomerates. This formation mechanism of various Cu/C nanofibers can be applied to not only pressure but also time as a kinetic factor. At a given pressure of same pO_2 , time determines the degree of C decomposition and hollow C nanofiber formation. According to the C nanofiber structures, the Cu diffusion mechanism is similar with the case of pressure. It should be noted that pressure determines the formation rate of hollow C structure because the amount of O_2 which reacts with C at the surface of nanofiber increases at high pressure. Formation mechanism of Cu/C nanofibers can be explained by Kirkendall effect-based hollow C structure formation and stress relaxation-based Cu diffusion with Ostwald ripening. The uniqueness of our method is that both atomic diffusions and alignments are effectively controlled by only the kinetic factors, whereas previous studies required complicated additional post treatment.^[13,22]

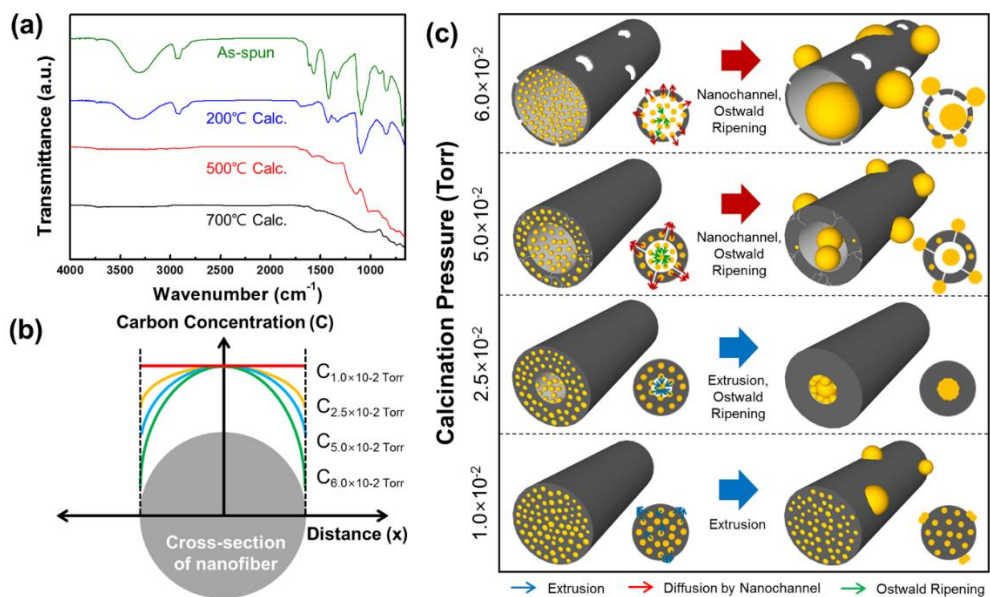


Figure 4.9. (a) FT-IR spectra for investigating the CuAc decomposition during the calcination of electrospun CuAc+PVA nanofibers based on the ramping region temperature. Schemes indicating for the (b) C concentration gradient as a driving force of outward C diffusion and (c) Cu/C nanofiber formation mechanism of the fully filled, core/shell, hollow, and porous/hollow nanofibers by selective oxidation.

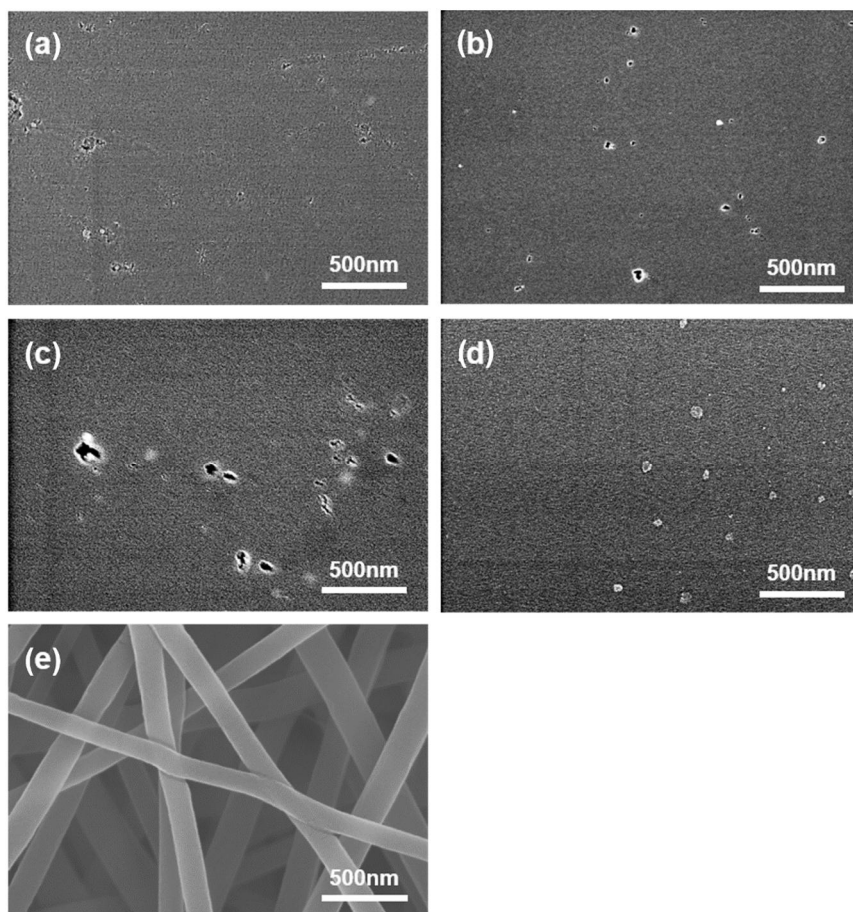


Figure 4.10. Structures of PVA nanofibers after calcining at **(a)** 1.0×10^{-5} Torr for full reduction and **(b)** 1.0×10^{-2} Torr, **(c)** 5.0×10^{-2} Torr, and **(d)** 1.0×10^{-1} Torr for selective oxidation. Calcining at 1.0×10^{-1} Torr decomposed all of the material with only the substrate remaining. **(e)** Before the calcination, uniform PVA nanofibers were formed.

4.6. Effect of Cu/C nanofiber structures on electrical properties

The structure of the Cu/C nanofiber affects its electrical properties. **Figure 4.11a** and **b** show the current-voltage (I-V) relationships and sheet resistances (R_s) of the nanofibers formed after 5 h calcination in which the samples showed good ohmic conduction. Increasing the pressure from 1.0 to 2.5×10^{-2} Torr decreased the resistance. The resistance then increased upon increasing the pressure above 2.5×10^{-2} Torr. Finally, at 6.0×10^{-2} Torr, the ohmic character disappeared. Core/shell nanofibers with Cu agglomerates densely located in the core had a minimum R_s of 251 Ω/sq (**Figure 4.11c**). In this structure, the outer C protective shell had a disordered structure. The imperfect crystalline C structure of PVA can hinder O_2 diffusion through the outer C. It can help prevent Cu oxidation. Without any additional process to coat Cu nanofiber, the self-formed Cu/C core/shell nanofiber exhibited stable electrical properties in atmospheric. The increase of R_s limited to within 10% during 28 days, as shown in **Figure 4.11d**. Calcination at 5.0×10^{-2} Torr, which forms hollow C nanofibers, yielded larger R_s values. The porous/hollow C nanofibers with enlarged Cu agglomerates formed at 6.0×10^{-2} Torr exhibited the highest electrical resistivity. These results indicate that selective oxidation can induce various Cu/C nanofiber properties *via* the different Cu dispersion and C nanofiber structures.

Interestingly, the structures of Cu/C nanofibers affected the behavior of mechanical stress induced electrical reliability. To investigate the mechanical reliability, Cu/C nanofibers sheets attached on the polyimide (PI) film and bending fatigue test proceeded. The strain in bending fatigue test can be modulated by the curvature of bended region and it is directly affected by the gap ($2r$) between fixed and moving plate with a fixed thickness of Cu/C nanofibers and PI film (h). According to the

Chapter 4: Selective Carbon Oxidation based Reductive Metal/Carbon Nanofiber Structure control

relative displacement of conducting film, the deformation mode of tensile and compressive can be determined.

$$\varepsilon = \frac{\Delta l}{l_0} = \frac{\pi r - \pi r_0}{\pi r_0} = \frac{h}{2r_0} \quad (\text{Eq. 4.7})$$

The structures of Cu/C nanofibers for reliability evaluation are categorized into Cu embedded inside C nanofibers and Cu agglomerated outside C nanofibers. There exists an intimate relationship between the distribution of Cu and mechanical stress induced electrical reliability (**Figure 4.12**). Generally, as the cycle proceeds, the resistance increases due to the mechanical stress induced nanofiber destruction. In the case of Cu embedded C nanofibers, R/R_0 increases toward 1.3 and starts to be saturated over 200,000 cycles at 1% compressive condition. Interestingly, as the strain increases from 1% to 2% condition, the resistance increase was lower than 2% and R/R_0 maintained at the initial value during 500,000 cycles (**Figure 4.12a**). It is an unexpected behavior and outstanding reliability performance. In contrast, Cu agglomerated outside C nanofibers show gradual increase of R/R_0 as the bending fatigue cycle proceeds (**Figure 4.12c**). To study about this phenomena, the microstructures of Cu/C nanofibers have been investigated by FE-SEM. In the case of Cu embedded inside C nanofibers (2% strain) which showed R/R_0 increase lower than 2%, broken nanofibers were linked by Cu extrusion (**Figure 4.12b**). For the relaxation of mechanical stress induced by bending fatigue, Cu diffused to the broken tip of nanofibers and reliability has been enhanced by this linking behavior. However, in the case of Cu agglomerated outside C nanofibers, there was no linking phenomenon between the broken C nanofibers due to the outside displacement of Cu agglomerates (**Figure 4.12d**).

Chapter 4: Selective Carbon Oxidation based Reductive Metal/Carbon Nanofiber Structure control

This mechanical stress induced Cu diffusion can link the number of nanofibers from 2 to 5 (**Figure 4.13a**). In TEM images of linked part of nanofibers, continuous crystalline metal structures were observed and it means that recrystallization can occur after repeated mechanical deformation. The structures of Cu in Cu/C nanofibers affects not only intrinsic electrical conductivity but also electrical reliability after mechanical deformation.

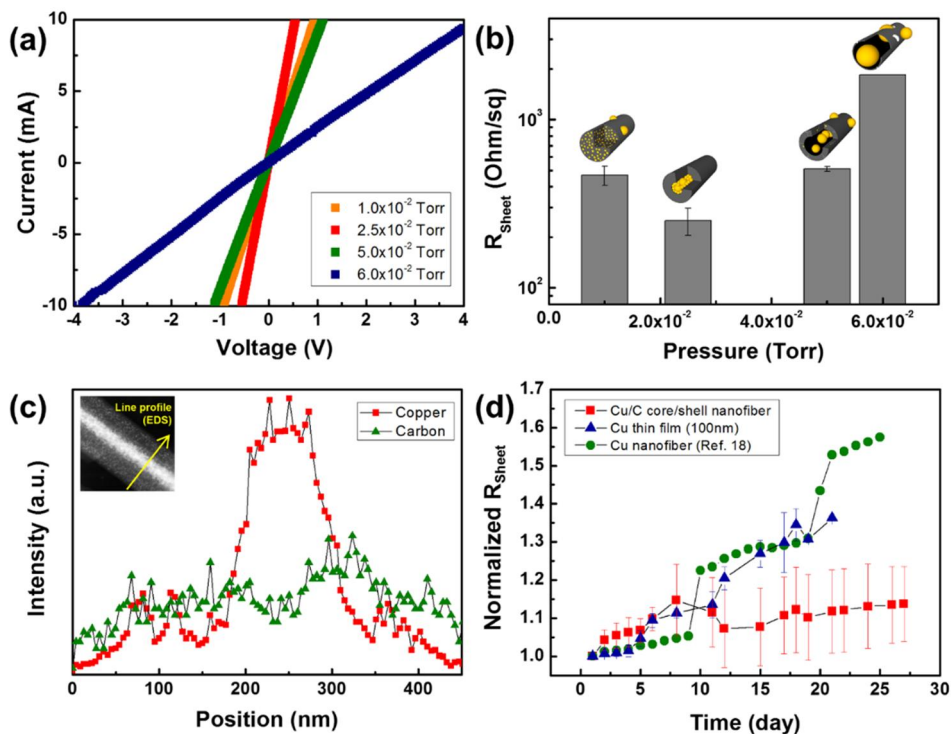


Figure 4.11. (a) I-V curve for the Cu/C nanofibers formed *via* selective oxidation according to pressure and the (b) sheet resistance (R_s) determined *via* the Van der Pauw method. (c) TEM EDS line profile for the dual Cu and C components of the Cu/C core/shell nanofibers. (d) High oxidation resistance of the Cu/C core/shell nanofibers formed at 2.5×10^{-2} Torr. R_s was measured under atmospheric conditions.

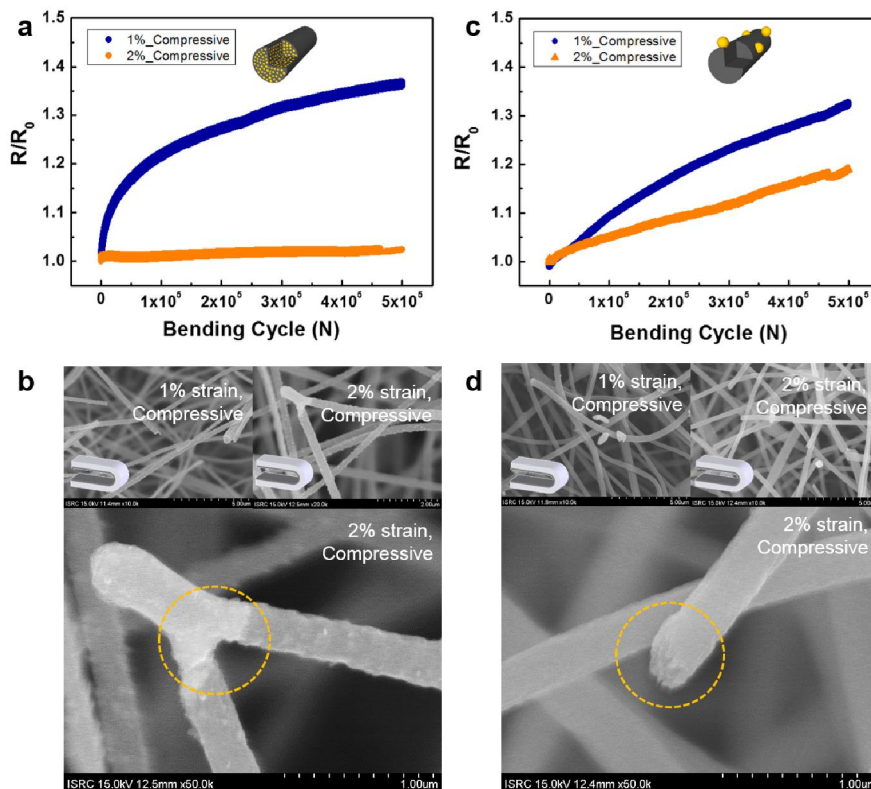


Figure 4.12. Effect of Cu structures (particle size and distribution) on the mechanical-electrical reliability, which has been analyzed by the bending fatigue test during 500,000 cycles. **(a)** Relative resistance change with increasing bending cycles and **(b)** FE-SEM images after 500,000 cycles of Cu embedded inside C nanofibers according to the compressive strain. **(c)** Relative resistance change with increasing bending cycles and **(d)** FE-SEM images after 500,000 cycles of Cu agglomerated outside C nanofibers according to the compressive strain.

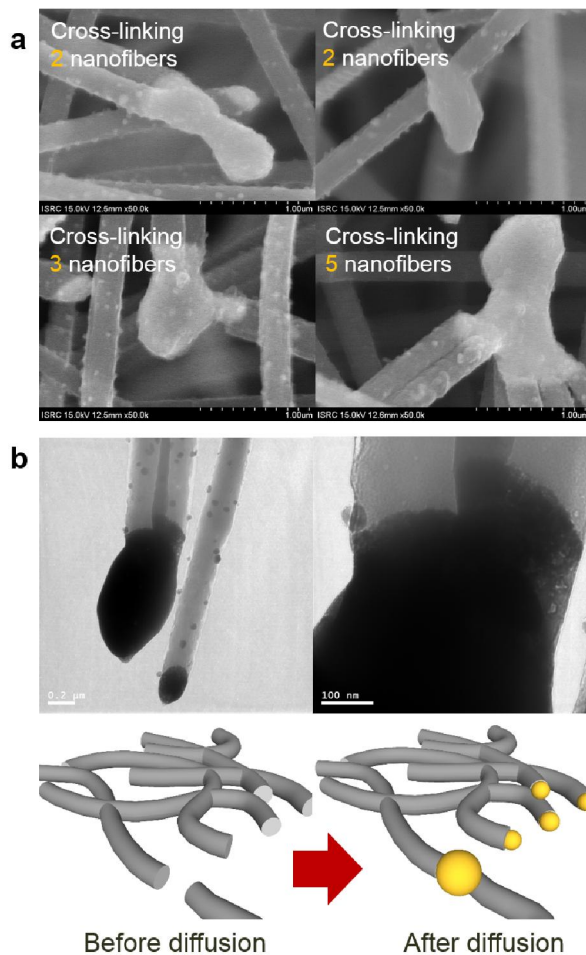


Figure 4.13. (a) FE-SEM and (b) TEM images for displaying the cross-linked broken nanofibers by diffused Cu after 500,000 bending fatigue cycles of Cu embedded C nanofibers in 2% strain condition.

4.7. Summary

We demonstrated a new fabrication methodology for diversely structured metal/C nanofibers by controlling the redox reaction with kinetic factors, such as calcination pressure and time. The structures were classified into fully filled C nanofibers, metal/C core/shell nanofibers, hollow C nanofibers, and porous/hollow C nanofibers. All of these structures originated from the same raw materials and formed *via* a one-step process. The proposed method was based on selective oxidation, which induces C oxidation and metal reduction during calcination. In this scheme, the oxidation tendency of the metal is lower than that of C. In the pressure range of selective oxidation from 1.0 to 6.0×10^{-2} Torr, the degree of C decomposition in the nanofiber can be adjusted. Therefore, the inner diameter of the hollow structure and metal particle size and distributions were controlled by the kinetic factors of calcination, such as pressure and time. Also, the rate of hollow structure formation was affected by the pO_2 . The self-forming mechanism of the metal/C nanofibers can be explained through the hollow C structure formation and stress relaxation-based metal diffusion. As C decomposed in the selective oxidation, concentration gradients were generated and induced outward C diffusion. According to the states of C structures, the degree and direction of Cu diffusion for the relaxation of stress were determined. These metal/C nanofibers showed various properties according to the secondary nanostructures. Especially, self-formed Cu/C core/shell nanofibers at 2.5×10^{-2} Torr efficiently prevented Cu oxidation. Through this fabrication method, the morphology and distribution of 1D nanostructures can be optimized for inducing high performance in various applications.

CHAPTER 5

Selective Carbon Oxidation induced Hollow Structure Formation in Metal/Carbon Nanofibers

5.1. Introduction

The objective of this thesis is to identify the effect of catalytic C oxidation on metallic species to form hollow C structures which determines the metal/carbon nanofiber structures. The fundamental principles to control the structure and phase of metal/C nanofibers were studied in Chapter 4. Here, we established a methodology to provide core principles to understand the effect of controlling the phase, morphology, size, arrangement, and distribution of nanomaterials. Generally, among the various catalytic roles of metal on C related reactions, carburization on metal surface received great attention due to the formation of graphene. This kind of promoted carburization and related graphene synthesis were mainly investigated with the Cu due to its low miscibility (activity coefficient $\gamma > 1$) with C. The representative reverse reaction of the carburization is the promoted C decomposition (especially oxidation based combustion) at the metal surface. After first observation of promoted carbon monoxide (CO) oxidation by Langmuir, catalytic oxidation of gaseous C composites

Chapter 5: Selective Carbon Oxidation induced Hollow Structure Formation in Metal/Carbon Nanofibers

was investigated theoretically in Pt, Pd thin films. In this work, it has been revealed how catalytic C oxidation with the existence of metal can induce the formation of hollow, porous structures with remarkable precision. Reductive metals such as Fe, Co, Ni, Cu, and Pt were applied to study about the mechanism of catalytic C oxidation and related effect on formation of hollow C structure. This innovative conversion of metal role can open a new paradigm of synthesis methodology for metal ion embedded multi-atomic component nanomaterials.

5.2. Thermodynamic consideration on the calcination of reductive metal/carbon nanofibers

For the phase transformation of metal ion and carburization of polymer matrix, calcination after electrospinning is required. **Figure 5.1a** shows the schematics for gas-solid reactions between O₂ gas and metal/C nanofibers during calcination. In the multi-atomic component material, the oxidation and reduction aspects of metal ion in metal precursor and C can be categorized into 3 groups according to the standard formation Gibbs free energy of compound (ΔG°) in **Figure 5.1b**. Among various metal species, noble metal and transition metal show lower oxidation tendency than that of C. This principle provides a theoretical background for distinguishing full reduction, full oxidation, and selective oxidation. Full reduction under lower pO₂ than ΔG° of oxidation induces simultaneous reduction of metal and C. Full oxidation which proceeds at the higher condition of ΔG° of oxidation induces simultaneous oxidation of metal and C. If the pO₂ condition can be modulated between the metal and C, selective metal reduction and C oxidation can be induced. This calcination scheme is a key principle to control metal/C hybrid nanofibers. **Figure 5.1c** is the schematic for indicating the structure evolution of metal/C nanofibers according to the pO₂ in selective oxidation. At the lowest pO₂, full-filled C nanofibers are formed with the embedded metal nanoparticles by the carburization. At higher pO₂, hollow C nanofibers start to form and metal is agglomerated within the core of nanofibers. As the pO₂ increases, the degree of C decomposition is accelerated and the diameter of inner hollow core increases. This structure evolution induces metal/C core/shell nanofibers. Furthermore, this continuing C combustion can induce the formation of

Chapter 5: Selective Carbon Oxidation induced Hollow Structure Formation in Metal/Carbon Nanofibers

hollow and porous C nanofibers with enlarged metal agglomerates inside and outside nanofibers.

Figure 5.2a shows the Ellingham diagram for denoting the oxidation ΔG° of metals (Fe, Co, Ni, Cu, Pt) and C. By comparing the ΔG° of each species at constant temperature of 700 °C, oxidation tendencies of them can be identified. At 700 °C, Fe shows higher oxidation tendency ($\Delta G^\circ = -405.05 \text{ kJ/mol}$) than C ($\Delta G^\circ = -396 \text{ kJ/mol}$). It means that selective C oxidation and reduction of Fe doesn't occur, and Fe oxides are expected to form. Unlike Fe, the oxidation tendencies of Co, Ni, Cu, and Pt are lower than C. They can induce selective oxidation of C with metal reduction. The oxidation tendency is increasing with the series of Pt, Cu, Ni, and Co.

To figure out the phase of metal ion and C after calcination under O_2 ambient, metal (Fe, Ni, Co, Cu)-C-O ternary phase diagrams were considered by FactsageTM calculation (**Figure 5.2b**). Tie-lines in Fe-C-O phase diagrams were constructed by linking the Fe oxide (Fe_2O_3 , Fe_3O_4) and C. It represents the tendency of Fe oxide dominant phase formation and is related with the higher oxidation tendency than C. However, the other metals such as Ni, Co, and Cu showed the phase diagrams whose tie-lines are connected with the C oxide and metal element. It represents the tendency of C oxide dominant phase formation.^[35] Based on the thermodynamic calculation-induced ternary phase diagram, we expected the formable phases by applying the mole fraction of metal-C-O in experiments. Their mole fraction was calculated from the amount of metal precursor [copper acetate: $\text{Cu}(\text{COOCH}_3)_2$, cobalt acetate: $\text{Co}(\text{COOCH}_3)_2$, nickel acetate: $\text{Ni}(\text{COOCH}_3)_2$, chloroplatinic acid: H_2PtCl_6 , and iron nitrate: $\text{Fe}(\text{NO}_3)_3$] and polymer matrix (polyvinyl alcohol: $(\text{C}_2\text{H}_4\text{O})_x$), O_2 pressure in chamber, and the mass of electrospun specimen. According to the $p\text{O}_2$ to induce selective oxidation, the metal-C-O mole fraction can be changed. The $p\text{O}_2$ was

Chapter 5: Selective Carbon Oxidation induced Hollow Structure Formation in Metal/Carbon Nanofibers

induced as 0.010 (red), 0.025 (orange), 0.050 (green), 0.060 Torr (blue) and the mole-fractions at each condition were marked with the shape of stars. In the case of Fe, Fe₂O₃, C, O was expected to form without pure Fe at the pressure condition from 0.010 to 0.060 Torr. In contrast, other reductive metals of Co, Ni, Cu were expected to form metal-CO-O. In the case of Co, Ni, calcination pressure conditions over 0.050 Torr is expected to induce metal-metal oxide-C oxide products in **Figure 5.2b**.

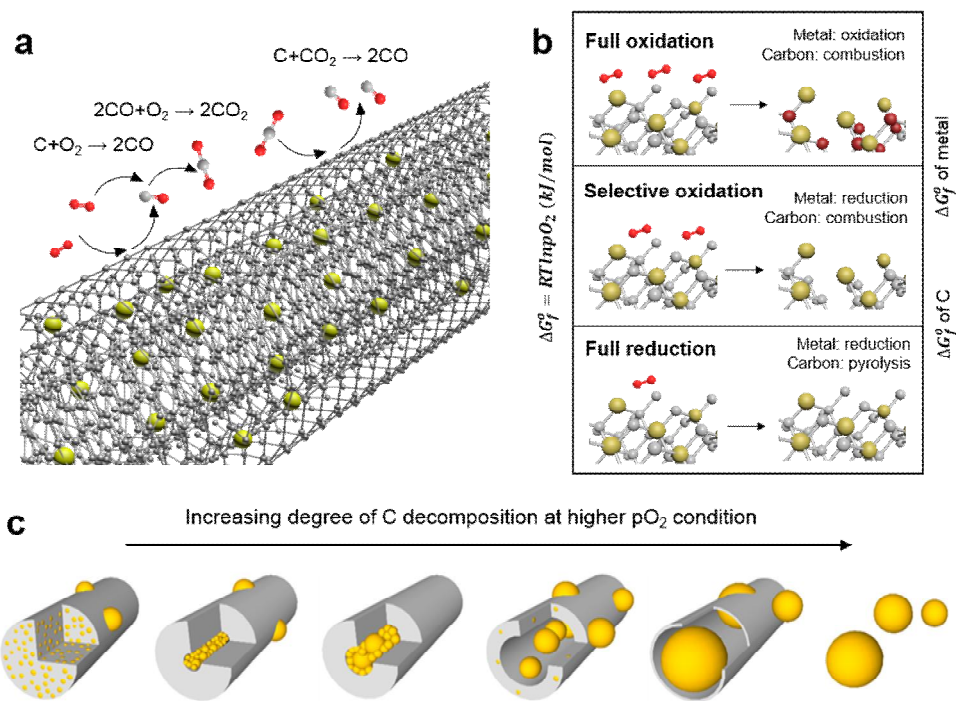


Figure 5.1. Thermodynamic consideration about gas-solid reactions in the calcination of metal precursor + polymer matrix nanofibers. **(a)** Schematics for indicating gas-solid reactions between gaseous O_2 and solid state metal + C atoms in nanofiber system. **(b)** Categorization of redox reactions of metal and carbon (C) such as full reduction, selective oxidation, and full oxidation according to the oxidation Gibbs free energy (ΔG). **(c)** Schematic for structure evolution of metal/C nanofibers with increasing oxygen partial pressure (p_{O_2}) in selective oxidation region.

Chapter 5: Selective Carbon Oxidation induced Hollow Structure Formation in Metal/Carbon Nanofibers

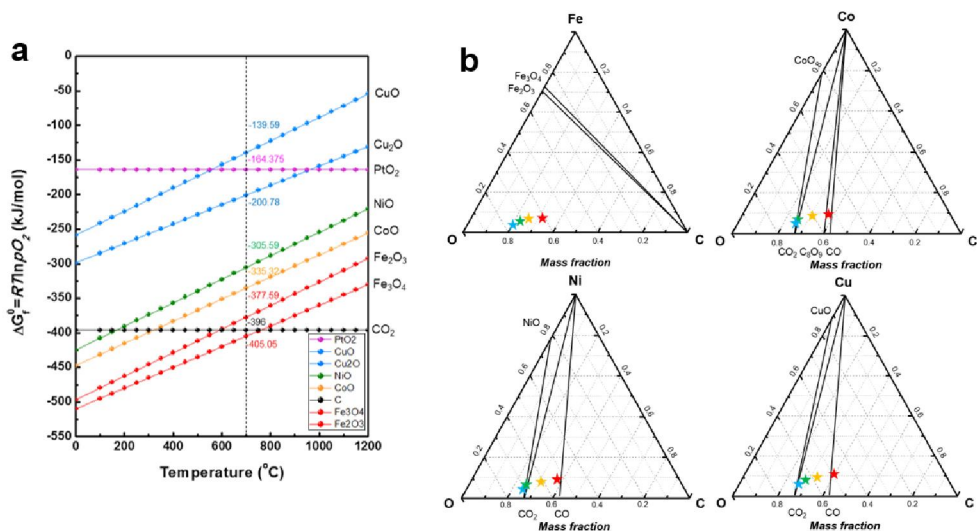


Figure 5.2. (a) Ellingham diagram for indicating oxidation tendency of C and various metals such as Fe, Co, Ni, Cu, and Pt. (b) FactsageTM calculated ternary phase diagrams of metal (Fe, Co, Ni, Cu)-C-O system for prediction of materials composition between metal precursor and polymer matrix, and relative ratio between chamber pressure and mass of specimen.

5.3. Structure evolution of reductive metal/carbon nanofibers with the hollow structure formation

Figure 5.3 shows the structures of metal/C nanofibers after calcination under high vacuum ($<10^{-5}$ Torr) and pressures for selective oxidation (0.010, 0.025, 0.050, 0.060 Torr). They generally indicate that C decomposition induces the formation of hollow and porous structures. To investigate the aspects of structure evolution, we compared the structures of metal (Co, Ni, Cu, Pt)/C nanofibers. Fe has been excluded because of oxide formation at the pressure range.

Interestingly, the rate of combustion based C decomposition differed according to the metal types. In the case of Co (**Figure 5.3a**), 10 nm sized Co nanoparticles were formed outside C nanofibers at the high vacuum condition. They were densely distributed at the surface of nanofiber. With the existence of O₂ during calcination, hollow and porous C nanofibers with 25 nm-sized Co nanoparticles formed from 0.010 Torr calcination. With increasing pressure, C decomposition became severe and the size of pores at the nanofiber surface increased. Simultaneously, enlarged 50 nm sized Co nanoparticles were placed inside and outside nanofibers. At the pressure above 0.050 Torr, most C were decomposed and Co agglomerates formed with the grains.

Ni showed similar structure formation tendency with the case of Co (**Figure 5.3b**). At high vacuum, 20nm-sized Ni nanoparticles formed and placed inside C nanofibers. At 0.010 Torr, hollow and porous C structures were generated with the enlarged Ni nanoparticles. At 0.025 Torr, C nanofibers were decomposed and started to be disconnected. Especially, Ni particles grew and bamboo-like Ni agglomerates formed

Chapter 5: Selective Carbon Oxidation induced Hollow Structure Formation in Metal/Carbon Nanofibers

inside nanofibers. Similar with the Co, pressure above 0.050 Torr induced Ni particles formation with the severely decomposed porous C nanofibers.

However, as investigated in chapter 4, Cu shows a different structure evolution aspect with Co and Ni (**Figure 5.3c**). At high vacuum, 5nm-sized Cu nanoparticles are embedded within C nanofibers. Unlike Co and Ni which formed hollow and porous C nanofibers, 0.010 Torr calcination formed similar structure of Cu/C nanofibers with high vacuum calcination. As the pressure increases, 0.025 Torr calcination induced Cu/C core/shell nanofibers. 0.050 Torr calcination induced hollow C nanofibers with Cu agglomerates. At 0.060 Torr, hollow and porous C nanofibers were formed and this structure was similar with the Co/C, Ni/C nanofibers formed at 0.010 Torr calcination. By regarding metal/C nanofiber structure evolution predicted in **Figure 5.1c**, they proceeded with the order of full-filled C nanofibers, metal/C core/shell nanofibers, hollow C nanofiber, and porous C nanofiber. These aspects were regularly induced in Cu. In the case of Co and Ni, full-filled and core/shell nanofibers would be formed at the pressure below 0.010 Torr due to high degree of C decomposition.

Pt showed the lower degree of C decomposition than Cu. **Figure 5.3d** displays the structure evolution of Pt/C nanofibers after calcination according to the ambient condition. At high vacuum, 5nm-sized Pt nanoparticles were fully-embedded in C nanofibers. Interestingly, this structure formation was repeated until the pressure range of 0.010~0.050 Torr and it means that C decomposition in Pt/C nanofibers was retarded even though the pressure was high enough to form hollow and porous C structures in other metals. Eventually, Pt/C core/shell nanofibers were formed at 0.060 Torr. Comparing the pressure which induced Cu/C core/shell nanofibers as 0.025 Torr, slow C decomposition in Pt/C system has been investigated.

Chapter 5: Selective Carbon Oxidation induced Hollow Structure Formation in Metal/Carbon Nanofibers

There exists metal type dependence on combustion based C decomposition (**Figure 5.3e**). With the order of Co>Ni>Cu>Pt, C decomposition rate was decreased. From this result, it can be revealed that the C oxidation and formation of hollow C structure has an intimate relationship with the metal.

Chapter 5: Selective Carbon Oxidation induced Hollow Structure Formation in Metal/Carbon Nanofibers

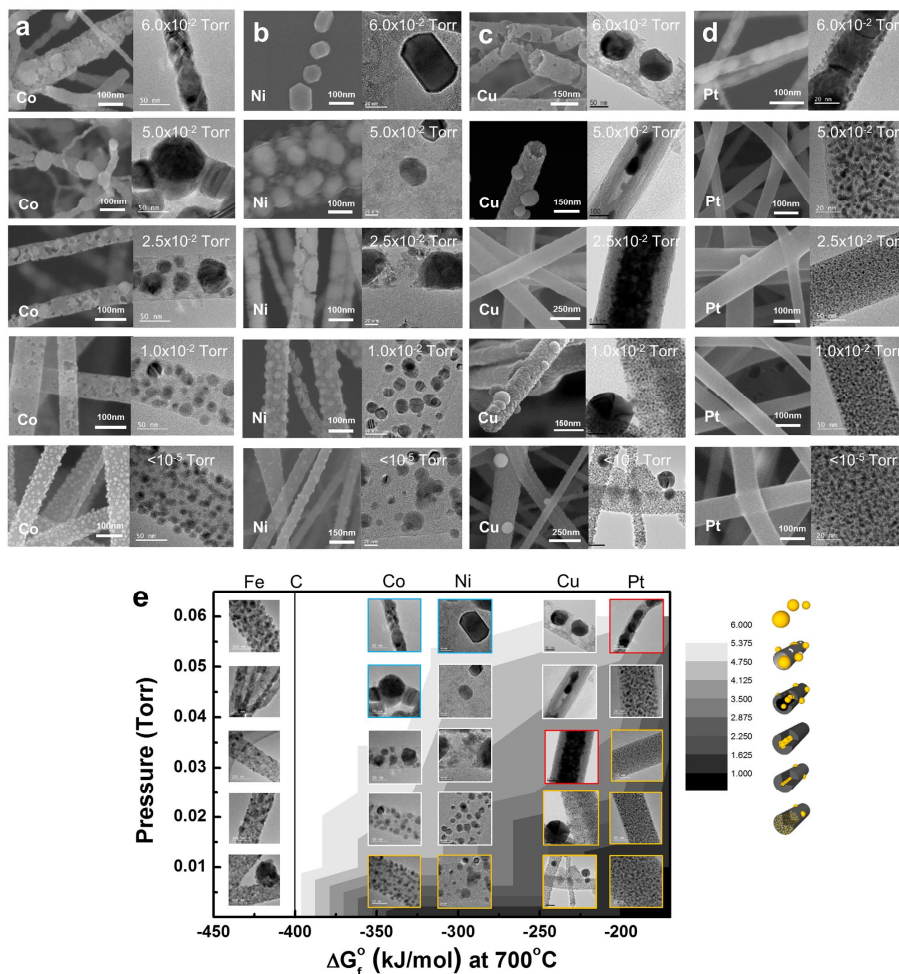


Figure 5.3. FE-SEM and TEM images for displaying the metal/C nanofiber structures of (a) Co, (b) Ni, (c) Cu, and (d) Pt with the pressure control in the series of high vacuum ($< 10^{-5}$ Torr), 1.0, 2.5, 5.0, and 6.0×10^{-2} Torr during the calcination temperature and time of 700 °C and 5h. With increasing pressure, hollow and porous C structures form. Compared to metal/C nanofibers formed by high vacuum calcination, the selective oxidation based structures show higher C decomposition degree. (e) Difference of the pressures which induce hollow and porous structures according to the metal types.

*Chapter 5: Selective Carbon Oxidation induced Hollow Structure
Formation in Metal/Carbon Nanofibers*

5.4. Catalytic carbon oxidation on metal surface

It is required to verify the site-dependence of C oxidation to understand the structure evolution mechanism of metal/C nanofibers. Regarding on the experimental results in **Figure 5.3**, the preferred C oxidation at the surface of metal should be considered. To determine the preference of C oxidation, the energies in the process of O₂ dissociation, CO formation were calculated by density functional theory (DFT).

Figure 5.4 shows the result of DFT calculation about C oxidation process at the vacuum and metal surface. Cu was selected as a representative metal in this calculation and the energies for CO and CO₂ formation process were calculated. Red dots and green lines in **Figure 5.4a** indicate the energy levels in vacuum and Cu (111) surface. Reaction coordinates in x-axis are steps for C oxidation process. Coordinate 1 indicates the status for existence of one O₂ molecule and one C atom. Coordinate 2 is the status of two O atoms by breaking the bonding of O₂ molecule and one C atom. Coordinate 3 indicates the status for formation of CO molecule by C-O atom bonding and the existence of one O atom. Coordinate 4 is the status for CO separation from the metal surface. The energy levels (green) of metal surface between the reaction coordinates are energy barriers between each step. In the case of vacuum, the energy of 6.47 eV is required to break the O-O bonding in O₂ molecules. It is an activation energy barrier between the coordinate 1 and 2. Relative energy of -5.29 eV in coordinate 3 reveals the stable formation of CO molecule. There are 2 steps and 3 processing status for CO formation in vacuum. In contrast, there are 5 steps and 6 processing status for CO formation in metal surface. The most important discovery is that the activation energy to proceed the reaction is negligible compared to the vacuum case. Compared to initial state, energy level of reaction coordinate 2 is -2.63

Chapter 5: Selective Carbon Oxidation induced Hollow Structure Formation in Metal/Carbon Nanofibers

eV and 0.28 eV is an activation energy to dissipate O₂ molecule. The energy level for CO formation is -5.20 eV and 0.02 eV is required to overcome activation energy. The energy level for CO separated status is -4.29 eV and 0.91 eV is required. Therefore, 1.21 eV is required in the case of metal surface and it is lower than the required energy of 6.47 eV in vacuum.

CO₂ formation shows the similar aspect with the case of CO. In **Figure 5.4b**, there are 6 coordinates for the formation of CO₂. Coordinate 1 is the status for two O₂ molecules and one C atom. Coordinate 2 indicates the two O atoms from O-O bonding breaking, one O₂ molecule, and one C atom. Coordinate 3 is the status for generation of one CO molecule by bonding between O and C atom, and existence of one O atom, one O₂ molecule. Coordinate 4 is for indicating two O atoms formation from the rest O₂ molecule. There exist three O atoms and one CO molecule. In coordinate 5, one of the three O atoms makes a bonding with CO and it forms CO₂ molecule. There exist two O atoms and one CO₂ molecules. Coordinate 6 is the status for CO₂ separation from the surface and it is not related with the vacuum case. In the case of vacuum, there are 4 steps and 5 processing status for CO₂ formation. In the case of metal surface, there are 9 steps and 10 processing status. Unlike the vacuum condition which requires the energy of 12.94 eV to overcome the activation energy, only 1.57 eV is required totally on metal surface. Therefore, the C oxidation is preferred at the metallic surface than vacuum. It means that C oxidation in metal/C nanofibers starts from the interface between metal and C.

The detailed procedure has been calculated according to the displacement of O and C at the metal surface step-by-step (**Figure 5.5**). On the metal surface, O-O separation is preferred than bonding state. It can be determined from the energy status in **Figure 5.5a, c**. For O₂ dissipation, only energy to overcome the barrier is required. In DFT

Chapter 5: Selective Carbon Oxidation induced Hollow Structure Formation in Metal/Carbon Nanofibers

calculation, Ni (111) surface requires 0.297 eV and Cu (111) surface requires 0.277 eV. Furthermore, from the lower energy in the case of CO bonding than C-O separation, it can be revealed that CO formation can be promoted at the metal surface. Energies to overcome the barrier are 0.892 eV in Ni (111) surface and 0.025 eV in Cu (111) surface. From these results, C oxidation on metal surface can be promoted than vacuum states.

Based this phenomenon, C oxidation process in metal/C nanofiber system can be explained by **Figure 5.6**. C oxidation proceeds at the interface between metal and C, not the outer surface of C nanofibers. Firstly, O₂ molecules are adsorbed at the metal surface. Secondly, O₂ dissociation occurs and O diffuse toward the C to generate gas state CO, CO₂. Thirdly, C-O bonding is generated and gaseous CO, CO₂ are mainly formed near the metal surface. Figure shows the overall C oxidation process at the metal surface step-by-step. This process includes C adsorption, O adsorption, O₂ dissociation, CO formation at the metal surface, and CO desorption.

To verify this hypothesis, we calculated the bonding energy between metal and C, O, CO (**Figure 5.7**). In the case of C and O adsorption, higher bonding energy indicates the preference of adsorption. In contrast, lower bonding energy indicates the preference of CO desorption. Due to the extremely low energy in O₂ dissociation and CO formation, these terms have been excluded in consideration. In the case of C adsorption, there was no clear trend between the types of metals. Pt, Ni, Co showed similar bonding energies and Cu showed the lowest energy of 5.1361 eV. Although the absolute values of binding energies are high, the amount of C around metals is high enough in metal/C nanofibers. Therefore, C adsorption term shows low significance to verify our hypothesis. O adsorption showed the clear trend according to the types of metals. Co showed the highest adsorption energy with O as 5.9169 eV.

Chapter 5: Selective Carbon Oxidation induced Hollow Structure Formation in Metal/Carbon Nanofibers

Ni was 5.5665 eV, and Cu was 4.9724 eV. Pt was 4.4192 eV and it showed the lowest adsorption energy with O. This adsorption energy trend is coincident with the formation rate of hollow C nanofiber in **Figure 5.3**. In fact, Co with the highest O adsorption tendency showed the hollow C nanofiber formation at the 0.010 Torr which denotes the lowest p_{O_2} . It means that at the Co surface, C oxidation is promoted and hollow structures are easy to form. In contrast, Pt with the lowest O adsorption tendency did not show the hollow C nanofiber formation until 0.060 Torr. Instead, Pt/C core/shell nanofibers formed at 0.060 Torr, which formed at 0.025 Torr in Cu/C nanofibers. From this result which denotes the tendency matching with the O adsorption energy and combustion based hollow C nanofiber formation, the mechanism of metal/C nanofiber structure formation can be explained by the promoted C oxidation at the metal surface. Especially, among the whole process of C oxidation in selective oxidation of metal/C nanofibers, the O adsorption is a rate-determining step.

CO desorption step can affect the pore accumulation process. After C oxidation at the metal surface, gaseous compounds such as CO (g) and CO₂ (g) are generated. Energies in **Figure 5.7** indicate the bonding energy between CO and metal. Therefore, high energy value means lower degree of CO desorption from the metal surface. In the case of Cu whose bonding energy between CO and Cu surface shows the lowest value of 5.7431 eV, hollow tube shaped structures were formed at 5.0×10^{-2} Torr. In contrast, Co and Ni which show higher CO bonding energy of 8.4583 and 7.9123 eV form pores near the metal nanoparticles. These structures can be observed in 1.0×10^{-2} Torr condition of **Figure 5.3**. It is due to the high degree of bonding energy between CO and metal surface. Although the gaseous C decomposition products easily form, their migration toward the center of nanofibers and accumulation are retarded.

Chapter 5: Selective Carbon Oxidation induced Hollow Structure Formation in Metal/Carbon Nanofibers

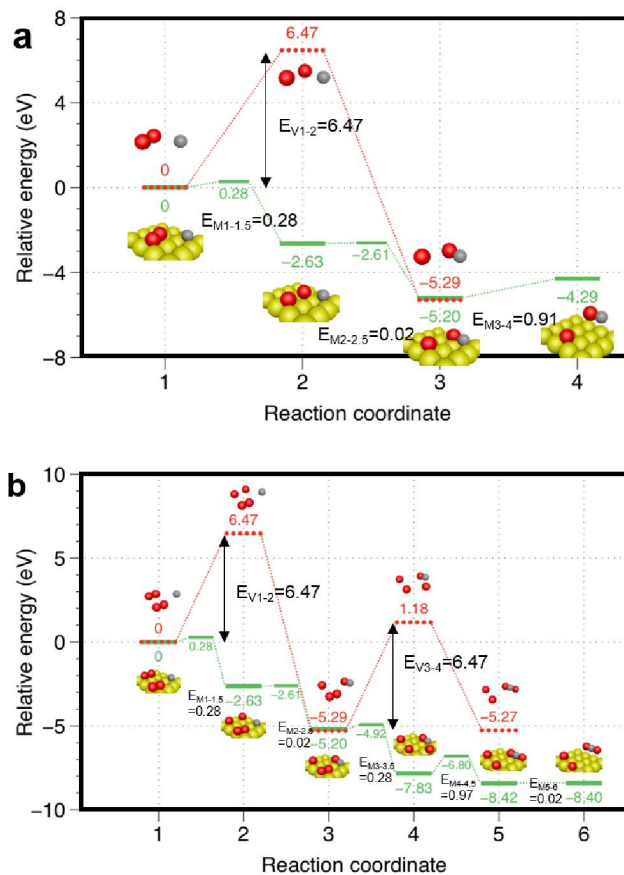


Figure 5.4. Mechanism of oxidation based C combustion process in metal/C hybrid nanofibers. Density functional theory (DFT) calculation to compare the preference of C oxidation at the metal surface and vacuum in the case of (a) CO and (b) CO₂ formation.

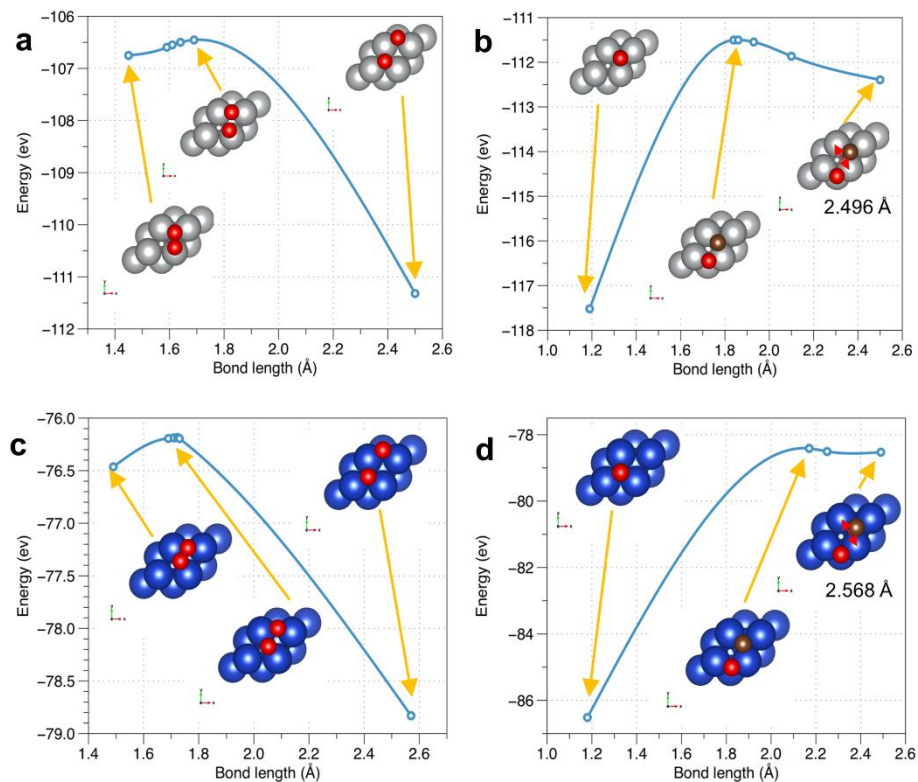


Figure 5.5. DFT calculation for energy computation in O_2 dissociation and CO formation on Ni (111) and Cu (111) surface. **(a)** O_2 dissociation on Ni (111) which shows the initial state for bridge-top and final state for two fcc site. **(b)** CO formation on Ni (111) which shows the initial state for two hcp site and final state for hcp site in perpendicular direction. **(c)** O_2 dissociation on Cu (111) which shows the initial state for bridge-bridge and final state for two hcp site. **(d)** CO formation on Cu (111) which shows the initial state for two hcp site and final state for fcc site in perpendicular direction.

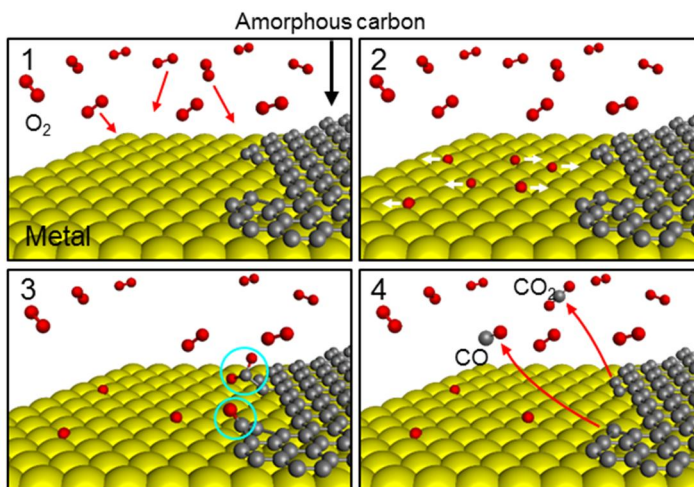


Figure 5.6. Schematic for general C oxidation process to form carbon monoxide (CO) and carbon dioxide (CO_2) on the surface of metal species.

Chapter 5: Selective Carbon Oxidation induced Hollow Structure Formation in Metal/Carbon Nanofibers

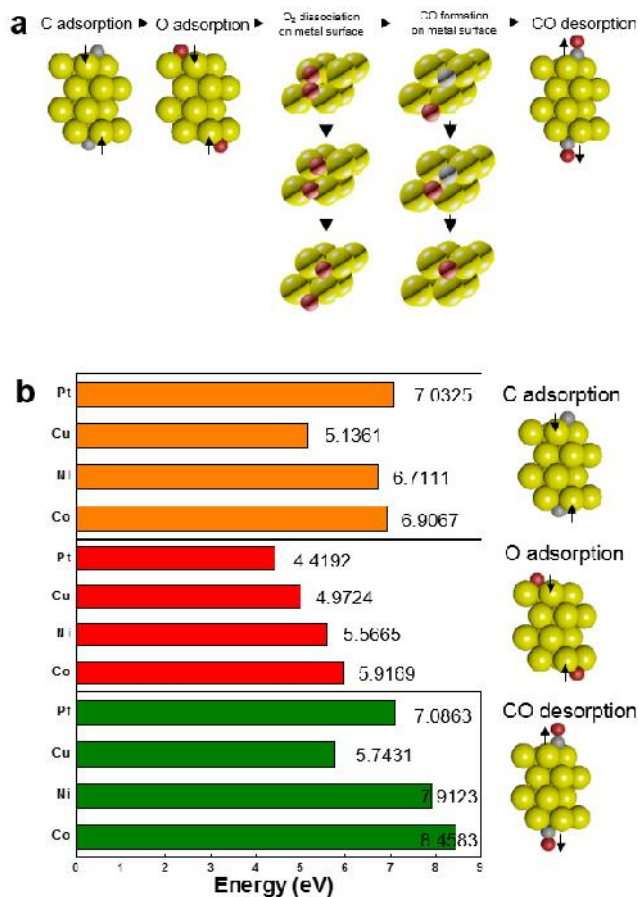


Figure 5.7. (a) Overall C oxidation steps of C adsorption, O adsorption, O₂ dissociation and CO formation on metal surface, CO desorption. (b) Density functional theory (DFT) calculation based energy consideration of C adsorption, O adsorption, and CO desorption according to the metals of Pt, Cu, Ni, Co.

5.5. Mechanism of hollow C structure formation

Based on the experiment and DFT calculation result, the mechanism of metal/C nanofiber structure evolution has been established in **Figure 5.8**. The chamber ambient for inducing selective oxidation is composed of O₂ molecules. Electrospun nanofibers contain metal precursor and polymer matrix. Polyvinyl alcohol (PVA) was used as a polymer matrix. After carburization, it is decomposed to amorphous C with low crystallinity. Simultaneously, metal ions in precursor are reduced to form pure metal clusters inside C nanofibers.

Due to selective oxidation (C oxidation and metal reduction), the pO₂ range where calcination proceeded induces the reaction of O₂ gas molecules with C solid atoms. However, C-O reaction is accelerated at the surface of metal nanoparticles. Therefore, O₂ migrates toward the interface between metal and amorphous C. By considering the plane view with the vertical direction of nanofiber axis, C at the outer region of metal preferentially decomposed than inner region. Continued C oxidation at the outer metal nanoparticles generates outside pore at the surface of nanofibers.

After the C consumption at the outward surface of metal nanoparticles, further C oxidation starts at the inner surface of metal nanoparticles. Simultaneously, C-C bonding regeneration proceeds at the terminated site, which is composed of highly-activated C. The reconstruction of vacancy defects in C has been revealed in carbon nanotube (CNT).^[41,42] C reconstruction can be explained by the reverse Boudouard reaction ($C + CO_2(g) \leftarrow 2CO(g)$). It is related with the experimental pO₂ control methodology in this work. After the formation of high vacuum ($<10^{-5}$ Torr) *via* extracting gas molecules from chamber, O₂ gas has been filled with chamber to the desired pressure. Therefore, as the calcination proceeds, the total chamber pressure

Chapter 5: Selective Carbon Oxidation induced Hollow Structure Formation in Metal/Carbon Nanofibers

increases due to the formation of gaseous products and increasing temperature. Based on Le Chatelier's principle, Boudouard reaction proceeds to reverse reaction for lowering the molar number of gaseous components from 2CO (g) to $\text{CO}_2 \text{(g)}$.^[32] Therefore, C can be generated from the gaseous decomposition products. CO (g) are transformed to the C and $\text{CO}_2 \text{(g)}$. With the continuous oxidation at the inward surface of metal nanoparticles, hollow C structure can be induced. Furthermore, C concentration gradient between the inside and outside nanofibers can induce outward C diffusion. By considering the concentration gradient related driving force of C diffusion and the diffusivity difference between C and metal, nanoscale Kirkendall effect can also induce the formation of hollow C nanofiber structures.

Chapter 5: Selective Carbon Oxidation induced Hollow Structure Formation in Metal/Carbon Nanofibers

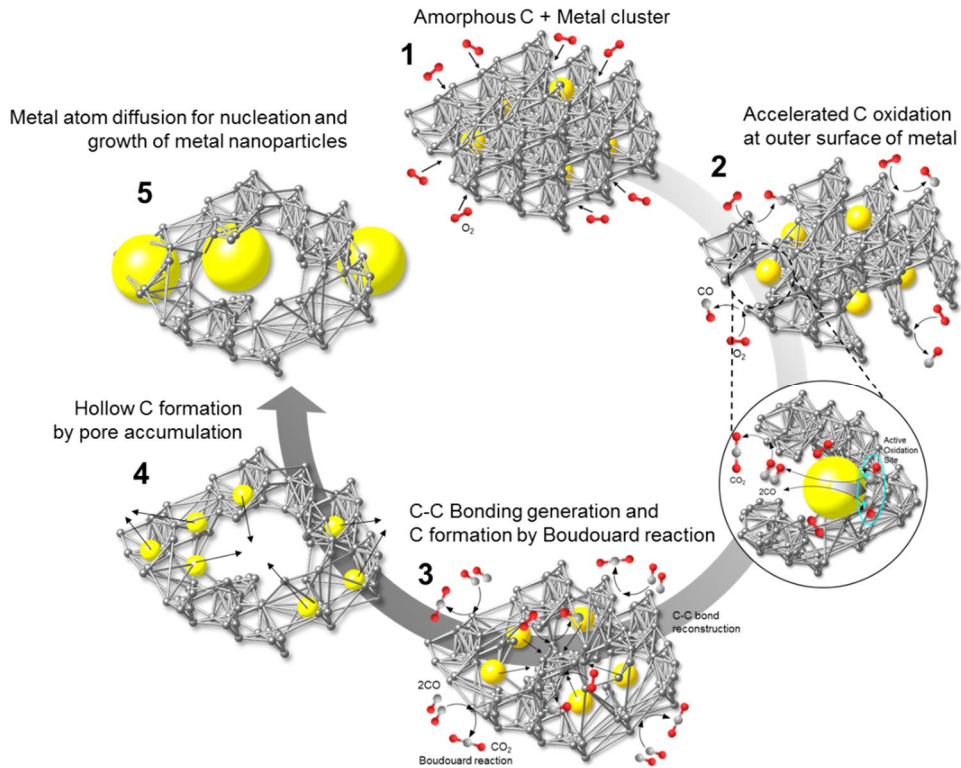


Figure 5.8. Procedure of hollow C structure formation in metal/C nanofibers by catalytic selective oxidation on metal surface. C matrix induced by calcination of polyvinyl alcohol (PVA) is amorphous structure. O_2 molecules diffuse toward metal located inside nanofibers because C oxidation is preferred at the metal surface. CO and CO_2 form at the matrix near the metal nanoparticles. Continuous C oxidation can induce hollow C structure by the accumulation of pores inside C matrix.

5.6. Summary

In this work, the effect of thermodynamic redox control between metal ion and C on the kinetics of metal/C structure formation has been studied. Considering Gibbs free energy for oxidation, there exists a difference between metal ion and C. Especially, transition metals such as Co, Ni, Fe and noble metals such as Ag, Au, Pt show lower tendency for oxidation than C. When those metals are fabricated as a metal/C hybrid material, selective oxidation of C and reduction of metal can be induced. This specific redox-control can induce the formation of diversified nanofiber structures from the same raw material. As the degree of C decomposition increases, C oxidation induces the formation of hollow and porous structure.

Interestingly, there exists a metal type-dependence on C oxidation. It is related with the intimacy with oxygen and it can be determined by Gibbs free energy in Ellingham diagram and DFT calculation about the bonding energies between metal and oxygen. Co showed the lowest Gibbs free energy for oxidation and highest bonding energy between metal surface with oxygen atom. In contrast, Pt showed the highest Gibbs free energy for oxidation and lowest bonding energy accordingly. The tendency of oxygen familiarity was the order of Co>Ni>Cu>Pt. In fact, Co showed the highest degree of hollow structure formation. Interestingly, the order of hollow structure formation according to the metal types was matched well with the order of oxygen intimacy. This result indicates that the metal affects the C oxidation aspects in the metal/C hybrid materials. It is related with the preferred C oxidation on metal surface than vacuum. The overall process of C oxidation at the metal surface can be explained by the 'C adsorption → O adsorption → O₂ dissociation → CO formation → CO desorption'. Based on this phenomenon, hollow structure formation can be explained by the

Chapter 5: Selective Carbon Oxidation induced Hollow Structure Formation in Metal/Carbon Nanofibers

continuous C oxidation and pore accumulation.

It has been revealed how the thermodynamic redox control between metal ion and C affects the kinetics of nanostructure formation. Especially, unlike bulk material, gas-solid reactions can control both phase and structure of the nanomaterials by inducing atomic diffusion with the dynamic motion of gaseous molecules. In this work, the role of metal has been firstly investigated in the structuring process of C nanomaterials, especially 1D structured nanofibers. Preferential C oxidation at the metal surface induced the unexpected atomic behavior of metal and C. Based on this phenomenon, a new-class of rational design for metal/C hybrid nanomaterials has been established. Furthermore, the catalytic role of metal has been firstly discovered as not only C formation such as graphene layer on Cu surface, but also oxidation based C combustion.

CHAPTER 6

Pressure Equilibrium based Carbon Porosity Engineering for Oxidative Metal Structure Control

6.1. Introduction

In this chapter, we report on a fabrication methodology for controlling the structures of oxidative metal by utilizing Boudouard reaction, related with pressure equilibrium between gaseous products from C oxidation. Unlike the reductive metal which shows lower ΔG than C, oxidative metal shows higher preference for oxidation than C. Therefore, selective oxidation is not adequate for structure control of oxidative metal. The porosity of C nanofibers is a key parameter to modulate the size and dispersion.

New active materials for greater lithium (Li) insertion with a higher capacity than graphite (372 mAh/g) is required. Li-alloy based anode materials including silicon (Si), tin (Sn), and germanium (Ge) have emerged as alternatives.^[43-45] Sn shows a great potential as a next generation anode due to its abundance, low cost and high theoretical capacity (993 mAh/g) with 4.4 Li per one Sn atom.^[46] A major drawback of Sn is large volumetric expansion (260%) during Li insertion, which causes

pulverization and rapid capacity loss.^[47] In order to mitigate these, several structural requirements should be satisfied. First, small and uniform Sn is required. It has been reported that fracture becomes less severe as the particle size decreases, and that particles with smaller diameter than the critical size do not fracture.^[48] Second, a buffer matrix for relaxing the volumetric expansion is required. The matrix should confine Sn nanoparticles to prevent their aggregation and pulverization. In zero-dimensional (0D) C matrix, Sn/C spheres formed by aerosol spray pyrolysis showed stable cycle performance.^[48,49] However, they required additives to bind the separated active materials. One-dimensional (1D) C matrix contributes to both confinement and the electron conduction path. However, in a pure Sn system, all Sn agglomerates formed outside the C nanofibers and additional treatments, such as ALD, were required to prevent the pulverization of Sn.^[50] It still remains a challenge to efficiently fabricate an ideal structure of Sn/C anode for LIBs.

Here, we present a novel fabrication method to optimize the structures of pure Sn/C nanofibers by tuning the porosity of C nanofibers. It is controlled by the pressure equilibrium related reactions between C nanofibers and gaseous decomposition products. Electrospun nanofibers are the most adequate 1D C matrix for anodes because they simultaneously provide a buffer matrix and conductive frameworks.^[51,52] For the synthesis of Sn/C composites, utilizing a Sn precursor is appropriate due to controllable size and dispersion of Sn nanoparticles.^[2,10] Therefore, calcination is required for the reduction of Sn ions and the decomposition of polymer matrix. We systematically controlled the outward metal diffusion in the C nanofibers. It should be minimized to confine Sn nanoparticles inside the C nanofibers. The calcination schemes were optimized to control the porosity of C nanofibers as a key parameter.

Chapter 6: Pressure Equilibrium based Carbon Porosity Engineering for Oxidative Metal Structure Control

This optimized Sn/C structure was enabled by confining the Sn nucleation site and minimizing the outward Sn diffusion originated from stress relaxation.

6.2. Gas-solid reaction based Sn/C structure control

To modulate the structure of Sn/C composites, outward Sn diffusion and the nucleation sites of Sn should be considered during calcination. The driving force for diffusion is stress relaxation, which originated from the differences in the thermal expansion coefficients (ΔCTE) between Sn ($23.5 \times 10^{-6} / ^\circ\text{C}$) and C ($1.5 \times 10^{-6} / ^\circ\text{C}$).^[21,53] Additionally, Sn has a low melting temperature of $232\text{ }^\circ\text{C}$.^[54] Calcination at $700\text{ }^\circ\text{C}$ induces melting and subsequent cooling after the isothermal region induces solidification. In the cooling region, Sn shrinks more than C (abrupt volume change) due to the large ΔCTE and Sn phase transforms from a liquid to a solid (density of solid: $7.18\text{ g}\cdot\text{cm}^{-3}$, liquid: $6.98\text{ g}\cdot\text{cm}^{-3}$).^[54] Sn tends to diffuse outward to relax this stress. Furthermore, due to the low melting temperature, Sn nucleation and grain growth easily occur. Because of this complicated phase transformation process, it is extremely hard to create nanocomposite structures with small Sn nanoparticles fully embedded. Therefore, it is important to utilize the outward Sn diffusion and confine the nucleation site with minimum grain growth *via* the structures of the outer C nanofibers.

The porosity of C nanofibers was determined to be a key parameter. We designed three different calcination schemes to understand the effect of porosity on the Sn structures and optimize the Sn/C nanofibers (**Figure 6.1**). To obtain a pure Sn phase, a low oxygen partial pressure ($p\text{O}_2$) was required due to the low Gibbs free energy of oxidation. There were two methods for inducing low $p\text{O}_2$. By extracting air from the chamber, the pressure decreased below 10^{-5} Torr, which was denoted as high vacuum (HV) calcination. Also, inert Ar gas formed a low $p\text{O}_2$ condition. The calcination schemes in **Figure 6.1a** were categorized into (1) stabilization + Ar (SA) calcination,

(2) HV calcination, (3) Ar calcination. The structures of Sn/C nanofibers were investigated using field-emission scanning electron microscope (FE-SEM) and transmission electron microscope (TEM). The average size and uniformity of Sn were analyzed using high magnification TEM images. The images were reproduced along the boundaries and the diameters of Sn nanoparticles was calculated with the assumption of a spherical shape (**Figure 6.2**). In SA calcination (**Figure 6.1b,c**), there were no embedded Sn nanoparticles inside the C nanofibers. Instead of Sn nanoparticles, large and diversely sized Sn agglomerates (average diameter: 94.43 nm) formed on the surfaces of the nanofibers. We denote them as SA calcination-induced nanofibers (SANFs). In HV calcination (**Figure 6.1d,e**), 16 nm Sn nanoparticles were embedded inside and 50nm Sn agglomerates were sparsely distributed outside of the C nanofibers. These materials were denoted as the HV calcination-induced nanofibers (HVNFs). Compared to SA calcination, the size and density of the outer Sn agglomerates decreased due to the same total amount of Sn. Finally, Ar calcination (**Figure 6.1f,g**) generated Sn nanoparticles fully embedded in C nanofibers without any outer Sn agglomerate. The average diameter of the Sn nanoparticles was 15.18 nm, and the size distribution showed the lowest standard deviation among the three conditions. Additionally, the density of the Sn nanoparticles was higher than that of the HVNFs. These materials were denoted as Ar calcination-induced nanofibers (ArNFs).

The effect of each calcination scheme on porosity is presented in **Figure 6.1a**. In the first scheme, stabilization (250 °C, air) for pre-decomposition of the polymer proceeded before the Ar calcination. However, the other schemes did not include stabilization. The main difference between HV and Ar calcination was the degree of inverse decomposition related to the pressure equilibrium. To quantitatively measure

the porosity of the nanofibers, we analyzed the Brunauer-Emmett-Teller (BET) specific surface area (SSA) in **Figure 6.3**. It was measured using the relative pressure of N₂ gas with adsorption and desorption at the isotherm of 77 K. Also, the total pore volume and pore size distribution were considered. In **Figure 6.3a**, the general shape of the isotherm indicated a mesoporous structure, as determined from the hysteresis related with capillary condensation phenomenon.^[55] Interestingly, SANFs show the highest BET SSA, and total pore volume as 98.97 m²/g and 0.0627 cm³/g. Additionally, there was an abrupt increase of volume at the low relative pressure range, which indicates a microporous structure. However, in the conditions without stabilization, the lack of knee-shaped isotherms is observed and the porosities are relatively low. ArNFs show the lowest BET SSA and total pore volume as 10.46 m²/g and 0.0217 cm³/g. Based on the Barrett-Joyner-Halenda (BJH) plot for investigating pore size distribution, SA calcination formed nanofibers with micropores (**Figure 6.3b**).^[56] It could be interpreted that stabilization forms micropores and increases the porosity of the nanofibers. Therefore, the amount of Sn diffusion is highest, and Sn agglomerates formed outside the C nanofibers during SA calcination. However, calcinations without stabilization produced different structures due to the lower porosity. Embedded Sn nanoparticles started to form as the porosity decreases. In Ar calcination, which had the lowest porosity, all of the Sn nanoparticles were embedded in the C nanofibers. These tunable structures of Sn/C nanofibers reveal the possibility of unrestricted control of the active materials in terms of porosity.

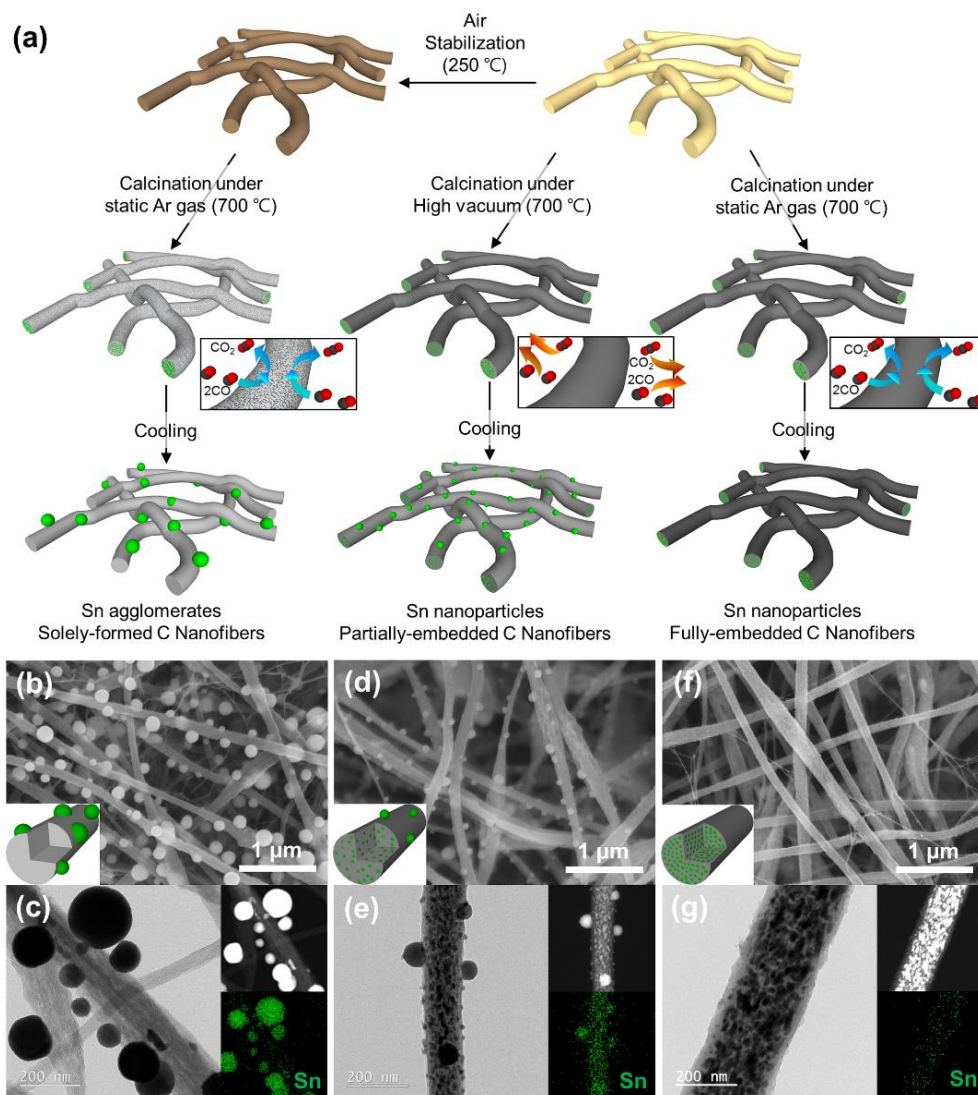


Figure 6.1. (a) Structural modulation schemes of the Sn/C nanofibers by controlling the porosity of the C nanofibers. FE-SEM and TEM images with HAADF, EDS of Sn/C nanofibers for Sn size and distribution comparison according to the calcination conditions. (b,c) SA calcination, (d,e) HV calcination, and (f,g) Ar calcination.

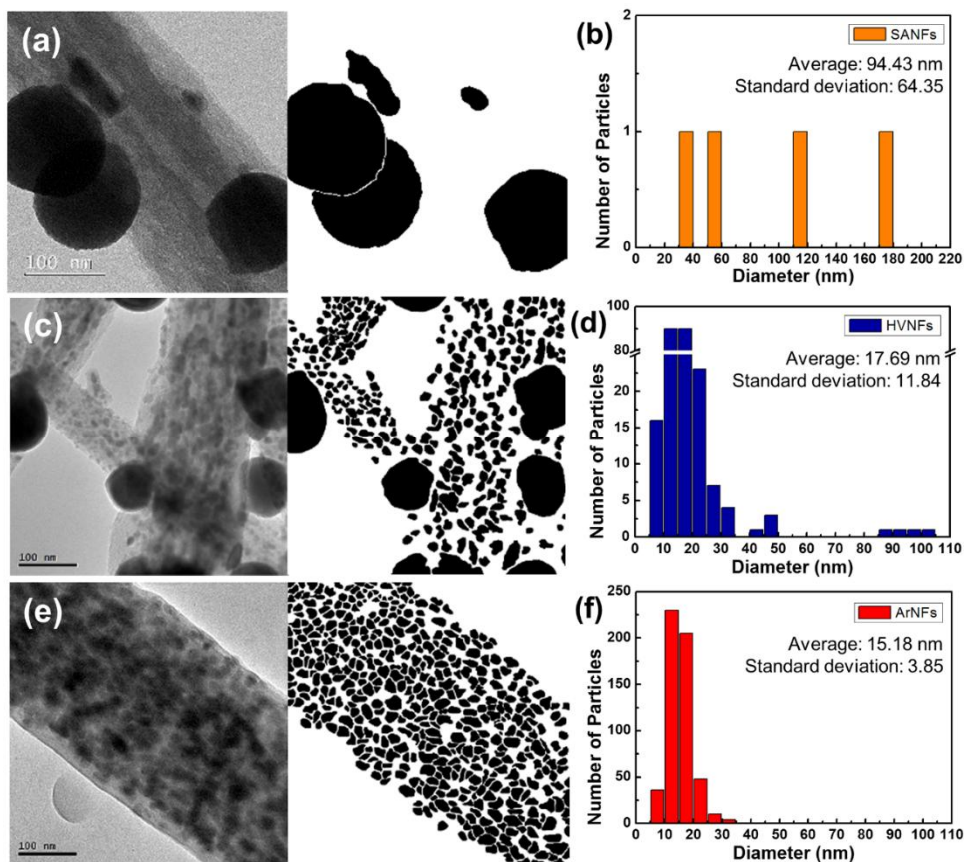


Figure 6.2. Transmission electron microscope (TEM) images, reproduced images for particle size and distribution analysis of the Sn/C nanofibers formed by (a,b) SA calcination, (c,d) HV calcination, and (e,f) Ar calcination. Sn particle distributions are represented by the histogram.

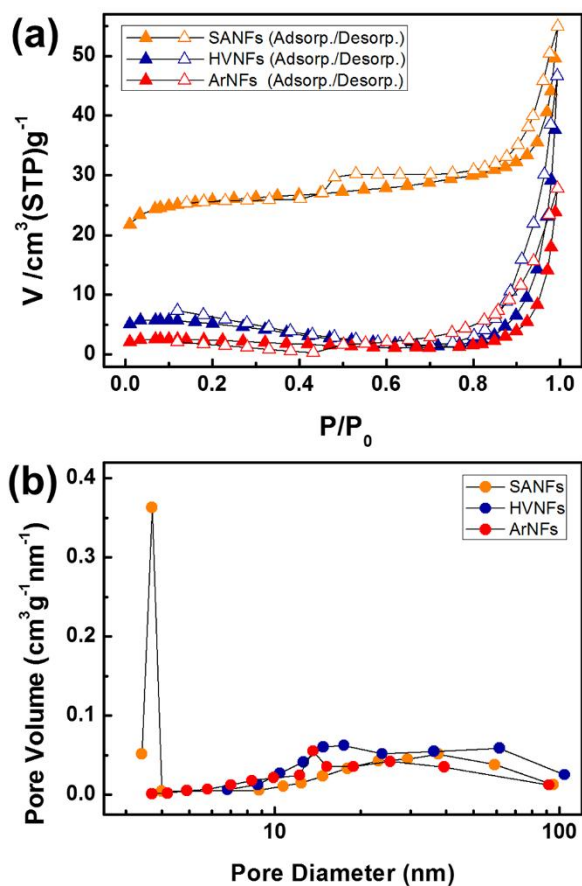


Figure 6.3. (a) Brunauer-Emmett-Teller (BET) specific surface areas of the Sn/C nanofibers according to the calcination conditions. (b) Comparison of the pore size distribution between the Sn/C nanofibers using the Barrett-Joyner-Halenda (BJH) plot.

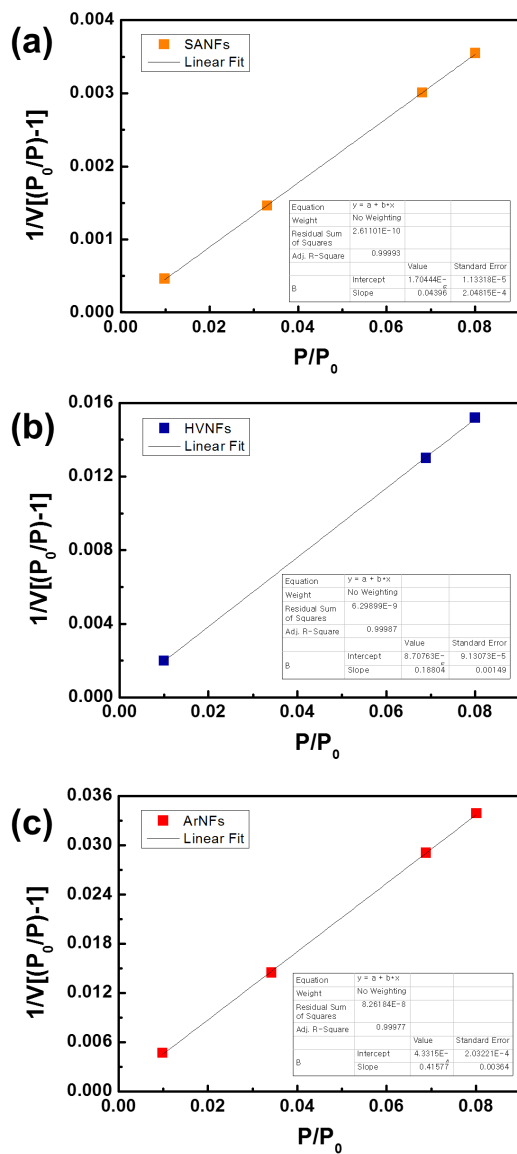


Figure 6.4. Fitting plot for investigating the Brunauer-Emmett-Teller (BET) surface area according to the relative pressure (P/P_0). **(a)** SA calcination, **(b)** HV calcination, and **(c)** Ar calcination.

Chapter 6: Pressure Equilibrium based Carbon Porosity Engineering for Oxidative Metal Structure Control

Table 6.1. Comparison of the BET surface area and the total pore volume of the Sn/C nanofibers formed using the various calcination conditions.

	SANFs	HVNFs	ArNFs
BET surface area (m ² /g)	98.97	23.14	10.46
Total pore volume (cm ³ /g)	0.0627	0.0358	0.0217

6.3. Effect of ambient condition on porosity of Sn/C nanofibers

To better understand the mechanism of porosity control, the effect of stabilization and the difference between HV and Ar calcination in gas-solid reactions were investigated in detail.

First, stabilization accelerated the decomposition of the polymer matrix.^[57] Thermal decomposition of Sn acetate (SnAc) and polyacrylonitrile (PAN) was analyzed using thermogravimetric analysis (TGA) and differential scanning calorimetry (DSC), as shown in **Figure 6.5**. To fabricate Sn/C nanofibers, electrospun SnAc + PAN nanofibers need calcination, which is related with the thermal decomposition of SnAc and PAN. Based on the ambient conditions, they are categorized into combustion and pyrolysis. To determine the thermal decomposition of SnAc + PAN nanofibers, TGA and DSC were carried out in air and N₂ gas at a scan rate of 3 °C/min (**Figure 6.5**). In TGA, the air condition showed a 51.59 % weight decrease from room temperature to 700 °C. In contrast, the N₂ gas (inert) condition showed a 38.50 % weight decrease. This result can be explained by the difference between oxidation-based combustion and reduction-based pyrolysis. In the case of air (**Figure 6.5a**), SnAc forms tin dioxide (SnO₂) *via* Sn oxidation, and PAN decomposes into gaseous products, such as CO₂ and H₂O. In the temperature range from 100 °C, the weight percent started to decrease due to dehydration. In DSC, there existed an exothermic peak at approximately 250~300 °C, which shows cyclization of the nitrile group in PAN and decomposition of the acetate precursor. The next exothermic peak

at approximately 450 °C indicates the decomposition of the polymer matrix *via* combustion. However, in the case of N₂ (**Figure 6.5b**), pure Sn phase can be formed *via* the reduction of SnAc. The pyrolysis products of PAN include not only gaseous products but also residual C with low molecular weight (M_w) hydrocarbons. There also existed an exothermal peak at approximately 270 °C which indicates cycling of PAN. When comparing the amount of heat in DSC, it can be determined that cycling proceeds more vigorously in air. Decomposition under air, in which stabilization (250 °C) proceeded, induced dehydration and cyclization of the polymer matrix with the gas products. Stabilization *via* pre-decomposition before calcination, induced higher porosity with micropores. Additionally, it increased the crystallinity of the C nanofibers with cross-linked hexagonal rings, which is related to the tautomeric changes to pyridine structure.^[58,59] It was revealed using Fourier transform infrared spectroscopy (FT-IR) by the peaks that disappeared at 2940, 1450 cm⁻¹ (C-H stretching, bending), and 2240 cm⁻¹ (C≡N stretching) and the peaks that appeared at 1595 cm⁻¹ (C-N, C-C stretching) and 1250 cm⁻¹ (C-C bond) in **Figure 6.6**.^[60] Through FT-IR, the effect of stabilization on the formation of Sn/C nanofibers can be investigated. FT-IR proceeded in the nanofibers after electrospinning, 200, 250 °C 1 h stabilization, and 700 °C 5 h calcination. In the electrospun nanofibers, peaks at 2940 and 1450 cm⁻¹ showed C-H stretching and bending, and the peak at 2240 cm⁻¹ showed C≡N stretching. However, after stabilization, these peaks started to disappear and peaks appeared at 1371 cm⁻¹ (C-N bond) and 1595 cm⁻¹ (C-N, C-C stretching), which shows the formation of cyclized hexagonal rings.⁴ As the stabilization temperature

Chapter 6: Pressure Equilibrium based Carbon Porosity Engineering for Oxidative Metal Structure Control

increased, these peak changes became clear at 250 °C. Finally, after 700 °C calcination, arrays of ring structures were formed, which was revealed by the peaks at 1250 cm⁻¹ (C-C bond).

Second, harnessing the pressure equilibrium precisely controlled the porosity of the C nanofibers. HV calcination maintained constant pressure due to flowing out behavior of gaseous products. However, in Ar calcination, the gate valve was closed at HV (< 10⁻⁵ Torr) and Ar gas was inserted to the desired pressure. When the pressure reached the desired conditions, the chamber was blocked by closing the gas valve and no gas was introduced to the chamber. In this static Ar condition, the pressure increased due to the formation of gas products from SnAc, PAN decomposition and kinetic energy ($=3kT/2$) originating from the high temperature of 700 °C. The major gas-solid reactions during calcination can be understood as the Boudouard reaction between solid C nanofibers, gaseous carbon dioxide (CO₂), and carbon monoxide (CO) as the decomposition products.^[31]



In this equation, the pressure difference in the chamber should be considered. Based on Le Chatelier's principle, the reaction proceeds to reach pressure equilibrium. In the HV calcination, there was no preferential direction for the reaction (**Figure 6.7a**). However, because the Ar calcination increased the chamber pressure, the above equation preferentially proceeded in the reverse direction and produced C + CO₂(g) from 2CO (g) to lower the molar number of gas components (**Figure 6.7b**). This inverse decomposition decreased the porosity of C nanofibers because of the

accumulation of solid C from the CO gas. It can be interpreted as a recycling of the decomposition products. Also, the weight percent ratio of C in the Sn/C nanofibers measured by X-ray photoelectron spectroscopy (XPS) was highest in Ar calcination (**Figure 6.7c**). Through this process, we precisely controlled the degree of porosity in the C nanofibers.

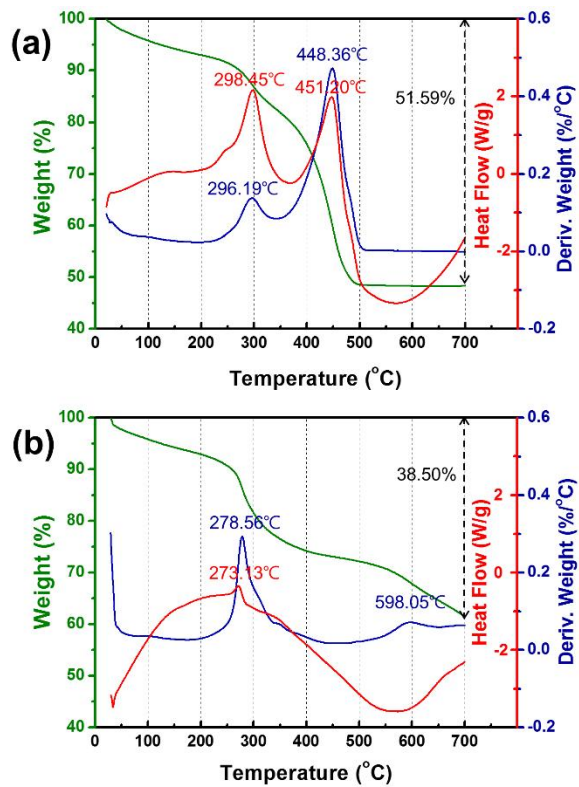


Figure 6.5. TGA and DSC of electrospun SnAc + PAN nanofibers to investigate the thermal decomposition process under (a) air and (b) N₂ gas flow in inert condition.

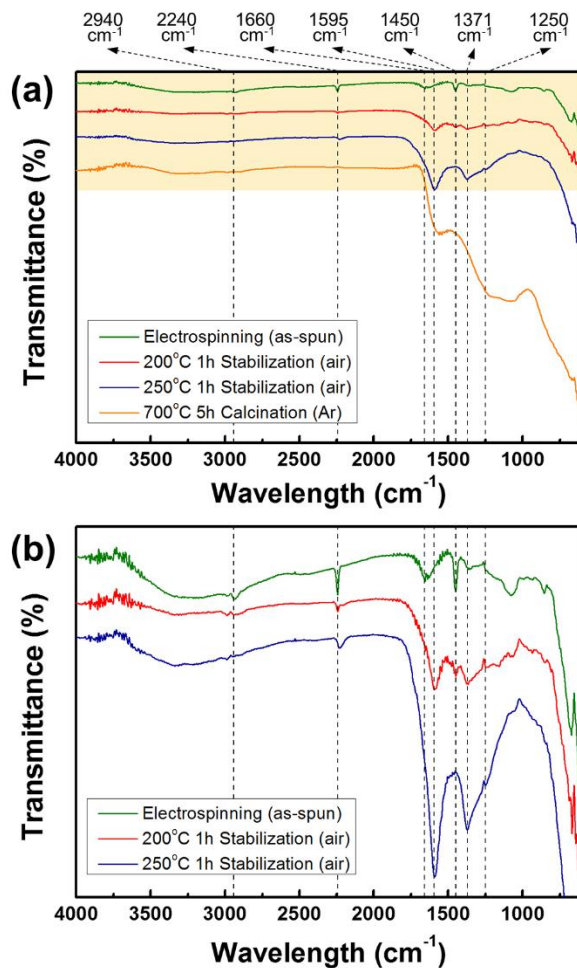


Figure 6.6. (a) FT-IR of Sn/C nanofibers from electrospinning to stabilization and calcination for investigating the thermal decomposition behavior of the SnAc and PAN. (b) Magnified range of transmittance in the FT-IR.

Chapter 6: Pressure Equilibrium based Carbon Porosity Engineering for Oxidative Metal Structure Control

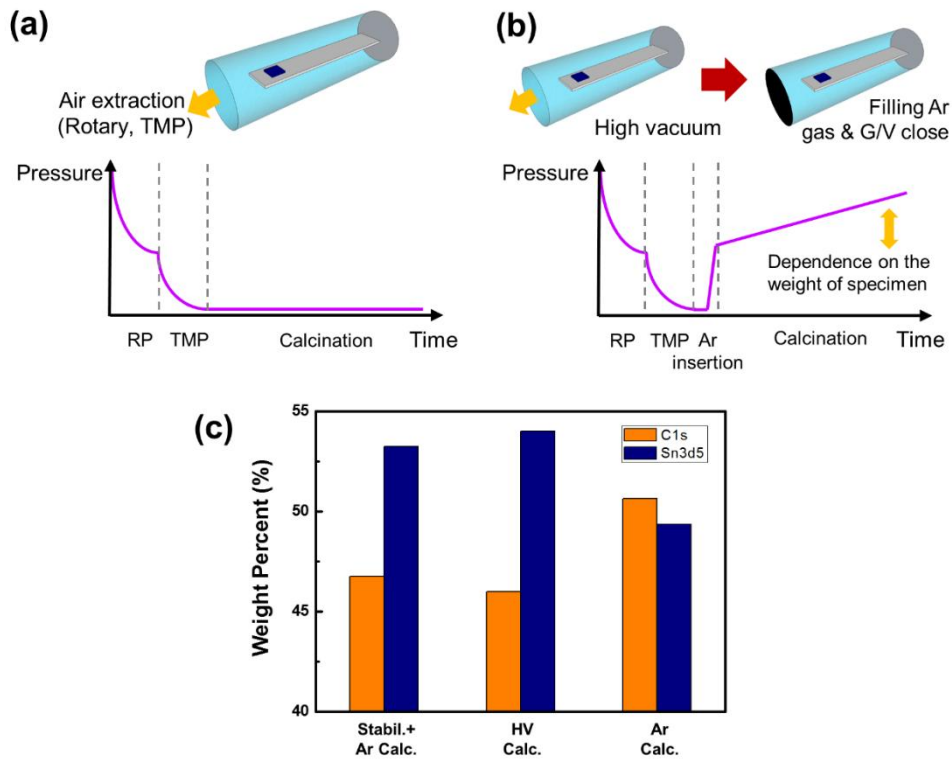


Figure 6.7. Calcination pressure and time profile schematics according to the tailoring methods of pressure equilibrium, such as (a) HV calcination and (b) Ar calcination. (c) XPS analysis for quantitative investigation of the weight percent ratio between C1s and Sn3d5 in the Sn/C nanofibers.

6.4. Material properties of Sn/C nanofibers

The materials properties of the Sn/C nanofibers were carefully characterized for using them as anode material. X-ray diffraction (XRD) and Raman spectroscopic analysis were carried out to investigate the Sn phase and crystallinity of the C nanofibers. Sn shows higher oxidation tendency than C and is easy to oxidize. The XRD results (**Figure 6.8a**) indicate that pure Sn phase formed in all Sn/C nanofibers. (Sn JCPDS no. 01-086-2265). The Raman analysis shown in **Figure 6.8b** showed the relative crystallinity difference of the C nanofibers. It is interpreted using the G band at approximately 1560 cm^{-1} , which is due to the stretching mode of sp^2 atoms (rings and chain), and the D band at approximately 1360 cm^{-1} , which is due to the breathing mode of sp^2 atoms (rings).^[61] The crystallinity, nanocrystalline size, ordering, and bondings of the C nanofibers could be obtained *via* peak intensity ratio (I_D/I_G) and peak shift (**Table 6.1**). Comparing the crystallinity, SANFs showed the lowest I_D/I_G as 0.97 which indicates the highest crystallinity. The stabilization, which induced dehydration and cyclized structure, enhanced the crystallinity. However, the schemes without stabilization, such as HV and Ar calcination, showed disordered C structures with relatively low crystallinities. HVNFs had the lowest crystallinity with an I_D/I_G of 1.116. HV calcination tended to produce lower crystallinity C nanofibers compared with Ar calcination. Considering I_D/I_G and the G band position, the structures of the C nanofibers are classified into groups of transition from graphite to nanocrystalline graphite.^[61] Crystallinity and graphitic crystallite size decreased in the following order: SANFs > ArNFs > HVNFs. This trend is an amorphization trajectory.^[61]

Figure 6.8c,d present the electrical properties of the Sn/C nanofibers. In current-voltage (I-V) sweeps, all nanofibers showed ohmic contact behavior, which means that they can be used not only as active materials but also current collectors without additives (**Figure 6.8c**). To precisely compare the electrical conductivities, the sheet resistance (R_s) was measured using the Van der Pauw method. The R_s of the SANFs with the highest crystallinity was 56.4 k Ω /sq and that of the HVNFs with the lowest crystallinity was 84.3 k Ω /sq (**Figure 6.8d**). The crystallinity of the C nanofibers affected the electron conduction. However, the lowest R_s of 15.7 k Ω /sq was obtained for the ArNFs where the Sn nanoparticles were embedded. These results indicate that not only the crystallinity of C but also the size and dispersion of the Sn can affect the electronic conduction. The latter property is intimately related to electron tunneling between metal nanoparticles.^[62] The barrier width and the energy of the electron-hole pair creation are affected by the radius and the volumetric fraction of the metal nanoparticles. Therefore, in the ArNFs, superior electrical conductivity could be obtained due to the combination of crystallinity of the C nanofibers and the uniformly sized Sn dispersion.

To quantitatively investigate the Sn oxide formation, XPS of the Sn 3d_{5/2} peak was performed (**Figure 6.9**). The binding energy of Sn⁰ is 484 eV and that of Sn²⁺ is 486 eV.^[63,64] Therefore, the formation ratio between them can be calculated from the integral of the binding energy area. Sn²⁺ and Sn⁰ oxidation states were obtained *via* peak deconvolution. Interestingly, unlike the XRD results, which indicated pure Sn, the XPS showed the co-existence of Sn and Sn oxide. It means that thin oxide layer was formed on the surfaces of the Sn particles due to the high oxidation tendency of Sn. We can compare the aspects of Sn oxide formation according to the structures of the Sn/C nanofibers. The Sn²⁺ ratio was highest in the ArNFs whose structure showed

Sn nanoparticles embedded C nanofibers and lowest in SANFs with Sn agglomerates outside the C nanofibers (**Figure 6.9d**). The oxide formation can be explained based on the structural aspects and the thermodynamic oxidation tendency difference between Sn and C. Based on the assumption of the same total Sn amount, the surface to volume ratio is highest in the ArNFs with 15.18 nm Sn nanoparticles. Sn has a higher oxidation tendency than C, which means that Sn oxidation proceeds with C reduction. In the ArNFs, the adjacent surface ratio of Sn was highest and SnO could be formed easily at the surface of Sn nanoparticles. In addition to the porosity of the C nanofibers, the SnO layers on the surfaces of the Sn particles contributed to confine the Sn size and structures.

To understand the effect of SnO on the electrochemical performance, the formation of Li₂O from SnO should be considered during lithiation and delithiation.



Li₂O is irreversibly formed from the SnO at the surface of active materials during the 1st lithiation. It is electrochemically inactive and can be a source of capacity loss after the 1st cycle. However, Li₂O can pin down Sn volumetric expansion, which is a critical problem for LIBs performance. To prevent volumetric expansion, other transition metal alloys were used in previous studies. Furthermore, Li₂O is a Li transporting solid electrolyte whose Li ion conductivity is $1.5 \times 10^{-9} \text{ (}\Omega \cdot \text{cm)}^{-1}$ at 25 °C. Optimized Sn structures with C nanofibers and adequate formation of Li₂O can contribute to the enhancement of anode performance.

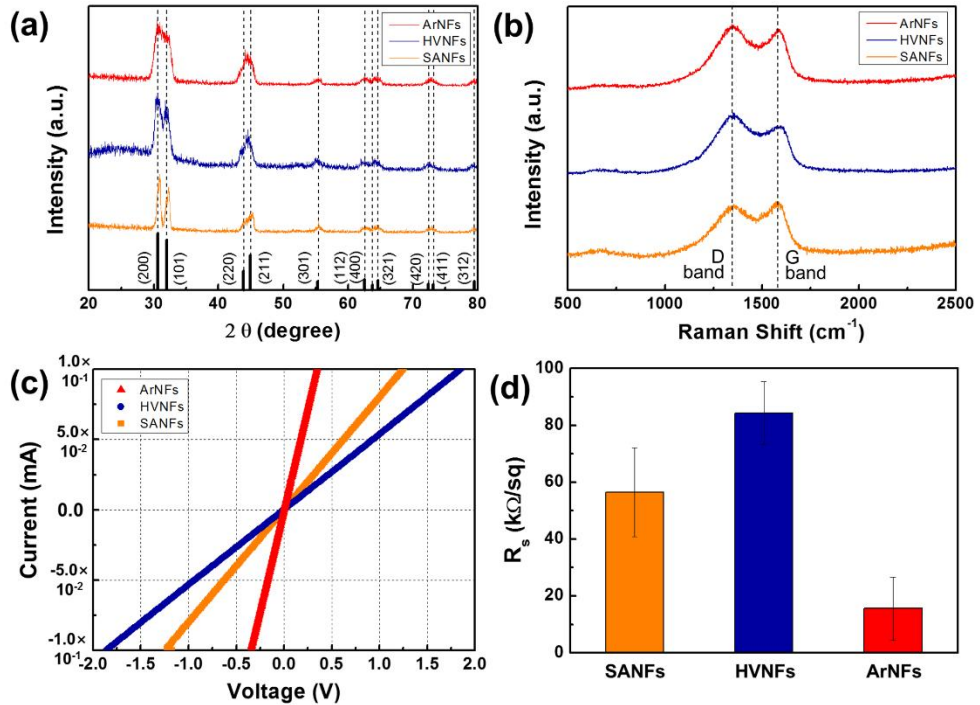


Figure 6.8. (a) XRD analysis for investigating the phase of Sn in the SANFs, HVNFs, and ArNFs. (b) Raman analysis for investigating the C crystallinity in the Sn/C nanofibers according to the calcination conditions. The electrical properties of the Sn/C nanofibers free-standing mats with (c) current-voltage (I-V) sweep and (d) sheet resistance measurement using the Van der Pauw method.

Chapter 6: Pressure Equilibrium based Carbon Porosity Engineering for Oxidative Metal Structure Control

Table 6.2. Parameters of the Raman analysis of the Sn/C nanofibers according to the calcination methods.

	SANFs	HVNFs	ArNFs
$I_D/I_G = R$	0.970	1.116	1.052
Graphitic crystallite size L_a (nm) = $4.4/R$	4.536	3.943	4.183
D band position (cm^{-1})	1355.98	1343.30	1345.43
G band position (cm^{-1})	1581.21	1594.47	1591.42

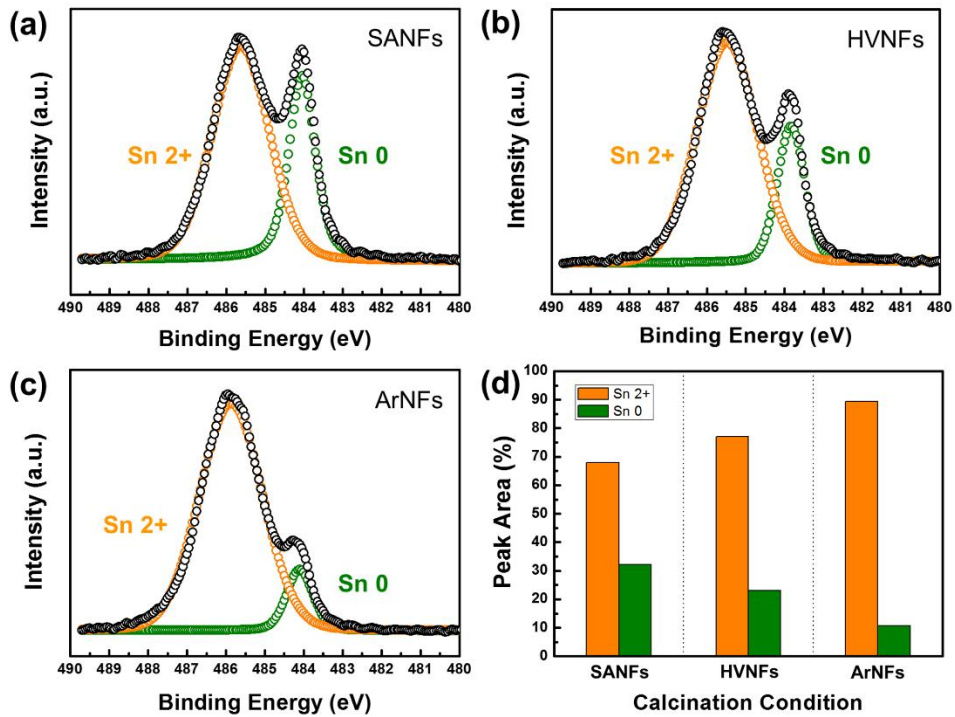


Figure 6.9. XPS analysis for investigating the oxidation states of Sn in (a) SANFs after SA calcination, (b) HVNFs after HV calcination, (c) ArNFs after Ar calcination. The relative differences between them are quantitatively represented by the (d) Sn $3d_{5/2}$ relative peak area.

6.5. All solid state Li-ion battery performance

The electrochemical properties of Sn/C nanofibers were investigated as the anode in all-solid-state LIBs without a current collector, binder, and conducting additives. With the 77.5Li₂S-22.5P₂S₅ glass solid-state electrolyte, the specific capacity (total mass of a punched disk from a Sn/C nanofiber mat) and coulombic efficiency were evaluated during 50 cycles with a rate of 0.05C (**Figure 6.10a**). Considering a theoretical capacity of Sn (993 mAh/g), ArNFs showed the highest capacity of 1260.41 mAh/g at the 1st discharge. However, the charge capacity did not fully recovered (59.64% efficiency) at 1st cycle due to the irreversible reactions related to the solid electrolyte interface (SEI) formed at the surface of the embedded Sn nanoparticles. Although the charge capacity decreased during the 1st cycle, the specific discharge capacity was maintained from 763.96 mAh/g (3rd cycle) to 761.86 mAh/g (50th cycle) in **Figure 6.10b**. Additionally, the coulombic efficiency was maintained at greater than 99.5% which indicates superior reversibility. There was no active material degradation in the ArNFs. It is an outstanding electrochemical performance obtained by nanostructured Sn/C anode. Furthermore, this result shows that ArNFs were successfully applied as the anodes for all-solid-state LIBs without any additives. Superior capacity and stable cyclability of ArNFs can be explained by the ideal Sn/C structures. The high surface to volume ratio of the Sn increases the number of reactive Li sites and the uniform dispersion of Sn promotes the buffer effect of the C nanofibers *via* balanced stress relaxation. In the case of the HVNFs, the discharge and charge capacities during the 1st cycle were 1039.70 mAh/g and 601.38 mAh/g (**Figure 6.10a**). The HVNFs showed a lower specific discharge capacity and a larger capacity loss from 589.16 mAh/g (3rd cycle) to 548.13 mAh/g (50th cycle) than the ArNFs (**Figure 6.10c**).

Considering the same Sn amount, the surface area of the Li reaction site was lower in the agglomerates than the nanoparticles. Therefore, the lower capacity of the HVNFs compared with the ArNFs can be explained by the coexistence of Sn agglomerates and nanoparticles. Also, the capacity loss after the 50th cycle is related to the outside position of the Sn agglomerates. Without managing the volume expansion of the anode materials, pulverization or cracking of the Sn can occur. Interestingly, the highest initial coulombic efficiency of 62.51% was obtained in the SANFs. Additionally, the lowest SnO ratio could minimize the capacity loss after the 1st cycle. However, consistent with the structural differences of Sn/C nanofibers, the lowest capacity during the 1st cycle was obtained for the SANFs (discharge: 939.70 mAh/g, charge: 587.38 mAh/g). The capacity started to decrease from 580.16 mAh/g during the 2nd cycle (**Figure 6.10a**). Not only the capacity but also the coulombic efficiency decreased to 98% as the cycling continued because of the Sn agglomerates formed outside the C nanofibers. It means that the microstructure of Sn/C composites affects their electrochemical performance more than their phase uniformity. A short circuit occurred after the 15th cycle. Considering the abrupt capacity decrease, the Sn was broken apart (decrepitation, crumbling). The repeated lithiation/delithiation induced stress in the Sn agglomerates. They were eventually separated from the nanofibers. The fractured structures and non-uniform distributions seem to be the main reason for the short circuit.

In the charge/discharge profiles of the ArNFs with a potential range of 0.005 – 1.8 V, there existed clear plateaus at 0.44, 0.56, 0.66, 0.70, and 0.76 V (**Figure 6.10b**). They represent the potential for the formation of Li-Sn alloys (Li_xSn , $0 < x < 4.4$) during charging and discharging. There existed a slight potential shift due to kinetic factors, such as polarization, and the longest plateau at 0.56 V indicated that $\text{Li}_{0.7}\text{Sn}$ was the

favorable phase from reaction kinetics point of view. Although capacity loss occurred after the 1st cycle, most plateaus remained in all 50 cycles. It can be determined that ArNFs are an ideal and optimized structure for the stress relaxation. Furthermore, based on the differential charge/discharge profiles, the reactions in the ArNFs proceeded faster than in the HVNFs due to the existence of clear peaks (**Figure 6.11**). As outer Sn agglomerates form and inner Sn nanoparticles disappear, an unclear and short plateau is observed in HVNFs (**Figure 6.10c**). The capacity was maintained as the cycling proceeded due to the embedded Sn nanoparticles. However, in the SANFs with outer Sn agglomerates, not only the length of the plateau but also the capacity abruptly decreased due to Sn degradation during the cycling (**Figure 6.10d**).

To investigate the rate capability of the Sn/C nanofibers, the rate was changed from 0.05 to 0.5 C (**Figure 6.10e**). These experiments proceeded for 5 cycles at each rate after 50 cycles of 0.05 C. Considering the conditions of the all-solid-state LIBs, the ArNFs and HVNFs showed good rate capability at the rate of 0.5 C. This improved rate capability can be attributed to the short electron diffusion lengths in the Sn structures. ArNFs with embedded Sn nanoparticles exhibited outstanding rate capability as expected. The cell was initially cycled at 0.05 C with a capacity of 762 mAh/g. With increasing rate, the discharge capacity decreased to 760 mAh/g at 0.1 C, 731 mAh/g at 0.2 C, and 592 mAh/g at 0.5 C. Although the HVNFs had lower capacity than that of ArNFs, it also showed a constant capacity at every rate condition. Comparing the rate capabilities, the ArNFs can discharge 10 times faster with a higher capacity of 592 mAh/g (0.5 C) than the HVNFs with 525 mAh/g (0.05 C).

This work focused on optimizing the structures of Sn/C nanofibers to achieve superior electrochemical performance. There was a lack of understanding about fundamental mechanisms for controlling the Sn structures in 1D C matrix including

Chapter 6: Pressure Equilibrium based Carbon Porosity Engineering for Oxidative Metal Structure Control

nanofibers. With the porosity control of C nanofibers, Sn nanoparticles embedded in C nanofibers could be induced for the first time. It is meaningful that systematic principles for utilizing the outward Sn diffusion were established and efficient fabrication schemes were designed to control the Sn size and dispersion.

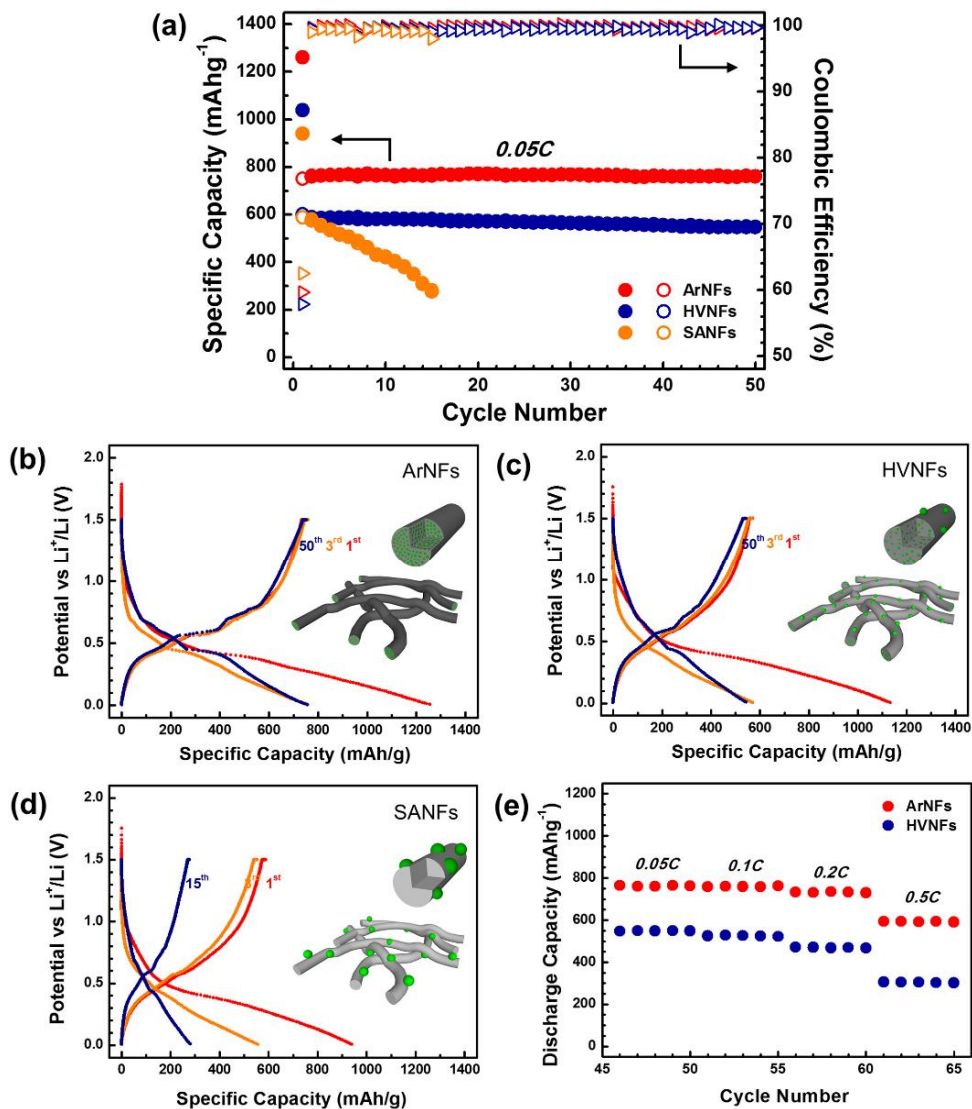


Figure 6.10. The electrochemical properties of the Sn/C nanofibers as the anodes of all-solid-state Li-ion batteries. **(a)** The cycle performances and coulombic efficiencies of the Sn/C nanofibers according to the Sn structures. The charge/discharge profiles of **(b)** ArNFs, **(c)** HVNFs, and **(d)** SANFs during cycling. **(e)** Comparison of the rate capability between HVNFs and ArNFs.

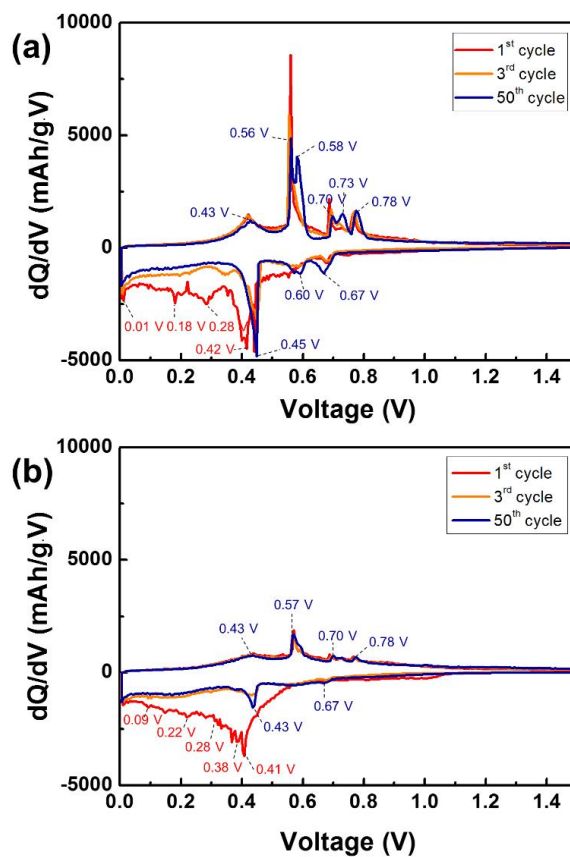


Figure 6.11. Differential charge and discharge profiles of (a) ArNFs and (b) HVNFs as the anodes in all-solid-state Li-ion cells from the 1st to the 50th cycle.

6.6. Summary

We have successfully developed a high performance Sn/C nanofibers anode of all-solid-state LIBs. It should be noted that the free-standing nanofiber mats were applied as electrodes without current collector and additives. It was enabled by optimizing the structures of Sn/C nanofibers. Manipulating the outward Sn diffusion was required for tunable Sn structures. The porosity of C nanofibers was regarded as a key parameter for this strategy and controlled by stabilization and gas-solid reactions between CO (g), CO₂ (g), and C nanofibers. According to pressure equilibriums, the preferential direction of the reactions was determined. We designed three calcination schemes to control the porosity. As it increased, Sn diffused out and agglomerated outside C nanofibers. Especially, the structure of the uniformly sized and well-dispersed small Sn was formed in the lowest porosity C nanofibers (ArNFs), which confined nucleation sites and prevented outward Sn diffusion. It was an ideal structure to minimize the stress originating from volumetric expansion and prevent pulverization of Sn. The electrochemical properties were evaluated as an anode of all-solid-state Li ion cell. ArNFs showed the best cycling performance with the capacity of 762 mAh/g and a coulombic efficiency over 99.5 % after 50 cycles. The novelty of our fabrication schemes for precise C porosity modulation and tunable Sn structures has been demonstrated by breaking through the limitations of Li-alloy based anodes. We believe that this work will open new synthetic routes to fabricate standard structures for general electrodes in future energy devices.

CHAPTER 7

Thermodynamic based Reaction Prediction of Multi-component Atomic System for Kinetic van-der Waals Solid Structure Control

7.1. Introduction

At nanoscale, contribution of surface energy and fast diffusion can generate many intriguing phenomena that may not be predicted in traditional approaches. In this chapter, we have proved how chemical potential of each species in multi-components system still can predict the phase behaviors even in a nanofiber. Tie-line calculated in ternary and quaternary phase diagram enables to predict which phases can evolve and exist stably in our Mo-S-C-O system. As a result, after identifying the specific region where the Boudouard reaction become favored, we successfully make macroscopically assembled two dimensional (2D) – molybdenum disulfide (MoS_2) crystals inside and on C nanofibers. Interestingly, because of interplay of ad-atom growth and gas phase inter-diffusion, vertical stacking and lateral growth of MoS_2 were controlled with astonishing precision and MoS_2 nanotube was directly converted from C based nanofibers.

Chapter 7: Thermodynamic based Reaction Prediction of Multi-component Atomic System for Kinetic van-der Waals Solid Structure Control

Structure control of MoS₂ is important to understand the reaction mechanism and broaden the applications because it can diversify and optimize intrinsic properties without doping.^[65-67] Few-layered MoS₂ fabrications are categorized into layer exfoliation from bulk MoS₂, chemical vapor deposition (CVD), and thermal decomposition of precursors.^[68,69] In reducing ambient, thiosalt precursors such as ammonium tetrathiomolybdate (ATTM, (NH₄)₂MoS₄), potassium tetrathiomolybdate (PTTM, K₂MoS₄) can form MoS₂.^[70,71] In the case of ATTM, decomposition products such as (NH₄)HMoS₄ of 160~173 °C, H₂MoS₄ of 173~180 °C, MoS₃ of 180~190 °C and Mo₂S₅ of 190~220 °C are generated during calcination.^[70] Although MoS₂ can be formed at the 425 °C with H₂, calcination at 800 °C is recommended for uniform phase formation.^[72] To form layer structured MoS₂ from single stacking unit, the nucleation and growth of MoS₂ ad-atoms are essential. Precisely controlled MoS₂ layers show remarkable performances in various applications such as field-effect transistor^[73], photovoltaics^[74], sensors^[75,76], piezoelectric energy generator^[77], Li, Na ion batteries^[78,79], electrochemical catalyst.^[80,81] Their performances are primarily affected by MoS₂ edge site exposure, crystal structures, and stacking sequence (2H, 1T). The hybridization of MoS₂ and C materials such as carbon nanotube (CNT), graphene, and nanofibers is favored in energy applications. They can provide large surface area and uniform dispersion by providing anchoring sites of activated C.^[82-84] Especially, C nanofibers show superior electrical conductivity and enable mass production.^[32] Until now, many metal dichalcogenides such as MoS₂, tungsten disulfide (WS₂) were embedded in C nanofibers and restricted to form single or few layered MoS₂ with confined structure.^[84-87] It still remains a challenge to tune MoS₂ structure and morphology.

Chapter 7: Thermodynamic based Reaction Prediction of Multi-component Atomic System for Kinetic van-der Waals Solid Structure Control

In this work, innovative methodology of MoS₂ assembly is suggested via “predictive synthesis”. It utilizes MoS₂ nanoplatelet from ATTM as a single stacking unit in C nanofibers. Our scheme proceeds the calcination of solid state Mo-S-C composites in gas state O₂. To selectively induce desired reactions, this study starts from thermodynamic calculation. It was proceeded by Ellingham diagram and Mo-S-C, Mo-S-O, Mo-C-O, MoS₂-C-O ternary phase diagrams. Concurrent modulation of MoS₂ structures and morphologies was enabled by C combustion based kinetic control.

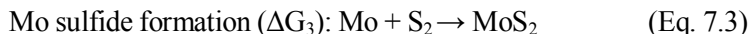
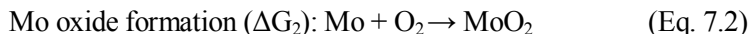
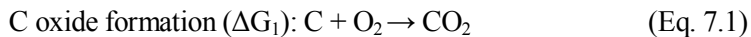
7.2. Thermodynamic calculation for redox control in Mo-S-C-O quaternary system

To apply the nanoscale Boudouard reaction to MoS₂ structure control, processing parameters (temperature, pressure) and material compositions should be determined before experiment. Atomic environments and possible reactions between them were shown in **Figure 7.1a**. ATTM and polyacrylonitrile (PAN, (C₃H₃N)_n) were used as a metal precursor (Mo, S source) and as a polymer matrix (C source) for electrospinning, respectively. O was supplied through O₂ gas; there was no O atom in the nanofiber. Elemental constituents in our system are Mo, S, and C in nanofibers, and O in the atmosphere. Possible redox reactions between them, and their related compounds, are Mo sulfidation (Mo_xS_y), Mo oxidation (Mo_xO_y), Mo carburization (Mo_xC_y), C sulfidation (C_xS_y), C oxidation (C_xO_y), and S oxidation (S_xO_y). In this work, Mo sulfidation + C oxidation should be induced without Mo oxidation, Mo carburization, C sulfidation, and S oxidation for MoS₂ assembly inside C nanofibers.

The thermodynamic feasibilities of those compounds and the processing parameters for the Mo-S-C-O redox control were considered in **Figure 7.1b**. In the Ellingham diagram, which displays the compound stability by chemical potentials, y-axis indicates Gibbs free energy (ΔG) and pO₂. The regions between the ΔG of the compounds and pO₂ can be matched by linking the extended line at a specific temperature.^[30] To apply the ΔG calculation to MoS₂ structure control, the calcination proceeded in a closed, O₂-gas-filled chamber.^[35] The pressure increased as the calcination proceeded due to gaseous decomposition products of the polymer matrix and increasing temperature. Hence, the pO₂ in this paper indicates the initial O₂

Chapter 7: Thermodynamic based Reaction Prediction of Multi-component Atomic System for Kinetic van-der Waals Solid Structure Control

pressure prior to the temperature increase in calcination. The representative reactions of Mo-S-C-O can be defined as follows.



Among the oxide, sulfide, and carbide Mo compounds, Mo oxide has the lowest ΔG . Although Mo sulfide is formed from ATTM, it can be oxidized due to the high oxidation tendency of Mo. Therefore, it is important to modulate the $p\text{O}_2$ to preclude Mo oxidation. At 800 °C (1073K), C shows the lowest ΔG of oxidation. C oxidation can be induced and Mo oxidation can be prevented by controlling the $p\text{O}_2$.^[2] Therefore, the redox reactions of Mo-S-C-O can be categorized according to the $p\text{O}_2$. At the lowest $p\text{O}_2$, such as under high vacuum ($<10^{-5}$ Torr) or Ar/H₂ gas, there is no oxidation of Mo and C ($\Delta G_1, \Delta G_2, \Delta G_3, \Delta G_4 > 0$). Mo undergoes sulfidation from ATTM and C undergoes reduction-based pyrolysis, which forms C residue in the absence of O. At the $p\text{O}_2$ between the ΔG of C oxidation and Mo oxidation ($\Delta G_1 < 0, \Delta G_2, \Delta G_3, \Delta G_4 > 0$), C is decomposed by oxidation-based combustion, which generates CO (g) and CO₂ (g), while maintaining MoS₂ formation. At the $p\text{O}_2$ above ΔG of Mo oxidation, both Mo and C are oxidized, and the Mo-S bonding in MoS₂ is broken by highly reactive O, which forms MoO₂ or MoO₃.

An important parameter extracted from Ellingham diagram is an equilibrium $p\text{O}_2$ which stabilizes corresponding phases. In our case, to stabilize MoS₂ (s), CO (g), and CO₂ (g) *via* nanoscale Boudouard reaction, $p\text{O}_2$ range between the ΔG of C oxidation

Chapter 7: Thermodynamic based Reaction Prediction of Multi-component Atomic System for Kinetic van-der Waals Solid Structure Control

and that of Mo oxidation should be derived. In **Figure 7.1b**, the dotted line was linked from the left axis point of $\Delta G=0$ to the point of $\Delta G=-396$ kJ/mol (C oxide formation at 800 °C).^[30] By extending this line to the right y-axis, the relevant pO_2 was obtained as 10^{-20} atm. However, there exists a gap between theoretical and experimental pO_2 values because the ΔG in the Ellingham diagram was established for bulk scale. Generally, in the case of nanoscale, a surface energy term should be added to the ΔG , which induces a shift of the processing parameters.^[88] In our previous work, C nanofibers demonstrated a ΔG shift of -90.92 kJ/mol.^[2] By considering this pressure shift in our system, 3.75×10^{-5} atm (0.0285 Torr) was derived as the equilibrium pressure for C oxidation. Therefore, we established an initial pressure range for the experiment from 0.1 to 0.4 Torr in our closed system.

Next, thermodynamic considerations are based on the phase diagram. After fixing the pressure at a temperature of 800 °C between 0.1 and 0.4 Torr from the Ellingham diagram, we constructed ternary phase diagrams of Mo-S-C, Mo-S-O, Mo-C-O, and MoS_2 -C-O (**Figure 7.2**). They were extracted from the Mo-S-C-O quaternary components. The phase diagram offers a framework to predict the equilibrium phases at specific conditions. In the ternary phase diagram, the elemental phases at the corner of triangle indicate stable states. Linking the tie-line indicates stable compound formation. Based on the Gibbs phase rule, tie-lines should not overlap.^[35] According to the aspects of tie-line linkage, ternary phase diagrams can be classified as no-phase dominant (compound-compound) or specific phase dominant (compound-element).^[35,36] We calculated phase diagrams from a thermochemical database program (FactsageTM software).^[89] In this calculation, the equilibrium pressure was established as a variable, and its values were 10^{-5} , 0.1, 0.2, 0.3, 0.4, 0.76, 4, and 760 Torr. With the exception of high vacuum (10^{-5} Torr) and air (760 Torr), common

Chapter 7: Thermodynamic based Reaction Prediction of Multi-component Atomic System for Kinetic van-der Waals Solid Structure Control

phase diagrams with similar compounds and tie-lines were constructed within the pressure range of 0.1~4 Torr.

The specific Mo-S-C-O mole fraction to form MoS₂ and gaseous C oxide while preventing Mo oxide formation was derived from the calculated ternary phase diagrams. First, the Mo-S-C ternary diagram was used to predict Mo, S, C composition in solid state electrospun nanofibers (**Figure 7.2a**). Mo₂C, MoC, Mo₂S₃, MoS₂, C₅S₁₁, and CS₇ were expected to be formed, with MoS₂ dominating the phase diagram. From the starting point of a 0.2Mo-0.8S molar ratio in ATTM, a dotted line linked with C (left corner) shows the possible composition of ATTM and PAN. The C mole fraction should exceed 0.15 to induce MoS₂+CS₂+C (pink area). Additionally, for uniform nanofibers, the electrospinning solution should have a sufficient viscosity, which depends on the amounts and molecular weight of PAN.^[90] According to all of these considerations, the mole fraction was established as 0.075Mo-0.302S-0.623C, which was achieved by the combination of 1.4 g of ATTM and 0.7855 g of PAN.

Second, the Mo-S-O and Mo-C-O phase diagrams allowed for the determination of the relative composition between O and 0.075Mo-0.302S-0.623C. In Mo-S-O system (**Figure 7.2b**), MoO₂, MoO₃, Mo₂S₃, MoS₂, and SO₂ were expected to be formed. In Mo-C-O system (**Figure 7.2c**), MoO₂, MoO₃, Mo₂₇C₁₃, Mo₆₇C₃₃, CO₂, C₄₃O₅₇, and CO were expected to be formed. Unlike the MoS₂-dominant Mo-S-C phase diagram, the Mo-C-O diagram was no-phase dominant. When the chamber (volume: 7854 cm³) was filled with only O₂ gas to 0.1~0.4 Torr, the amount of O₂ was calculated to be 1.2~4.7×10⁻⁵ mol. Based on this value, the mole ratio between Mo, S, C, and O was calculated to prevent Mo oxide formation. In the Mo-S-O phase diagram (**Figure 7.2b**), the dotted line linked with the point of 0.2 Mo-0.8 S molar ratio and O (left corner) shows the possible material composition. To form MoS₂+SO₂+S (pink area),

Chapter 7: Thermodynamic based Reaction Prediction of Multi-component Atomic System for Kinetic van-der Waals Solid Structure Control

the O mole fraction should be lower than 0.45. In the Mo-C-O phase diagram (**Figure 7.2c**), the dotted line linked with the point of 0.108 Mo-0.892 C molar ratio and O (left corner) also indicates that the O mole fraction should be lower than 0.45 for MoC+CO+C (pink area). From this theoretical prediction, we determined that the amount of ATTM+PAN nanofibers should be 30 mg in the calcination process. To confirm the material compositions obtained from Mo-S-C, Mo-S-O, and Mo-C-O ternary phase diagrams, the MoS₂-C-O phase diagram (**Figure 7.2d**) was analyzed. It was constructed by linking the MoS₂-related tie-lines in the Mo-S-C-O quaternary system with calculations in FactsageTM. Our conditions were confirmed to be in the region of MoS₂+CO+C (pink area, **Table 7.1**).

The predictions made from phase diagrams can be further validated by **Figure 7.3**. They show which mole fractions of solid and gas phase can be stable as a function of pO₂. Figure 1d is a phase calculation of 0.075Mo-0.302S-0.623C depending on the O₂ amount with the assumption of infinite calcination time. A constant amount of MoS₂ formed stably until the O₂ value reached 0.77 mol. When it exceeded 0.77 mol, the formation of MoS₂ decreased and MoO₂ started to form. Simultaneously, solid state C started to decompose with the presence of O₂ until it reached 0.3 mol. These values can be used as guidelines to set parameters not to exceed critical points. Figure 1e shows the calculations for gaseous products. In primary region, most products are CO, which originates from C combustion. Carbon disulfide (CS₂) decreases as CO forms. Compared to the C amount in Fig. 1d, CO formation is promoted by combustion of solid C until O₂ reaches 0.3 mol. As the O₂ amount increases above 0.3 mol, the production of CO is reduced and CO₂ starts to form. This relationship is related to both carbothermic reduction, which prevents Mo oxidation, and the Boudouard

Chapter 7: Thermodynamic based Reaction Prediction of Multi-component Atomic System for Kinetic van-der Waals Solid Structure Control

reaction. As calcination proceeds, the chamber pressure increases and the Boudouard reaction proceeds ($C+CO_2\leftarrow 2CO$) in reverse equilibrium direction.

Figure 7.4 denotes how this thermodynamic approach affects the MoS_2 rational design. Unlike the calcination at low pO_2 , which produces randomly-distributed MoS_2 single layers, the ambient calcination of O_2 changes all surrounding conditions while maintaining MoS_2 formation. Detailed aspects of structural evolution and related mechanisms will be discussed in following section.

Chapter 7: Thermodynamic based Reaction Prediction of Multi-component Atomic System for Kinetic van-der Waals Solid Structure Control

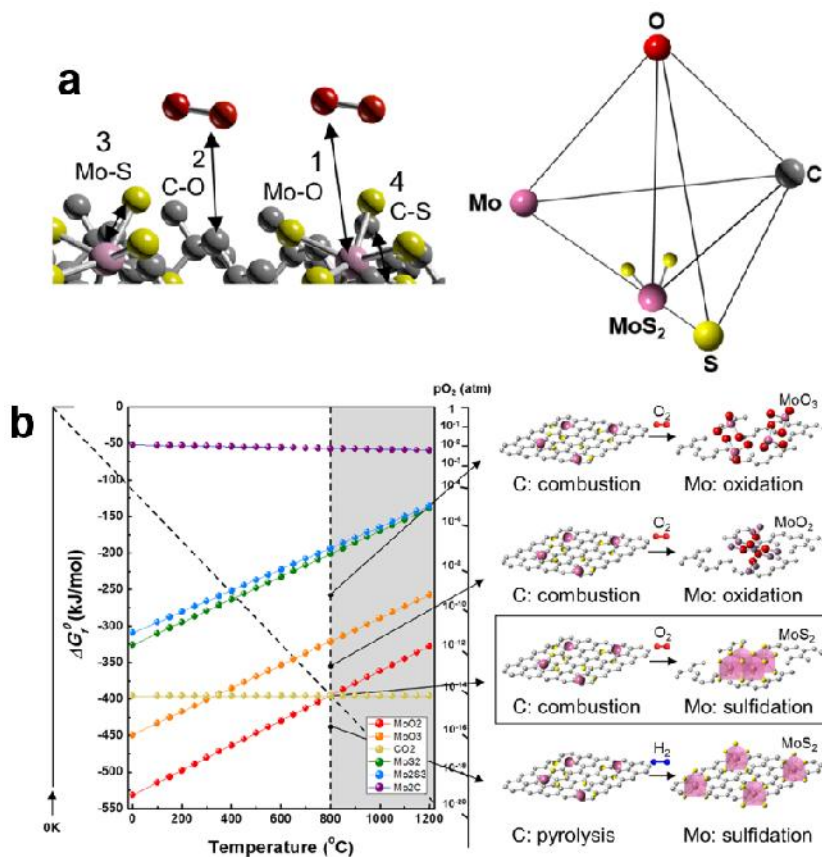


Figure 7.1. Thermodynamic Strategy to induce processing parameter and material composition to control MoS₂ formation. **(a)** Atomic system of Mo, S, C in nanofibers and O in ambient. **(b)** Ellingham diagram which provides Gibbs free energy of reactions between Mo, C and S, O.

Chapter 7: Thermodynamic based Reaction Prediction of Multi-component Atomic System for Kinetic van-der Waals Solid Structure Control

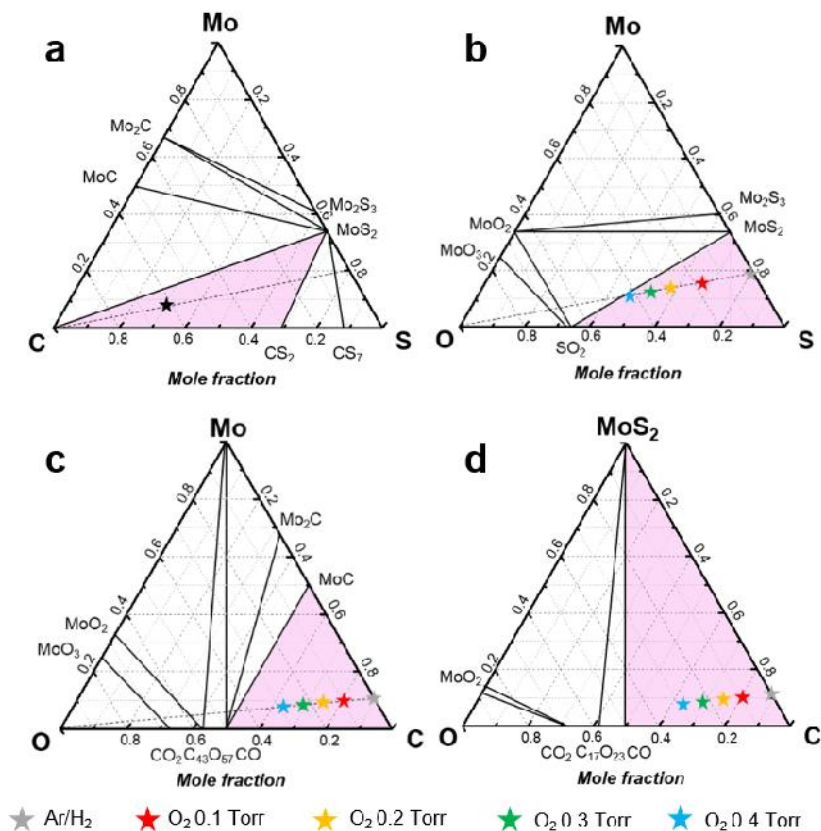


Figure 7.2. Ternary phase diagrams of nanofiber components to predict phase formation in the components of Mo, S, O, and C. **(a)** Mo-S-C, **(b)** Mo-S-O, **(c)** Mo-C-O, and **(d)** MoS_2 -C-O at the calcination condition of 800 °C, 0.1~0.4 Torr.

Chapter 7: Thermodynamic based Reaction Prediction of Multi-component Atomic System for Kinetic van-der Waals Solid Structure Control

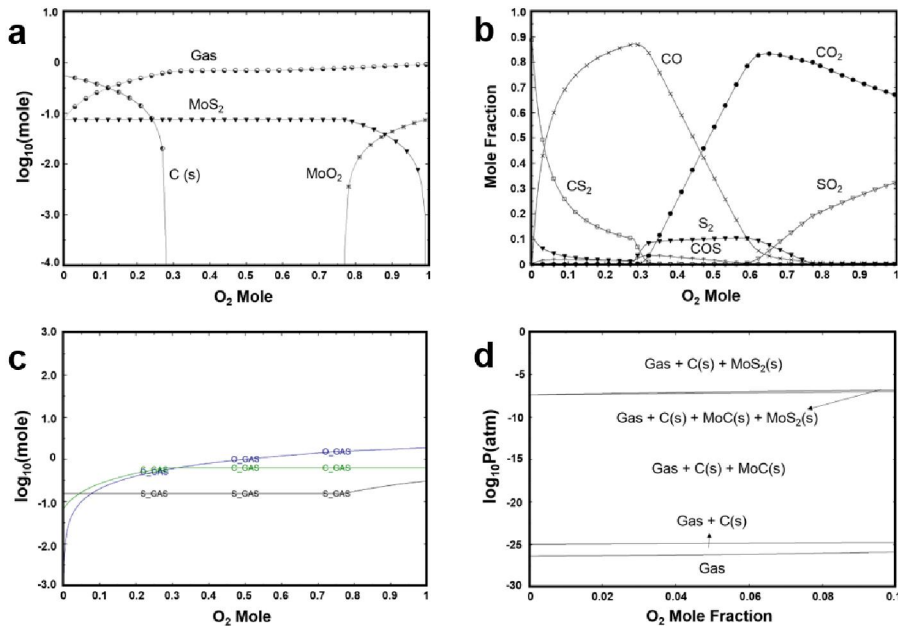


Figure 7.3. FactsageTM-calculated thermodynamic behavior of gas formation and phase transformation. **(a)** Evolution of thermodynamically stable phases calculated according to the O_2 moles in a closed chamber system and related **(b)** gas decomposition products. **(c)** The progress of gas product amounts in the aspects of C, O, S formed in accordance with the number of O_2 moles. **(d)** Phase diagram according to the O_2 mole fraction and total chamber pressure from 0 to 10^{-30} atm. The minimum pressure is 6.6×10^{-9} atm and the pressure range for selective oxidation ranged from 1.3×10^{-4} to 5.3×10^{-4} atm.

Chapter 7: Thermodynamic based Reaction Prediction of Multi-component Atomic System for Kinetic van-der Waals Solid Structure Control

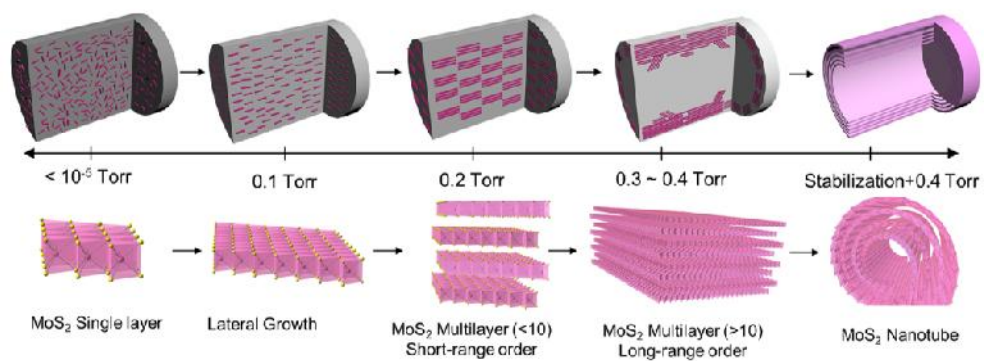


Figure 7.4. Structure evolution schemes of MoS₂ according to pressure, which affects the degree of selective C oxidation in MoS₂/C nanofibers.

7.3. Validation of molybdenum sulfidation and carbon oxidation

To verify the processing parameters and material compositions derived in the Ellingham diagram and the phase diagram, we investigated the chemical states of MoS₂/C nanofibers after calcination. The X-ray diffraction (XRD) analysis in **Figure 7.5a** reveals that MoS₂ is well-formed inside C nanofibers. Calcination at the pO₂ of 0.1~0.4 Torr induced an MoS₂ phase (hexagonal, JCPDS 00-006-0097) without Mo oxidation (MoO₂, MoO₃). As pressure increases, the relative peak intensity of MoS₂ (002) plane increases, revealing that MoS₂ layers stacked toward the (002) plane. With the confirmation of MoS₂ formation, the occurrence of C combustion should be investigated to determine the Mo sulfidation and C oxidation. The quantitative weight percent of Mo and C were analyzed using X-ray photoelectron spectroscopy (XPS). With the assumption of a constant amount of Mo in MoS₂/C nanofibers, the degree of C decomposition can be analyzed according to the pO₂ in calcination (**Figure 7.5b**). Unlike pyrolysis, combustion lowers the relative C weight percent (wt.%) due to the generation of CO (g) and CO₂ (g). By comparing the C wt.% between atmospheres of Ar/H₂ and O₂, the C decomposition type can be determined. Ar/H₂ calcination showed 68.3 wt.% C contents, and pO₂ 0.1 Torr calcination showed 57.69 wt.%. As the O₂ amount increased to 0.4 Torr, the wt.% decreased to 30.87 wt.%. Therefore, C decomposition proceeded by combustion, and its degree could be precisely modulated by the amount of O₂.

These Mo sulfidations and C oxidations can also be confirmed using Raman analysis (**Figure 7.5c**). The chemical status of MoS₂ and C can be divided and interpreted independently by the extent of the Raman shift. The E_{2g} peak at 377.5 cm⁻¹

Chapter 7: Thermodynamic based Reaction Prediction of Multi-component Atomic System for Kinetic van-der Waals Solid Structure Control

(in-plane vibration) and the A_{1g} peak at 403.3 cm^{-1} (out-of-plane vibration) belong to MoS_2 .^[91] The D peak at 1360 cm^{-1} (breathing mode of sp^2 atoms (rings)) and the G peak at 1600 cm^{-1} (stretching mode of sp^2 atoms (rings and chain)) belong to C.^[92] As the amount of O_2 increases, the E_{2g} and A_{1g} peak intensities of MoS_2 increases and the D and G peak intensities of C decreases. This result agrees with XRD and XPS results in **Figure 7.5a, b**. As shown by the difference in the intensities of the E_{2g} and A_{1g} peaks, highly-stacked MoS_2 favors the out-of-plane vibration mode. The extent of MoS_2 layer stacking therefore increases as the degree of C decomposition increases.

To investigate the effect of combustion on MoS_2/C nanofibers, a Brunauer–Emmett–Teller (BET) analysis was performed (**Figure 7.6**) by measuring N_2 gas adsorption and desorption at an isotherm of 77K. The BET specific surface area (SSA), pore volume, and pore size of the MoS_2/C nanofibers can be derived from this analysis. As the amount of O_2 increases, total pore volume increases from 0.0242 to $0.0523\text{ cm}^3/\text{g}$. In pore size distribution of MP plot (**Figure 7.6b**) and in the Barrett-Joyner-Halenda (BJH) plot (**Figure 7.6c**), the portion of micro/meso-pores increases at higher amounts of O_2 . Higher degrees of C combustion generate more pores in the nanofibers, which can be determined by the associated increase in BET SSA, pore volume, and micropore ratio.

The oxidation numbers of Mo and S were assessed by XPS to investigate the chemical status of MoS_2 more in detail. The Mo 2d spectra (**Figure 7.7a**) is composed of Mo $2d_{3/2}$ approximately 232 eV (red) and Mo $2d_{5/2}$ approximately 229 eV (blue). They represent the oxidation status of Mo^{4+} which denotes the formation of 2H-MoS_2 . The split peaks at slightly lower binding energies than those of Mo^{4+} shows the structurally distorted 1T phase.^[93,94] There is no significant difference in the peak intensity of Mo^{5+} at 234 eV (orange) and Mo^{6+} at 236 eV (yellow) for different O_2

Chapter 7: Thermodynamic based Reaction Prediction of Multi-component Atomic System for Kinetic van-der Waals Solid Structure Control

amounts. This result means that there is no excess oxidation of Mo related to the reaction between Mo and O. The peaks at 227 eV (green) are related to S 2s, which represents multiple chemical states of S.^[95] The S 2p XPS spectra (**Figure 7.7b**), which represent the oxidation status of S₂, is composed of S 2p_{1/2} approximately 163 eV and S 2p_{3/2} approximately 162 eV. As the O₂ amount increases, it induces MoS₂ layer stacking, and the relative peak intensity of S 2p_{1/2} reduces below than that of S 2p_{3/2}. The decrease of the S 2p_{1/2} value denotes the decreasing amount of bridging and terminal S²⁻ ligands.^[94,95] These results reveal that the nanoscale Boudouard reaction can control the chemical states of MoS₂ by the interplay of reduction and oxidation with gaseous O₂ molecules.

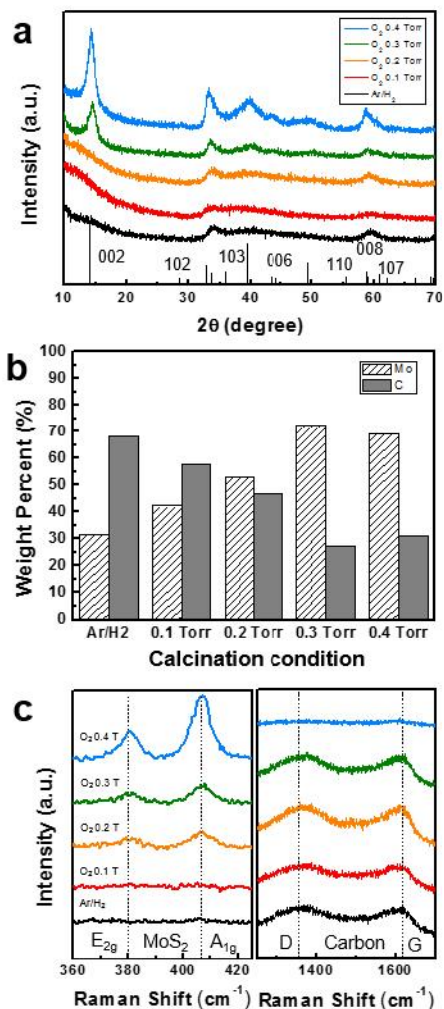


Figure 7.5. Analysis to confirm redox control of Mo-S-C-O and reaction inducement of Mo sulfidation and C oxidation. **(a)** XRD and **(b)** XPS analysis to determine the pressure range of selective oxidation. Raman analysis which shows the increasing **(c)** stacking number of MoS₂ with decreasing C contents in nanofibers.

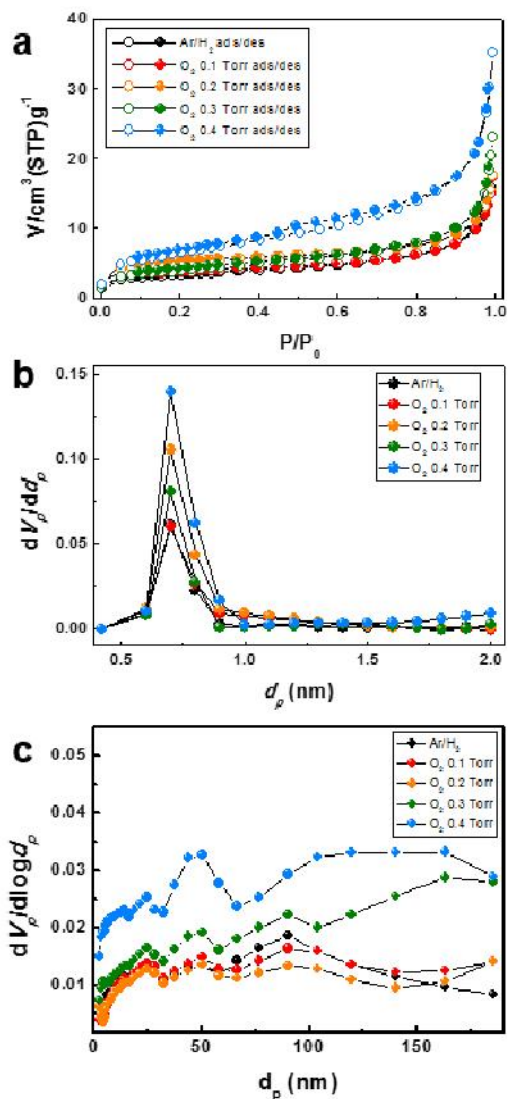


Figure 7.6. (a) Brunauer–Emmett–Teller (BET) specific surface areas of the MoS₂/C nanofibers according to the calcination conditions. (b) Comparison of the micropore size distribution between the MoS₂/C nanofibers using MP plot. (c) Mesopore size distribution of MoS₂/C nanofibers. Higher amounts of O₂ induced porosity in nanofiber structures after calcination in the Barrett-Joyner-Halenda (BJH) plot.

Chapter 7: Thermodynamic based Reaction Prediction of Multi-component Atomic System for Kinetic van-der Waals Solid Structure Control

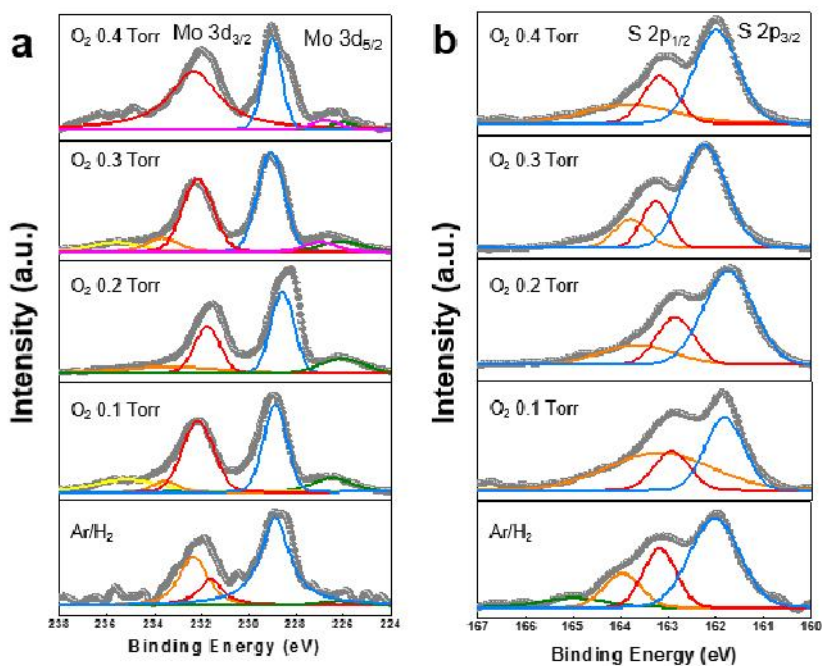


Figure 7.7. XPS analysis for investigating the chemical status of **(a)** Mo and **(b)** S.

7.4. MoS₂ rational design according to the thermodynamic-driven processing parameters

Figure 7.8 shows the structures of MoS₂/C nanofibers and MoS₂ nanotubes as analyzed using a field-emission scanning electron microscope (FE-SEM) and using a transmission electron microscope (TEM). It directly reveals how our thermodynamic-based synthesis scheme affects the kinetics of MoS₂ formation. They were fabricated at 800 °C, 5 h after electrospinning of ATTM+PAN nanofibers. In calcination under Ar/H₂ gas (**Figure 7.8a**), single-layered MoS₂ nanoplatelets formed. They were randomly distributed within nanofibers, which showed the highest C wt.% and the lowest porosity due to pyrolysis. Figures 3b-e show the MoS₂/C nanofibers formed by C combustion. In the presence of O₂, the MoS₂ structures and morphologies varied depending on the degree of C decomposition. At a pO₂ of 0.1 Torr (**Figure 7.8b**), the surface of the nanofibers and the structure of individual MoS₂ layers were similar to those acquired *via* Ar/H₂ calcination. However, they began to be aligned along the axis of nanofibers. Additionally, the layer length increased as the stacking degree was maintained. As the pressure increased to pO₂ 0.2 Torr (**Figure 7.8c**), both the length and stacking number of MoS₂ increased, within a rough nanofiber surface. Furthermore, all MoS₂ layers demonstrated a parallel alignment at the center of the nanofibers. At a pO₂ of 0.3 Torr (**Figure 7.8d**), unique MoS₂ structures and morphologies were produced. With the expected structural evolution of MoS₂ length and the increase in the stacking number, they formed bundles of 2D van der Waals solids and bent into an octahedron morphology. Additionally, the MoS₂ bundles began to be aligned along the nanofiber near the surface. At a pO₂ of 0.4 Torr (**Figure 7.8e**), this trend intensified. Most MoS₂ layers were displaced at the surface of the

Chapter 7: Thermodynamic based Reaction Prediction of Multi-component Atomic System for Kinetic van-der Waals Solid Structure Control

nanofibers, with a maximum stacking number of 25 and a length of over 100 nm. In the case of the nanotubes, air stabilization at 280 °C occurred before calcination, accelerating C decomposition. In thermogravimetric analysis (TGA), an exothermic peak at 250~300 °C was observed, denoting the cyclization of the nitrile group in PAN (**Figure 7.9**). Depending on the ambient conditions, the decomposition aspects of ATTM and PAN differ significantly, which can be intuitively explained by TGA and DSC. In air (high pO_2), metal ions in ATTM oxidize and PAN is decomposed by combustion. The calcination product is Mo-oxide grain nanofibers without residual C. However, in N_2 (low pO_2), metal ions are reduced and PAN is decomposed by pyrolysis, and carburized residual C forms in the shape of nanofibers. In TGA, an exothermic peak at 250~300 °C was observed, denoting the cyclization of the nitrile group in PAN. When the stabilization preceded calcination at pO_2 of 0.4 Torr, hollow MoS_2 nanotubes were formed (**Figure 7.8f**). The MoS_2 length and stacking number in the shell areas were consistent and aligned in the direction of the nanotube axis.

Figure 7.10 shows the detailed structure of nanotube-shaped MoS_2 . The production of fullerene-like MoS_2 nanotubes was first reported by the reaction between MoO_{3-x} and H_2S .^[96] However, most of the nanotubes showed limitations in their aspect ratios, yield, uniformity, dispersion, and crystallinity.^[97,98] In this work, high-aspect-ratio MoS_2 nanotubes were produced by the assembly of MoS_2 stacking unit as a motif (**Figure 7.10a**). The aspect ratio of nanotubes was higher than 100, and the MoS_2 shell was uniformly distributed at the surface. **Figure 7.10b** is a plane view of the inner section. To determine the exact phase of nanotubes, XRD and TEM analyses were performed. The XRD (**Figure 7.11**) shows the simultaneous formation of MoS_2 (JCPDS 00-006-0097) and MoO_2 (JCPDS 00-032-0671). This result is related to the higher degree of C decomposition by the stabilization. As expected from the

Chapter 7: Thermodynamic based Reaction Prediction of Multi-component Atomic System for Kinetic van-der Waals Solid Structure Control

Ellingham diagram, this result was caused by the O₂-gas-induced oxidation of C and partial Mo ions related with C over-consumption. To determine the precise distribution of MoS₂ and MoO₂, we analyzed diffraction patterns using fast Fourier transform (FFT) and energy dispersive spectroscopy (EDS) at the nanotube sites.

Figure 7.10c shows the shell structure of nanotubes, observed using high-resolution, Cs-corrected TEM; in it, we can see the atomic arrays of S-Mo-S. The d-spacing of 0.61 nm and the FFT revealed the existence of MoS₂. In contrast, the TEM image and FFT of the inside of the nanotube (**Figure 7.10d**) shows the existence of MoO₂. The inside showed a higher O atomic percent than did the shell of the nanotube (**Figure 7.11**). In **Figure 7.10e**, the atomic compositions of the shells of the nanotubes were determined as Mo and S using EDS mapping.

Chapter 7: Thermodynamic based Reaction Prediction of Multi-component Atomic System for Kinetic van-der Waals Solid Structure Control

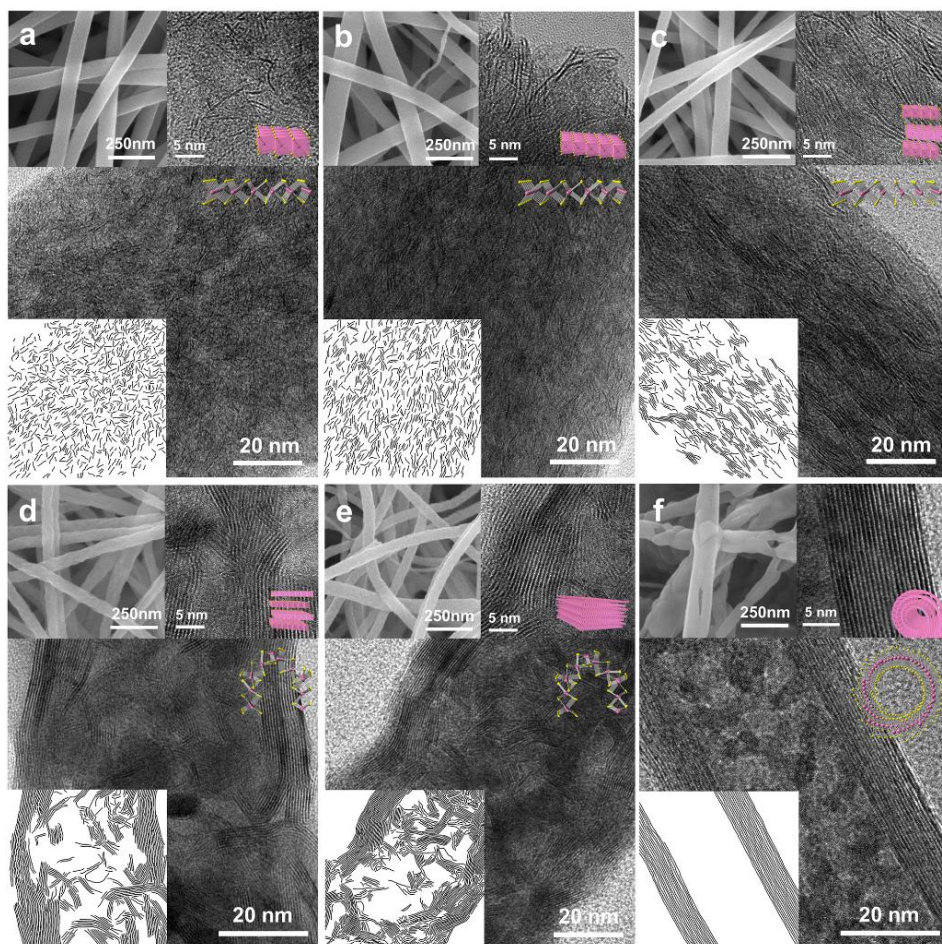


Figure 7.8. FE-SEM, TEM images and reproduced images of MoS₂/C nanofibers for structure analysis. FE-SEM images illustrate the surfaces of nanofibers and nanotubes. TEM images illustrate the length, stacking number, alignment, and distribution of MoS₂ inside nanofibers under conditions of (a) Ar/H₂ gas, (b) pO₂ 0.1 Torr, (c) 0.2 Torr, (d) 0.3 Torr, (e) 0.4 Torr, (f) Stabilization + pO₂ 0.4 Torr calcination.

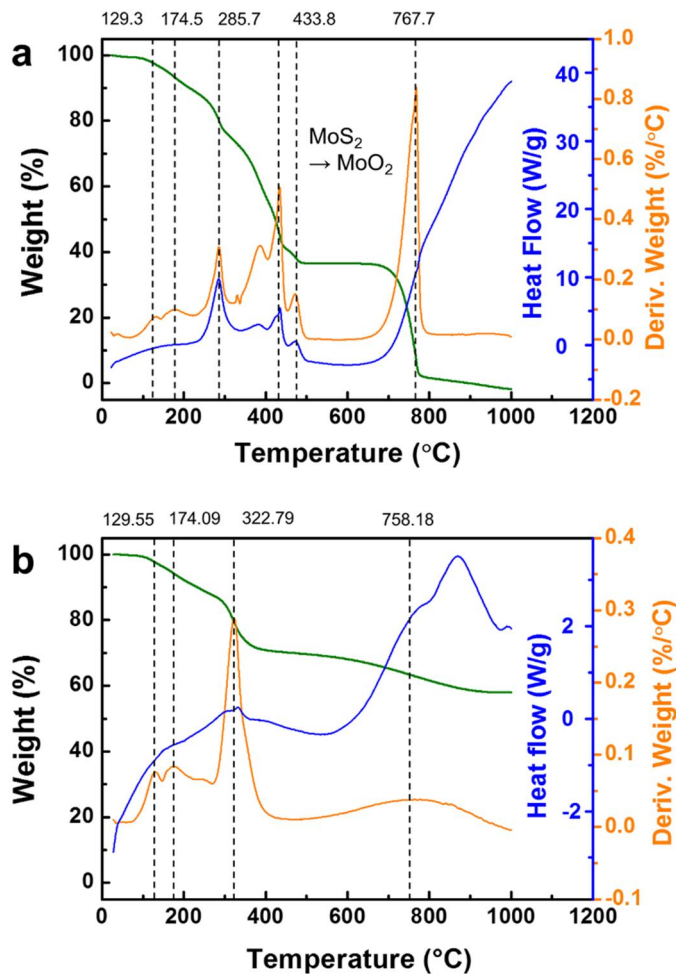


Figure 7.9. Thermogravimetric analysis (TGA) and differential scanning calorimetry (DSC) of electrospun ATTM+PAN nanofibers. These compare the extent of decomposition by full oxidation and full reduction under (a) air for combustion and (b) N_2 for pyrolysis.

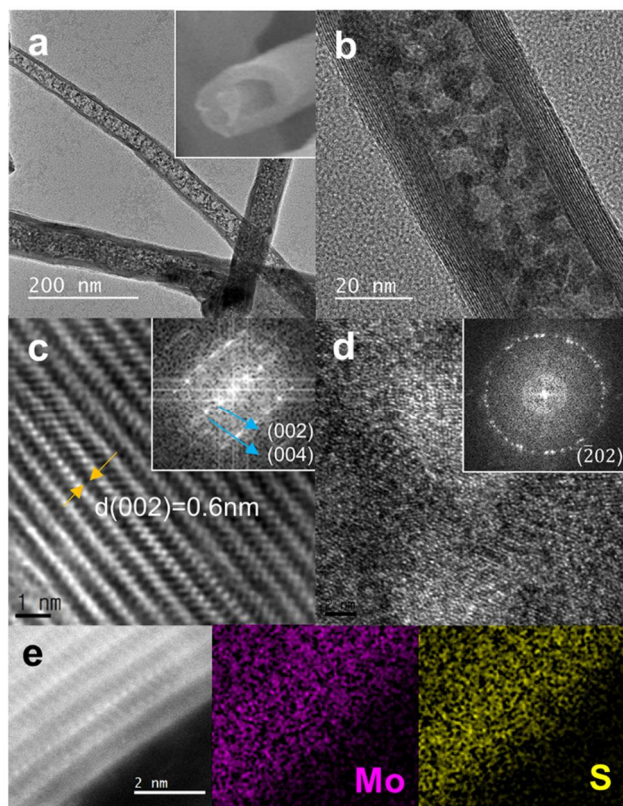


Figure 7.10. MoS₂ nanotubes with high aspect ratios formed by a stable calcination process. TEM images with (a) low magnification to show overall morphology and (b) high magnification to show MoS₂ distribution. Cs-corrected TEM analysis provides (c) high resolution image and FFT analysis (inlet) of MoS₂ atomic array at the shell in the (002) direction. (d) Bright field image and FFT analysis (inlet) of MoO₂ phase at the inner part and (e) HAADF and EDS mapping of the shell of the nanotubes.

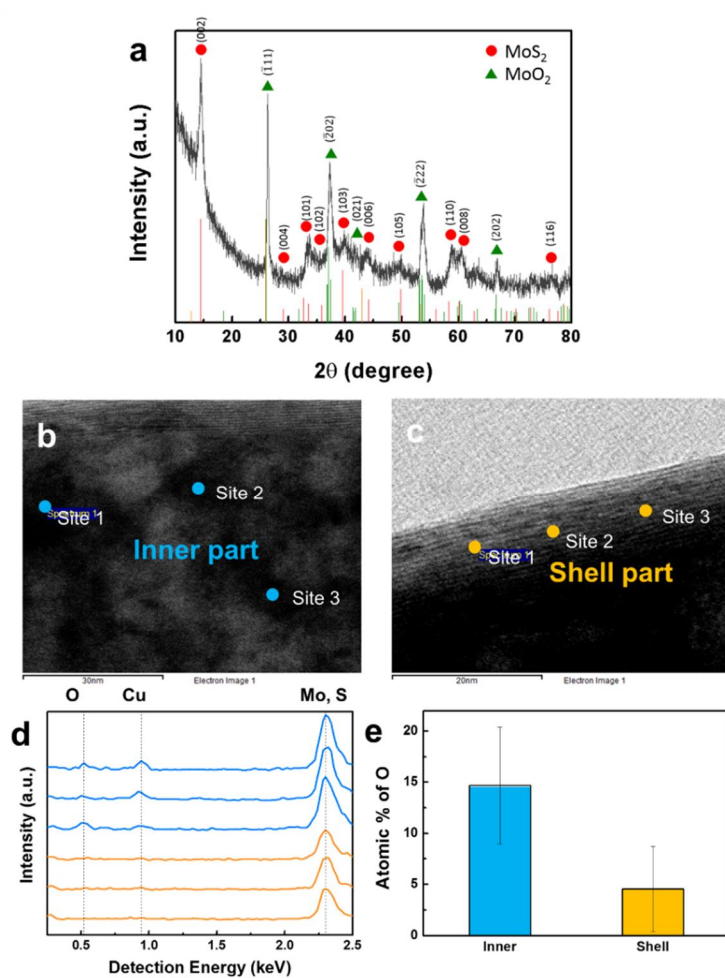


Figure 7.11. Phase investigation of MoS₂ nanotubes. **(a)** XRD analysis after stabilization + pO₂ 0.4 Torr calcination. TEM EDS analysis of **(b)** the inner part and **(c)** the shell part to investigate the distribution of MoS₂ and MoO₂. **(d)** Mo, S, O quantitative analysis for each of the sites. Cu has been detected due to the presence of the TEM grid. **(e)** Comparison of O atomic % between inner and shell parts. The inside showed a higher O atomic percent than did the shell of the nanotube. The shell part contains MoS₂ and inner part of the nanotubes contains MoO₂.

7.5. Kinetics of MoS₂ layer formation

For a comprehensive study of MoS₂ formation kinetics, statistical analysis of MoS₂ length and stacking number was performed, as shown in **Figure 7.12**. The pressure dependence at a fixed calcination time of 5 h was analyzed according to MoS₂ length and stacking number (**Figure 7.12a-c**). Under Ar/H₂ conditions, the average length and stacking number were 3.14 nm and 1.1, respectively. As the pressure increased from pO₂ of 0.1 to that of 0.4 Torr, these values increased from 3.90 nm and 1.29, respectively, to 8.61 nm and 4.60, respectively (**Figure 7.12b, c**). Finally, a maximum layer length and stacking number of 33.01 nm and 16.5, respectively, were obtained at the stabilization+0.4 Torr condition. The standard deviation of the length and stacking number was lowest in this MoS₂ nanotube. The MoS₂ layer prefers lateral growth (length) to vertical stacking (stacking number).

Next, the time dependence was evaluated at 1, 5, and 10 h at a fixed pressure of O₂ of 0.3 and 0.4 Torr (**Figure 7.12d-f**). As the time increased, both the length and stacking number also increased, and MoS₂ layers in C nanofiber showed an outward distribution, similar to the pressure control results (**Figure 7.13**). When comparing MoS₂ length and stacking number in the pO₂ of 0.3 Torr, 1 h and pO₂ of 0.2 Torr, 5 h conditions, they showed a similar degree of lateral growth and vertical stacking. This result reveals that the same structure can be formed faster at higher O₂ amounts, and the related kinetics are dominated by pO₂. When comparing the length and stacking number for the pO₂ of 0.3 and pO₂ of 0.4 Torr conditions (**Figure 7.12e, f**), the length was the same but the stacking number was higher in the pO₂ of 0.4 Torr condition. This result indicates that the increase in the lateral growth rate is saturated at pO₂ of 0.3 Torr and that it does not increase further in the pO₂ of 0.4 Torr condition. However,

Chapter 7: Thermodynamic based Reaction Prediction of Multi-component Atomic System for Kinetic van-der Waals Solid Structure Control

the growth rate of vertical stacking in pO_2 of 0.4 Torr was higher than that of pO_2 0.3 Torr, demonstrating lateral growth preference.

In this work, not only the structure but also the morphology of MoS_2 has been modulated. Nanoplatelets were formed in the range of $pO_2 = 0.1\sim 0.2$ Torr. As the pressure increases to the range of $pO_2 = 0.3\sim 0.4$ Torr, the curved shape of an octahedron formed inside the nanofibers (**Figure 7.12d, e**). Finally, hollow MoS_2 nanotubes formed under the stabilization+ pO_2 of 0.4 Torr condition (**Figure 7.12f**). In previous research, stable MoS_2 morphology was theoretically predicted by an energy equilibrium calculation.^[99–101] According to the number of MoS_2 atoms (N) at nucleation, the total energy of MoS_2 was calculated. The result indicated that MoS_2 morphology is stable in the order of ‘nanoplatelet \rightarrow octahedron \rightarrow hollow fullerene’ with increasing N. Our experimental results are well-matched with the theoretically-expected morphologies. Therefore, it can be inferred that the degree of C decomposition has an intimate relationship with number of MoS_2 molecules in the nucleation process.

Based on this principle, the structure formation process can be explained by the nucleation and growth of MoS_2 molecules (**Figure 7.14**). As more C is decomposed by increasing O_2 pressure, the migration of MoS_2 molecules becomes easier and the adjacent number of nuclei increases. Anisotropic growth behavior is explained by the difference in activation energy according to the heterogeneous nucleation sites. The MoS_2 basal plane is a weak interacting site and has low chemical reactivity. In contrast, the edge site is a strong interacting site and shows high chemical reactivity.^[102] Therefore, lateral growth induced by heterogeneous nucleation at the edge site proceeds faster than vertical growth.^[102,103] The MoS_2 distribution increases toward the surface of nanofibers as pressure and time increase, which can be

Chapter 7: Thermodynamic based Reaction Prediction of Multi-component Atomic System for Kinetic van-der Waals Solid Structure Control

explained by the complex interplay between gas molecules and the precursor. These preferred outward distributions and alignments of MoS₂ are related to CO and CO₂ formation and their migration toward the outside. Due to the formation of gaseous products and their outward migration, the creation of MoS₂ is promoted at the outer part of nanofibers.

Through the redox-mediated nanoscale Boudouard reaction, diversified MoS₂ structures (length, stacking number, alignment, and distribution) and morphologies (nanoplatelet, octahedron, and hollow nanotube) could be derived from the same starting material and controlled precisely for the first time. We think that this study provides an insight into not only MoS₂ structure control but also the design of nanomaterial synthesis. The importance of quantitative understanding of the behavior of atomic multi-components is increasing. Our methodology can provide core principles to understand the effect of spontaneous atomic reactions and migration on the phase, morphology, size, arrangement, and distribution of products in nanomaterials.

Chapter 7: Thermodynamic based Reaction Prediction of Multi-component Atomic System for Kinetic van-der Waals Solid Structure Control

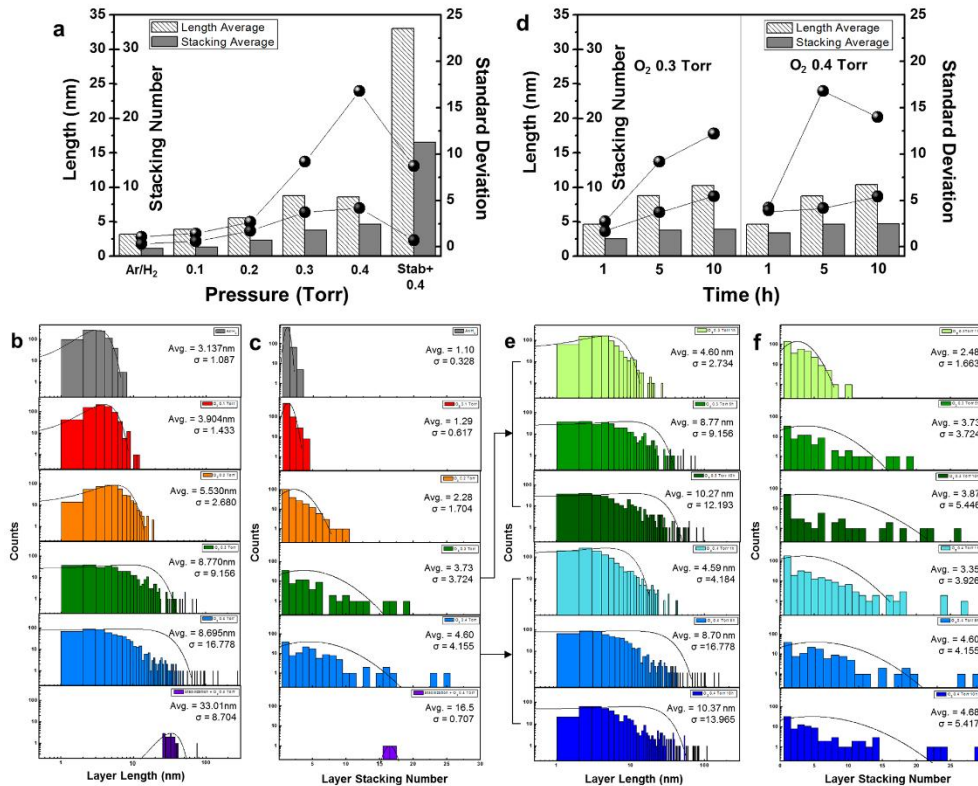


Figure 7.12. Statistical analysis which denotes the quantitative aspects of structure evolution of MoS₂. Average and standard deviation of MoS₂ structure information investigated by TEM images according to the (a) pressure (Ar/H₂ gas, pO₂ 0.1, 0.2, 0.3, 0.4 Torr, and stabilization + pO₂ 0.4 Torr) of (b) layer length, (c) stacking number and (d) isothermal time (1, 5, 10 h at pO₂ 0.3 and 0.4 Torr) of (e) layer length and (f) stacking number. Comparison of the growth modes between the lateral (length) and vertical (stacking number) directions during self-assembly of MoS₂ inside C nanofibers according to the pressure and time.

Chapter 7: Thermodynamic based Reaction Prediction of Multi-component Atomic System for Kinetic van-der Waals Solid Structure Control

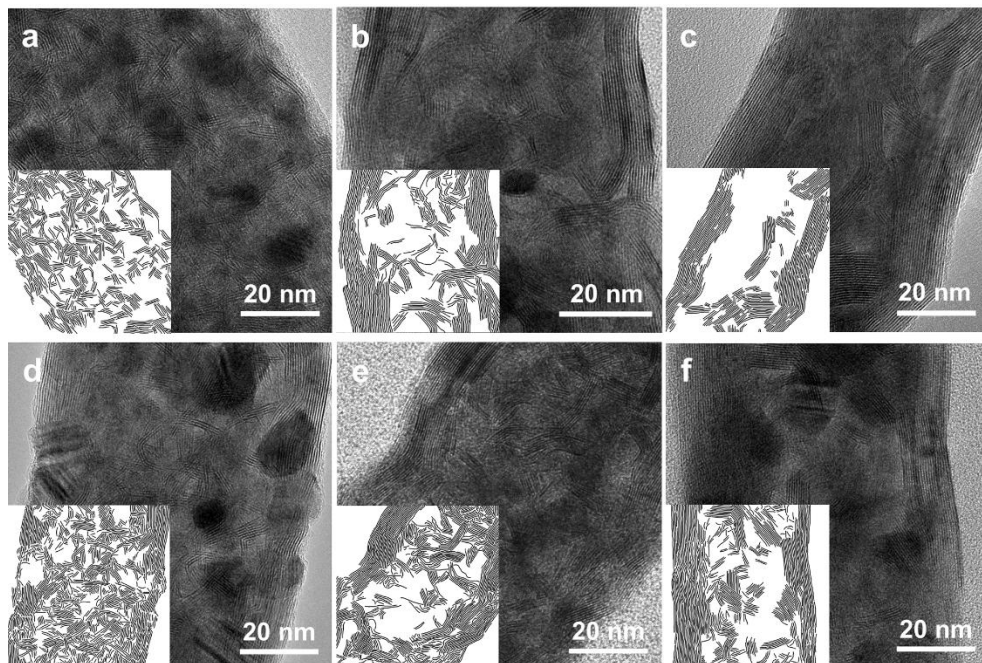


Figure 7.13. TEM images and reproduced images of MoS₂ in nanofibers for structure statistical analysis. The calcination time was varied at constant pressures of 0.3 and 0.4 Torr at a temperature of 800 °C. **(a)** 0.3 Torr 1 h, **(b)** 0.3 Torr 5 h, **(c)** 0.3 Torr 10 h, and **(d)** 0.4 Torr 1 h, **(e)** 0.4 Torr 5 h, **(f)** 0.4 Torr 10 h. As the isothermal time increased, MoS₂ layers are increasingly distributed near the surface of the nanofibers and aligned parallel to them.

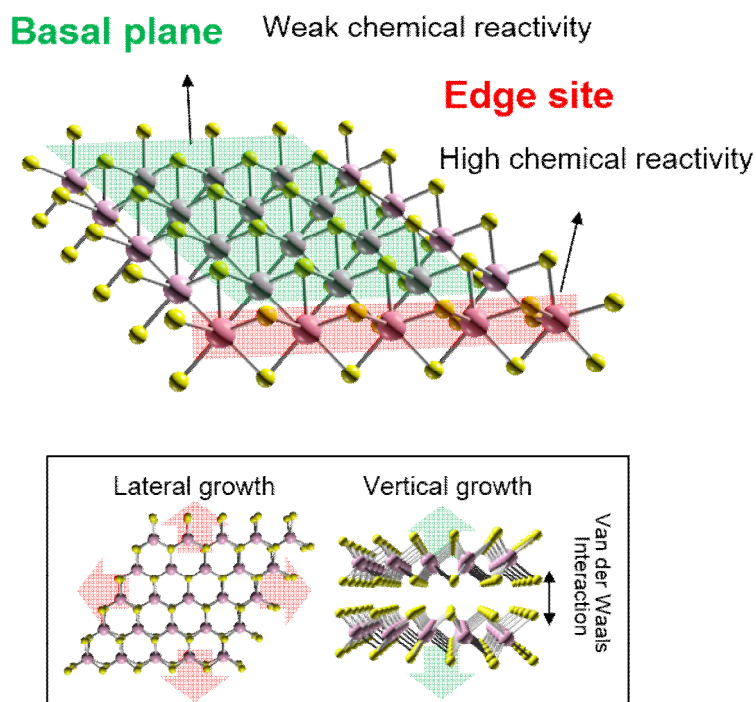


Figure 7.14. Schematics for displaying the chemical reactivity difference between MoS₂ edge site and basal plane. Due to the high chemical reactivity of MoS₂ edge site, lateral growth shows the higher preference than vertical stacking.

7.6. Summary

We demonstrated a predictive fabrication methodology for MoS₂ containing assemblies of 2D van der Waals solids. To control MoS₂ structures and morphologies, a quaternary atomic system of Mo-S-C-O was established by electrospun ATTM+PAN nanofibers and O₂ gas. Among the great diversity of potential reactions, the selective reaction of Mo-S and C-O was required, while also precluding other reactions. The redox reaction was controlled by leveraging the different oxidation tendencies of Mo and C. In the Ellingham diagram, the oxide, sulfide, and carbide formations' ΔGs were considered, and the processing parameters were determined to be O₂ 0.1~0.4 Torr at 800 °C. To predict the material composition of Mo-S-C-O, thermodynamic calculations of ternary phase diagrams (Mo-S-C, Mo-S-O, Mo-C-O, and MoS₂-C-O) and the compound formation ΔG were calculated using a thermochemical database program. In the Mo-S-C phase diagram, a C mole fraction over 0.15 was required to induce MoS₂+CS₂+C. After material composition was fixed as 0.075Mo-0.302S-0.623C, the relative amounts of metal precursor and polymer matrix were determined to be ATTM (1.4 g) + PAN (0.7855 g). In the Mo-S-O and Mo-C-O phase diagrams, the material composition was adjusted to prevent Mo oxidation and an O mole fraction of less than 0.45 was derived to induce the production of MoS₂+SO₂+S and MoC+CO+C. The total amount of nanofibers in the chamber was determined to be 30 mg with an O₂ amount of 2.4 ~ 9.4×10⁻⁶ mol.

Based on this theoretical background, the nanoscale Boudouard reaction enabled the dynamic motion of the elements in nanomaterials through the gas phase reaction. By adjusting the pressure and isothermal time of calcination, the MoS₂ structures and morphologies were controlled kinetically. Surprisingly, spontaneous lateral growth

Chapter 7: Thermodynamic based Reaction Prediction of Multi-component Atomic System for Kinetic van-der Waals Solid Structure Control

and vertical stacking were induced to form MoS₂ nanotubes from single-layered MoS₂ nanoplatelets. This behavior can be explained by the effect of C decomposition on MoS₂ nucleation and growth. It is related to the nanoscale reaction-diffusion process, which is receiving significant attention as a method for overcoming the generation of primitive building blocks of the bottom up methodology.^[104] This scheme can optimize MoS₂ to produce superior performance in electrical, electrochemical and catalytic activities. We believe that this work opens a new synthetic method for revealing the effects of predicted phase and structure control on the behavior of sophisticated atomic multi-components in nanomaterials.

CHAPTER 8

Conclusion

8.1. Summary of results

This study investigated the effect of thermodynamic redox reaction on the phase control and spontaneous assembly of atomic species in electrospun metal compound/C nanofibers. Moreover, underlying metallurgy based thermodynamic principles were applied in the fabrication of heterogeneous multi-atomic nanomaterials. Phase and structure control of the nanomaterials is desired to further expand the functionalities of nanofibers.

Generally, the role of C nanofiber was limited as a supporter which maintains high-aspect ratio 1D structures. However, a new functionality of C nanofiber has been pioneered as a descriptor to determine the migration of nearby atomic species and final structures of metal compound. It is based on oxidation based C decomposition, which produces gaseous decomposition products. Because of the reaction between O_2 (g) and C, the degree of C decomposition can be precisely controlled by the pO_2 . In the case of multi-atomic component system, the reaction between the elements can generate many intriguing compounds. For the selection of target products after calcination, Ellingham diagram and phase diagram can contribute to induce calcination temperature, pressure, and initial material composition. In this thesis, an innovative fabrication methodology for controlling the hybridization of secondary nanostructured C nanofibers and functional materials has been developed *via* predictive synthesis.

Chapter 8: Conclusion

In reductive metal which shows higher ΔG for oxidation than C, metal reduction and C oxidation can be induced simultaneously. According to the pO_2 , various metal/C nanofibers such as fully filled C nanofibers with embedded metal nanoparticles, metal/C core/shell nanofibers, porous or hollow C nanofibers with dispersed metal agglomerates were fabricated from the same precursors during single calcination step. It was revealed that this phenomenon is originated from the catalytic acceleration of C oxidation at the metal surface. Therefore, the C oxidation tendency was higher in the metal with higher bonding energy between O. Co based C system, whose binding energy of 5.92 eV, formed hollow C nanofibers at 1.0×10^{-2} Torr. In contrast, Pt based C system, whose binding energy of 4.42 eV, fully filled C nanofiber structures generated until 5.0×10^{-2} Torr and Pt/C core/shell structure formed at 6.0×10^{-2} Torr. This study reveals a new synthetic route to fabricate diversely structured metal/carbon nanofibers via synergetic effect of C descriptor.

In oxidative metal which shows lower ΔG for oxidation than C, metal/C nanofibers can be fabricated under the inert ambient condition. For the size and distribution control of metallic species, Boudouard reaction which can recycle the solid state C from the gaseous CO, CO₂ is crucial for porosity control. By inducing reverse Boudouard reaction ($C + CO_2 \leftarrow 2CO$), optimized porosity of C descriptor was obtained and it induced to the formation of 15 nm sized Sn nanoparticles uniformly distributed inside C nanofibers. It showed best anode performance in all-solid-state Li-ion cells with a capacity of 762 mAh/g and a coulombic efficiency greater than 99.5 % during 50 cycles.

In multi-atomic component for the fabrication of MoS₂/C nanofibers, redox reactions between Mo-S-C-O should be considered by the Ellingham diagram and ternary phase diagram. Selective Mo-S and C-O reaction should be induced for MoS₂ formation with the C combustion to form CO, CO₂. Tie-line calculated in ternary and quaternary phase

Chapter 8: Conclusion

diagram enables us to predict which phases can evolve and exist stably in our Mo-S-C-O system. As a result, after identifying the specific region where the Mo-S, C-O reaction occurs, we can successfully produce macroscopically-assembled 2D-MoS₂ crystals inside and on C nanofibers. Interestingly, because of the interplay between ad-atom growth and gas phase inter-diffusion, vertical stacking and lateral growth of MoS₂ were controlled with remarkable precision and MoS₂ nanotubes were directly converted from C-based nanofibers.

This study provides important information on the design of nanomaterial synthesis *via* quantitative understanding of the behavior of sophisticated atomic multi-components is increasing. It can provide core principles to understand the effect of spontaneous atomic reaction and migration on the phase, morphology, size, arrangement, and distribution in nanomaterials.

8.2. Future works and suggested research

The importance of quantitative understanding of the behavior of sophisticated atomic multi-components is increasing. For example, in a quaternary atomic system, transition metal (M_{trans})-containing systems such as M_{trans} , C, N, and O are important as electrochemical catalysts, and the impact of M_{trans} is significant for the activation and transformation of C, S, and O bonding. In this thesis, theoretically and experimentally revealed new insight can predict thermodynamic phase stability, to the fabrication of nanomaterials, in which the surface energy distorts the expected bulk-scale. This methodology can be expanded by applying to the fabrication of dual metal compounds system such as MoS_2 and WS_2 . For the structure control of MoS_2 and WS_2 by utilizing the C descriptor, redox reactions of Mo-W-S-C-O should be considered (**Figure 8.1**).

This scheme proceeds the calcination of Mo-W-S-C solid state nanofibers under O_2 gas ambient (**Figure 8.1a**). In this condition, various compounds such as MoS_x , MoC_x , MoO_x , WS_x , WC_x , WO_x , CS_x , SO_x , CO_x can be induced. Among them, selective reactions between Mo-S, W-S, and C-O should be induced with preventing others. In **Figure 8.1b**, to investigate the standard Gibbs free energy for the formation of these compounds, Ellingham diagram has been studied (ΔG° of $\text{WS}_2=-168.57$, $\text{MoS}_2=-201.22$, $\text{MoO}_2=-395.59$, $\text{WO}_2=-398.59$ kJ/mol). W shows the higher preference of oxide than Mo and lower preference of sulfide than Mo. Therefore, the condition for inducing selective formation of MoS_2 and WS_2 should be studied more in detail by reciprocal phase diagram in **Figure 8.1c**. By extracting the mole fraction region between them, MoS_2 and WS_2 structure region can be induced. Based on this

Chapter 8: Conclusion

theoretical background, the implication of predictive synthesis methodology will be studied in future work.

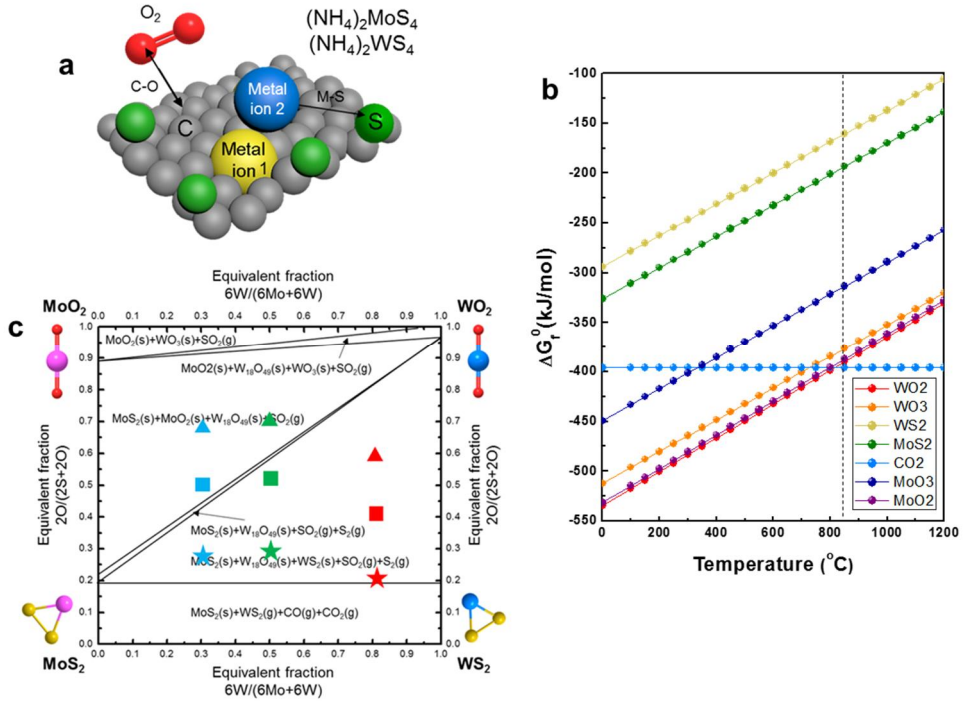


Figure 8.1. (a) Schematics for displaying the 5 atomic component of Mo-W-S-C-O for the fabrication of MoS₂+WS₂ inside C nanofibers. (b) Ellingham diagram for displaying the chemical potential (Gibbs free energy) about the compounds formed in Mo-W-S-C-O system. (c) Reciprocal phase diagram of Mo-W-S-O.

References

- [1] M. Inagaki, Y. Yang, F. Kang, *Adv. Mater.* **2012**, *24*, 2547.
- [2] D.-H. Nam, J.-H. Lee, N.-R. Kim, Y.-Y. Lee, H.-W. Yeon, S.-Y. Lee, Y.-C. Joo, *Carbon N. Y.* **2015**, *82*, 273.
- [3] C. Kim, *J. Power Sources* **2005**, *142*, 382.
- [4] M. Wang, Z.-H. Huang, L. Wang, M.-X. Wang, F. Kang, H. Hou, *New J. Chem.* **2010**, *34*, 1843.
- [5] L. Zou, L. Gan, R. Lv, M. Wang, Z.-H. Huang, F. Kang, W. Shen, *Carbon N. Y.* **2011**, *49*, 89.
- [6] L. Ji, X. Zhang, *Electrochem. commun.* **2009**, *11*, 795.
- [7] V. Thavasi, G. Singh, S. Ramakrishna, *Energy Environ. Sci.* **2008**, *1*, 205.
- [8] Q. B. Yang, D. M. Li, Y. L. Hong, Z. Y. Li, C. Wang, S. L. Qiu, Y. Wei, *Synth. Met.* **2003**, *137*, 973.
- [9] S. Wang, Y. Li, Y. Wang, Q. Yang, Y. Wei, *Mater. Lett.* **2007**, *61*, 4674.
- [10] X. Lu, C. Wang, Y. Wei, *Small* **2009**, *5*, 2349.
- [11] X. Lu, Y. Zhao, C. Wang, *Adv. Mater.* **2005**, *17*, 2485.
- [12] W. K. Son, J. H. Youk, T. S. Lee, W. H. Park, *Macromol. Rapid Commun.* **2004**, *25*, 1632.
- [13] K. Sode, M. Tanaka, Y. Suzuki, H. Kawakami, *Nanoscale* **2013**, *5*, 8235.
- [14] P.-C. Hsu, H. Wu, T. J. Carney, M. T. McDowell, Y. Yang, E. C. Garnett, M. Li, L. Hu, Y. Cui, *ACS Nano* **2012**, *6*, 5150.
- [15] D. Li, Y. Xia, *Adv. Mater.* **2004**, *16*, 1151.
- [16] J. Shin, S.-J. Choi, I. Lee, D.-Y. Youn, C. O. Park, J.-H. Lee, H. L. Tuller, I.-D. Kim, *Adv. Funct. Mater.* **2013**, *23*, 2357.

- [17] C.-L. Zhang, S.-H. Yu, *Chem. Soc. Rev.* **2014**, *43*, 4423.
- [18] S. Kang, Y. Mo, S. P. Ong, G. Ceder, *Nano Lett.* **2014**, *14*, 1016.
- [19] W. Sun, S. Jayaraman, W. Chen, K. A. Persson, G. Ceder, *Proc. Natl. Acad. Sci.* **2015**, *112*, 3199.
- [20] L. Shi, A. Xu, T. S. Zhao, *Phys. Chem. Chem. Phys.* **2015**, *17*, 29859.
- [21] F. Güder, Y. Yang, S. Goetze, A. Berger, N. Ramgir, D. Hesse, M. Zacharias, *Small* **2010**, *6*, 1603.
- [22] Y. Qin, Y. Yang, R. Scholz, E. Pippel, X. Lu, M. Knez, *Nano Lett.* **2011**, *11*, 2503.
- [23] D. Hecht, L. Hu, G. Grüner, *Appl. Phys. Lett.* **2006**, *89*, DOI <http://dx.doi.org/10.1063/1.2356999>.
- [24] A. Greiner, J. H. Wendorff, *Angew. Chemie - Int. Ed.* **2007**, *46*, 5670.
- [25] D. Li, Y. Xia, *Nano Lett.* **2004**, *4*, 933.
- [26] N. Bhardwaj, S. C. Kundu, *Biotechnol. Adv.* **2010**, *28*, 325.
- [27] J. T. McCann, D. Li, Y. Xia, *J. Mater. Chem.* **2005**, *15*, 735.
- [28] Z. Sun, E. Zussman, A. L. Yarin, J. H. Wendorff, A. Greiner, *Adv. Mater.* **2003**, *15*, 1929.
- [29] A. Magdziarz, S. Werle, *Waste Manag.* **2014**, *34*, 174.
- [30] D. R. Gaskell, *Introduction to the Thermodynamics of Materials*, Taylor And Francis, **2008**.
- [31] J.-W. Snoeck, G. F. Froment, M. Fowles, *Ind. Eng. Chem. Res.* **2002**, *41*, 4252.
- [32] D.-H. Nam, J. W. Kim, J.-H. Lee, S.-Y. Lee, H.-A.-S. Shin, S.-H. Lee, Y.-C. Joo, *J. Mater. Chem. A* **2015**, *3*, 11021.
- [33] J. Moon, V. Sahajwalla, *Metall. Mater. Trans. B* **2006**, *37*, 215.
- [34] A. Findlay, *The Phase Rule and Its Applications*, Longmans, Green, **1906**.

- [35] R. Beyers, K. B. Kim, R. Sinclair, *J. Appl. Phys.* **1987**, *61*, 2195.
- [36] K. J. Hubbard, D. G. Schlom, I. Introduction, *J. Mater. Res.* **1996**, *11*, 2757.
- [37] A. D. Pelton, C. W. Bale, P. L. Lin, *Can. J. Chem.* **1984**, *62*, 457.
- [38] Z. Lin, D. Han, S. Li, *J. Therm. Anal. Calorim.* **2012**, *107*, 471.
- [39] F. C. Nix, D. MacNair, *Phys. Rev.* **1941**, *60*, 597.
- [40] F. C. Marques, R. G. Lacerda, A. Champi, V. Stolojan, D. C. Cox, S. R. P. Silva, *Appl. Phys. Lett.* **2003**, *83*, 3099.
- [41] G.-D. Lee, C. Z. Wang, E. Yoon, N.-M. Hwang, K. M. Ho, *Appl. Phys. Lett.* **2008**, *92*, DOI <http://dx.doi.org/10.1063/1.2837632>.
- [42] G.-D. Lee, C.-Z. Wang, J. Yu, E. Yoon, N.-M. Hwang, K.-M. Ho, *Phys. Rev. B* **2007**, *76*, 165413.
- [43] L. Ji, X. Zhang, *Energy Environ. Sci.* **2010**, *3*, 124.
- [44] S.-B. Son, J. E. Trevey, H. Roh, S.-H. Kim, K.-B. Kim, J. S. Cho, J.-T. Moon, C. M. DeLuca, K. K. Maute, M. L. Dunn, H. N. Han, K. H. Oh, S.-H. Lee, *Adv. Energy Mater.* **2011**, *1*, 1199.
- [45] Y. Yu, L. Gu, C. Wang, A. Dhanabalan, P. A. Van Aken, J. Maier, *Angew. Chemie - Int. Ed.* **2009**, *48*, 6485.
- [46] B. Wang, B. Luo, X. Li, L. Zhi, *Mater. Today* **2012**, *15*, 544.
- [47] L. Ji, Z. Lin, M. Alcoutlabi, X. Zhang, *Energy Environ. Sci.* **2011**, *4*, 2682.
- [48] Y. Xu, Q. Liu, Y. Zhu, Y. Liu, A. Langrock, M. R. Zachariah, C. Wang, *Nano Lett.* **2013**, *13*, 470.
- [49] Y. Liu, N. Zhang, L. Jiao, Z. Tao, J. Chen, *Adv. Funct. Mater.* **2014**.
- [50] X. Han, Y. Liu, Z. Jia, Y.-C. Chen, J. Wan, N. Weadock, K. J. Gaskell, T. Li, L. Hu, *Nano Lett.* **2014**, *14*, 139.
- [51] D. M. Piper, J. H. Woo, S.-B. Son, S. C. Kim, K. H. Oh, S.-H. Lee, *Adv. Mater.*

- 2014**, *26*, 3520.
- [52] S. Cavaliere, S. Subianto, I. Savych, D. J. Jones, J. Rozière, *Energy Environ. Sci.* **2011**, *4*, 4761.
- [53] B.-Z. Lee, D. N. Lee, *Acta Mater.* **1998**, *46*, 3701.
- [54] S. L. Lai, J. Y. Guo, V. Petrova, G. Ramanath, L. H. Allen, *Phys. Rev. Lett.* **1996**, *77*, 99.
- [55] P. I. Ravikovitch, A. V Neimark, *Colloids Surfaces A Physicochem. Eng. Asp.* **2001**, *187–188*, 11.
- [56] E. P. Barrett, L. G. Joyner, P. P. Halenda, *J. Am. Chem. Soc.* **1951**, *73*, 373.
- [57] S. Dalton, F. Heatley, P. M. Budd, *Polymer (Guildf)*. **1999**, *40*, 5531.
- [58] Z. Bashir, *Carbon N. Y.* **1991**, *29*, 1081.
- [59] W. Watt, W. Johnson, *Nature* **1975**, *257*, 210.
- [60] I. Shimada, T. Takahagi, M. Fukuhara, K. Morita, A. Ishitani, *J. Polym. Sci. Part A Polym. Chem.* **1986**, *24*, 1989.
- [61] A. C. Ferrari, J. Robertson, *Phys. Rev. B* **2000**, *61*, 14095.
- [62] Q. F. Huang, S. F. Yoon, Rusli, H. Yang, B. Gan, K. Chew, J. Ahn, *J. Appl. Phys.* **2000**, *88*, 4191.
- [63] C. Nayral, E. Viala, P. Fau, F. Senocq, J.-C. Jumas, A. Maisonnat, B. Chaudret, *Chem. - A Eur. J.* **2000**, *6*, 4082.
- [64] M. Kwoka, L. Ottaviano, M. Passacantando, S. Santucci, G. Czempik, J. Szuber, *Proc. 4th Int. Work. Semicond. Gas Sensors (SGS 2004)* **2005**, *490*, 36.
- [65] A. K. Geim, I. V Grigorieva, *Nature* **2013**, *499*, 419.
- [66] B. Choi, J. Yu, D. W. Paley, M. T. Trinh, M. V Paley, J. M. Karch, A. C. Crowther, C.-H. Lee, R. A. Lalancette, X. Zhu, P. Kim, M. L. Steigerwald, C. Nuckolls, X. Roy, *Nano Lett.* **2016**, *16*, 1445.

- [67] M. Chhowalla, H. S. Shin, G. Eda, L.-J. Li, K. P. Loh, H. Zhang, *Nat Chem* **2013**, *5*, 263.
- [68] Y. Shi, H. Li, L.-J. Li, *Chem. Soc. Rev.* **2015**, *44*, 2744.
- [69] O. Lopez-Sanchez, D. Lembke, M. Kayci, A. Radenovic, A. Kis, *Nat Nano* **2013**, *8*, 497.
- [70] H. W. Wang, P. Skeldon, G. E. Thompson, *J. Mater. Sci.* **1998**, *33*, 3079.
- [71] H. W. Wang, P. Skeldon, G. E. Thompson, G. C. Wood, *J. Mater. Sci.* **1997**, *32*, 497.
- [72] J. L. Brito, M. Ilija, P. Hernández, *Thermochim. Acta* **1995**, *256*, 325.
- [73] RadisavljevicB., RadenovicA., BrivioJ., GiacomettiV., KisA., *Nat Nano* **2011**, *6*, 147.
- [74] S. Wi, H. Kim, M. Chen, H. Nam, L. J. Guo, E. Meyhofer, X. Liang, *ACS Nano* **2014**, *8*, 5270.
- [75] D. J. Late, Y.-K. Huang, B. Liu, J. Acharya, S. N. Shirodkar, J. Luo, A. Yan, D. Charles, U. V Waghmare, V. P. Dravid, C. N. R. Rao, *ACS Nano* **2013**, *7*, 4879.
- [76] Q. He, Z. Zeng, Z. Yin, H. Li, S. Wu, X. Huang, H. Zhang, *Small* **2012**, *8*, 2994.
- [77] W. Wu, L. Wang, Y. Li, F. Zhang, L. Lin, S. Niu, D. Chenet, X. Zhang, Y. Hao, T. F. Heinz, J. Hone, Z. L. Wang, *Nature* **2014**, *514*, 470.
- [78] H. Hwang, H. Kim, J. Cho, *Nano Lett.* **2011**, *11*, 4826.
- [79] L. David, R. Bhandavat, G. Singh, *ACS Nano* **2014**, *8*, 1759.
- [80] T. F. Jaramillo, K. P. Jørgensen, J. Bonde, J. H. Nielsen, S. Horch, I. Chorkendorff, *Science (80-.)*. **2007**, *317*, 100.
- [81] M. Asadi, B. Kumar, A. Behranginia, B. A. Rosen, A. Baskin, N. Reppin, D. Pisasale, P. Phillips, W. Zhu, R. Haasch, R. F. Klie, P. Král, J. Abiade, A.

- Salehi-Khojin, *Nat Commun* **2014**, *5*.
- [82] Y. Li, H. Wang, L. Xie, Y. Liang, G. Hong, H. Dai, *J. Am. Chem. Soc.* **2011**, *133*, 7296.
- [83] D. J. Li, U. N. Maiti, J. Lim, D. S. Choi, W. J. Lee, Y. Oh, G. Y. Lee, S. O. Kim, *Nano Lett.* **2014**, *14*, 1228.
- [84] C. Zhu, X. Mu, P. A. van Aken, Y. Yu, J. Maier, *Angew. Chemie Int. Ed.* **2014**, *53*, 2152.
- [85] H. Zhu, F. Lyu, M. Du, M. Zhang, Q. Wang, J. Yao, B. Guo, *ACS Appl. Mater. Interfaces* **2014**, *6*, 22126.
- [86] X. Xiong, W. Luo, X. Hu, C. Chen, L. Qie, D. Hou, Y. Huang, *Sci. Rep.* **2015**, *5*, 9254.
- [87] S. Yu, J.-W. Jung, I.-D. Kim, *Nanoscale* **2015**, *7*, 11945.
- [88] J. Park, J. Lee, *Calphad* **2008**, *32*, 135.
- [89] C. W. Bale, P. Chartrand, S. A. Degterov, G. Eriksson, K. Hack, R. Ben Mahfoud, J. Melançon, A. D. Pelton, S. Petersen, *Calphad* **2002**, *26*, 189.
- [90] J. M. Deitzel, J. Kleinmeyer, D. Harris, N. C. Beck Tan, *Polymer (Guildf)*. **2001**, *42*, 261.
- [91] P. Tonndorf, R. Schmidt, P. Böttger, X. Zhang, J. Börner, A. Liebig, M. Albrecht, C. Kloc, O. Gordan, D. R. T. Zahn, S. M. De Vasconcellos, R. Bratschitsch, **2013**, *21*, 4908.
- [92] A. C. Ferrari, J. Robertson, *Philos. Trans. R. Soc. A Math. Phys. Eng. Sci.* **2004**, *362*, 2477.
- [93] H. Wang, Z. Lu, S. Xu, D. Kong, J. J. Cha, G. Zheng, P.-C. Hsu, K. Yan, D. Bradshaw, F. B. Prinz, Y. Cui, *Proc. Natl. Acad. Sci.* **2013**, *110*, 19701.
- [94] B. Seo, G. Y. Jung, Y. J. Sa, H. Y. Jeong, J. Y. Cheon, J. H. Lee, H. Y. Kim, J.

- C. Kim, H. S. Shin, S. K. Kwak, S. H. Joo, C. Engineering, U. Central, **2015**, 3728.
- [95] J. Kibsgaard, T. F. Jaramillo, F. Besenbacher, *Nat Chem* **2014**, *6*, 248.
- [96] Y. Feldman, E. Wasserman, D. J. Srolovitz, R. Tenne, *Science (80-.)*. **1995**, 267, 222.
- [97] M. Nath, A. Govindaraj, C. N. R. Rao, *Adv. Mater.* **2001**, *13*, 283.
- [98] M. Remškar, A. Mrzel, M. Viršek, A. Jesih, *Adv. Mater.* **2007**, *19*, 4276.
- [99] M. Bar-Sadan, A. N. Enyashin, S. Gemming, R. Popovitz-Biro, S. Y. Hong, Y. Prior, R. Tenne, G. Seifert, *J. Phys. Chem. B* **2006**, *110*, 25399.
- [100] A. N. Enyashin, S. Gemming, M. Bar-Sadan, R. Popovitz-Biro, S. Y. Hong, Y. Prior, R. Tenne, G. Seifert, *Angew. Chemie Int. Ed.* **2007**, *46*, 623.
- [101] M. I. Mendeleev, D. J. Srolovitz, S. A. Safran, R. Tenne, *Phys. Rev. B* **2002**, *65*, 75402.
- [102] L. P. Hansen, E. Johnson, M. Brorson, S. Helveg, **2014**.
- [103] M. Bosi, *RSC Adv.* **2015**, *5*, 75500.
- [104] I. R. Epstein, B. Xu, *Nat Nano* **2016**, *11*, 312.

요약(국문초록)

나노 스케일 에서의 정확한 상 제어 및 거시적 단위에서의 자가 형성 기술은 중요하지만 나노소재의 실제 응용에 있어서 한계점을 보인다. 다중원소로 구성된 소재의 합성조건에서 대량 생산과 균일성 확보에서 있어서 가장 어려운 요소는 열역학 및 반응속도론적 이론을 기반으로 하는 예측성이 부족하다는 점이다. 본 연구에서는 전통적인 화학 야금학 이론을 적용하여 나노소재의 합성에서 야기되는 공정상 문제점을 해결하는 방안을 제시한다.

금속 화합물/탄소 나노섬유는 에너지 및 환경 분야에서 야기되는 문제점을 해결하기 위한 소재로 각광받고 있다. 금속 화합물은 전기화학적 반응에서 높은 활성을 보이는 소재이다. 그리고 전기전도성의 탄소 나노섬유는 높은 종횡비의 1 차원 나노구조를 형성하는 역할을 수행한다. 본 연구에서는 이러한 탄소 나노섬유의 기존의 역할에서 발전하여, 복합소재 내에서의 원자 이동 제어를 통해 궁극적으로는 금속 화합물의 최종 구조를 결정할 수 있는 인자 (descriptor)로서의 새로운 탄소 나노섬유의 역할을 제시한다. 이는 일산화탄소 (CO) 혹은 이산화탄소 (CO₂)와 같은 기체 상태의 탄소 분해 부산물을 유도하는 연소 기반 열분해 반응과 관련되어 있다. 탄소와 산소의 반응을 기반으로 하므로 탄소의 분해 정도는 하소 (calcination) 과정에서의 산소분압 (pO₂)에 의해 제어된다. 다중원소로 구성된 소재 시스템에서는 다양한 반응 및 반응생성물이 형성된다. 이들 중 선택적인 원소 간의 반응 유도를 위해서 엘링검 도표 및 상도표를 통해 공정 변수 및 소재 조성을 예측할 수 있다. 이러한 이론적 배경을 바탕으로 본 연구에서는 금속 화합물 활물질과 탄소 나노섬유의 상과 구조를 동시에 제어할 수 있는 예측합성법을 개발하였다.

우선적으로 선택적 탄소 산화반응을 기반으로 한 환원 경향성 금속 구조의 제어 방법에 대해 탐구하였다. 탄소의 산화반응에 대한 깃스 자유 에너지 (ΔG)를 기준으로 탄소보다 산화반응성이 낮은 환원성 금속, 탄소보다 산화반응성이 높은 산화성 금속으로 나누었다. Co, Ni, Cu, Pt 와 같은 환원성 금속의 경우에는 선택적 리독스반응 유도를 통해 금속의 환원과 탄소의 산화를 유도할 수 있다. 본 조건에서는 산소분압 제어에 의해 금속 나노입자가 분산된 탄소 나노섬유, 금속/탄소 코어/셸 나노섬유, 중공 및 다공성 구조의 나노섬유 등과 같이 다양한 구조의 나노섬유를 형성할 수 있다. 이러한 구조 제어의 메커니즘은 금속 표면에서 촉진되는 탄소의 산화반응과 관련 있다.

산화성 금속의 구조 제어는 탄소보다 금속의 산화 반응성이 높기 때문에 금속과 탄소가 산화되지 않는 분위기에서의 열처리를 전제조건으로 탄소의 다공성을 제어를 통해 유도되었다. 리튬 이온 전지의 음극으로 높은 용량을 구현할 수 있는 주석의 크기와 분포도는 하소 과정에서 주석의 외부확산을 제어함으로써 최적의 조건을 유도하였다. 이는 부두아 반응을 역으로 유도할 수 있는 압력평형을 제어하여 기체 상태의 CO로부터 탄소를 환원시키는 원리로 구현되었다.

기존의 금속/탄소 시스템에서 금속화합물/탄소 시스템을 구현하기 위해서는 4 성분계 이상의 구성원소에 대한 열역학적 전략수립이 필요하다. 이들의 선택적 산화, 환원 반응 유도를 통해 본 연구에서는 탄소 나노섬유 내에 이황화 몰리브덴 (MoS_2)의 구조를 제어하는 기술을 구현하였다. Mo-S-C-O 의 4 성분계에서 리독스 반응은 산소분압에 따라 분류될 수 있다. 이 중에서 몰리브덴과 탄소의 산화 반응에 대한 깃스 자유에너지 사이 구간을 산소분압 제어를 통해 유도할 수 있다. 이 구간에서는 몰리브덴의 환원과 탄소의 산화를 선택적으로 유도할 수 있으며 이는 이황화 몰리브덴의 형성과 동시에 탄소의 연소 반응을 가능하게 한다. 이러한 엘링검도표 기반의 공정변수 예측과 함께, 이를 유도하기 위한 삼원계 상도표를 통해 Mo-S-C-O 의 몰분율을 계산함으로써 소재 조성을 예측할 수 있다.

이 조건에서의 하소과정을 통해 이황화 물리브덴의 수직 적층 및 수평 성장을 제어하였다. 이를 통해 길이, 적층수, 분포, 정렬 등의 다양한 구조적 인자를 동시에 제어할 수 있었다.

본 연구에서는 동일한 금속 전구체와 고분자 매트릭스 나노섬유로부터 열역학적으로 예측된 변수에 의해 금속 화합물/탄소 나노섬유의 구조와 상이 다양하게 제어될 수 있음을 최초로 제시하였다. 이러한 합성 방법론은 금속 화합물/탄소 나노섬유를 에너지, 환경, 전자, 화학 등의 다양한 분야에서 최적의 성능을 구현할 수 있도록 하는 특성을 맞춤형으로 구현할 수 있게 한다.

표제어: 전기방사, 금속 화합물/탄소 나노섬유, 하소 공정, 선택적 산화, 엘링검 도표, 상도표, 예측 합성

학 번: 2011-20636